7-12-2023

Characterization of Subcellular Functional Domains in the Vesicular Glutamate Transporter 3-Expressing Retinal Amacrine Cell using Correlative Light and Electron Microscopy

Karl Friedrichsen
Washington University in St. Louis

WASHINGTON UNIVERSITY IN ST. LOUIS

Division of Biology and Biomedical Sciences
Neurosciences

Dissertation Examination Committee:
Joshua Morgan, Chair
Martha Bagnall
Brian Clark
Timothy Holy
Daniel Kerschensteiner

Characterization of Subcellular Functional Domains in the
Vesicular Glutamate Transporter 3-Expressing Retinal Amacrine Cell
using Correlative Light and Electron Microscopy
by
Karl Friedrichsen

A dissertation presented to
Washington University in St. Louis
in partial fulfillment of the
requirements for the degree
of Doctor of Philosophy

August 2023
St. Louis, Missouri

Table of Contents

List of Figures

List of Tables

<u>Acknowledgments</u>

I have many people to thank. I have been incredibly fortunate in having family and friends who have helped me in countless ways, and I would certainly not have made it here without their help.

I thank my parents for their unwavering support throughout my many triumphs and setbacks. I literally and metaphorically wouldn't be here without them.

I thank Nelly for perpetually pushing me towards every good thing in life, quite forcefully when necessary. I would not have finished graduate school, or even gotten into graduate school, without her confidence, understanding, scientific writing prowess, and skilled dismantling of every excuse I make for myself.

I thank our two sons, Samuel and Matisse, for filling every day with laughter and happiness, and for making the choice between finishing a coding project or finishing a dinosaur puzzle an easy one to make.

I thank Dr. Josh Morgan for having infinite patience every time I couldn't make it to lab because one of our sons was sick, or because daycare flooded, or because the car needed a new tire, or any of the other hundred things that conspired to make it a work-from-home day.

And I profusely thank my committee members for their patience, understanding, insight, and constant deadline extensions.

Karl Friedrichsen

Washington University in St. Louis
August 2023

Dedicated to my family

ABSTRACT OF THE DISSERTATION

Characterization of Subcellular Functional Domains in the

Vesicular Glutamate Transporter 3-Expressing Retinal Amacrine Cell

using Correlative Light and Electron Microscopy

by

Karl Friedrichsen

Doctor of Philosophy in Biology and Biomedical Sciences

Neurosciences

Washington University in St. Louis, 2023

Professor Joshua L Morgan, Chair

The following work seeks to better understand how neurons process multiple streams of information within the branches of their dendritic arbors. We use correlated light and electron microscopy to capture both live subcellular calcium responses and detailed morphology and synaptic connectivity in a unique retinal amacrine cell in order to directly study the relationship between structure and function. The vesicular glutamate transporter 3-expressing amacrine cell (VG3) selectively integrates and segregates visual information within its arbor branches and provides multiple target neuron types with appropriate excitatory or inhibitory synaptic inputs. By reconstructing VG3 arbor branches, synapses, and connected cell types, we learn which retinal circuits and visual pathways the VG3 contributes to and to what extent. By comparing this connectomic information with the subcellular responses to light stimuli in those same arbor branches, we learn how visual information flows through the VG3 arbor and how it selectively integrates multiple synaptic inputs and targets outputs to specific downstream neurons in opposing visual pathways simultaneously. Along the way we describe a polyaxonal amacrine

cell which almost exclusively targets VG3 and which is thought to be a primary source of the

VG3's ability to discriminate between local motion and global motion.

Chapter 1

Introduction

1.1 Subcellular Processing Within Neuronal Arbors

A common notion of neuronal function begins with input synapses on the branches of a neuron's dendritic arbor. When signals are received through these synapses, electrical impulses are transmitted up the arbor branches, diminishing in strength as they travel, to the soma, and to the axon hillock and axon (Colbert & Johnston, 1996; Richardson et al., 1987). If the sum of the inputs is sufficient, an action potential is initiated and travels down the axon to the output synapses. The summing of inputs on the dendritic arbor occurs across both time and space, so synchronous inputs have a greater effect, as do inputs closer to the soma and axon (reviewed in (Magee, 2000)). Further, input synapses can be inhibitory or excitatory, so coincident inputs with opposite signs can 'cancel' each other. The reality of how inputs are integrated within arbors is much more complex than this simplified version, and different arrangements of synaptic inputs and arbor branch morphologies are used to accomplish many dendritic processing tasks throughout the nervous system (London & Häusser, 2005; Tran-Van-Minh et al., 2015).

Many factors affect how synaptic inputs are integrated within a neuronal arbor. Firstly, at the site of the synapse these factors include the type of synapse (electrical or chemical), the type

1

of receptor (ionotropic or metabotropic), the polarity of its effect on the postsynaptic cell's membrane potential (depolarization or hyperpolarization), and the longevity of its effect. Once an input is received, a postsynaptic potential travels outward, diminishing in strength according to the length and time constants of the membrane. These constants are determined by the electrical properties of the membrane (impedance, capacitance, etc.) and whether the postsynaptic potential is conveyed via active or passive conduction (Rall, 1967, 1969). Postsynaptic potentials can also interact with each other, such as in the case of shunting inhibition or participation in sublinear or supralinear summation (Borst & Egelhaaf, 1994; Koch et al., 1983). In the case of shunting inhibition, an inhibitory synaptic input diminishes any excitatory postsynaptic potentials traveling through the area (Holt & Koch, 1997; Prescott & De Koninck, 2003).

Expanding the possibilities for computation within a single neuron, there exist types of neurons that do not have axons and instead have their output synapses on the same arbor branches as their input synapses. This arrangement creates the opportunity for different areas of the arbor to function semi-independently. Instead of the entire arbor being summed to make the binary decision to initiate an action potential or not, each individual output synapse makes the determination whether to release neurotransmitter depending on conditions at its specific location on the arbor. Each output synapse has a unique view of the arbor's inputs, being influenced by their relative distances and the morphology of the arbor branches. The amacrine cells of the retina are an example of these "axon-less" neurons, and they leverage their branch autonomy to allow single arbor branches to perform specific local processing tasks in dozens or hundreds of locations simultaneously.

1.2 Retinal Organization and Processing

The retina is a thin structure in the back of the eyeball including several layers of retinal neurons and their arbors. It translates light information into electrical impulses describing the visual scene. The layered structure of the retina roughly corresponds to the different stages of visual processing, with each stage combining information from previous stages to detect increasingly complex visual features (reviewed in (Masland, 2001)).

Retinal processing can be broadly divided into 'vertical' and 'horizontal' flow (Figure 1). Vertical flow involves processing information describing one location in visual space. Photoreceptors first encode light levels as series of electrical impulses which are transmitted to the bipolar cells directly below them through glutamatergic synapses in the outer plexiform layer (OPL). The bipolar cells parallelize the information into two complimentary streams, the ON and OFF visual pathways, which describe areas of the visual scene increasing and decreasing in luminance, respectively (reviewed in (Ichinose & Habib, 2022)). Those bipolar cells then carry the information through the inner nuclear layer (INL) and into the inner plexiform layer (IPL), a dense plexus containing the axonal terminals of the bipolar cells and the dendritic arbors of the RGCs. Different types of bipolar cells form axon terminals at different depths within the IPL according to their light response properties. The inner IPL, nearest to the bipolar cell bodies, is where OFF bipolar cells terminate, and the outer IPL, closer to the ganglion cell layer (GCL), is where the ON bipolar cells terminate. Additionally, some bipolar cells have more sustained
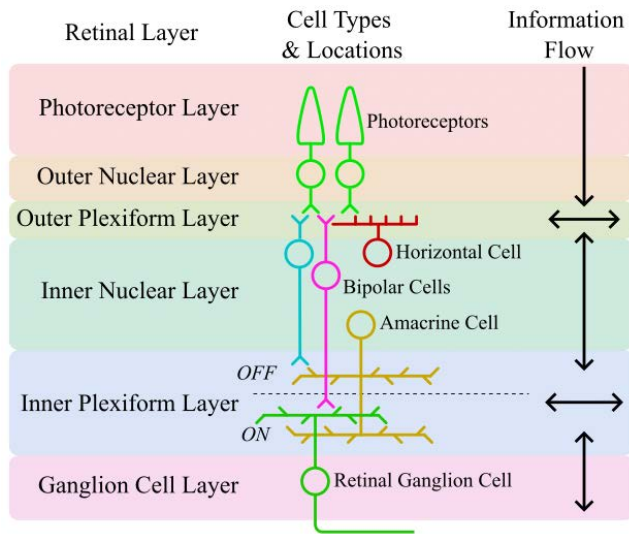
Figure 1.1. The layers of the retina. The types of retinal neurons with somas and neuritic arbors in each layer, and the direction of information flow in each layer. The overall transmission of information is from the photoreceptors in the outer retina (top) through the plexiform layers and to the RGCs of the inner retina (bottom).

responses to changes in illumination while others are more transient in their responses. Bipolar cells with transient responses terminate near the border between the OFF and ON layers of the IPL, while those with sustained responses terminate nearer the IPL borders with adjoining nuclear layers.

Horizontal flow concerns comparison of one area of the retina with neighboring areas. Comparing light levels in adjacent areas can detect local gradients or edges (reviewed in (Kesserwani, 2020).

Comparing these features over a larger area can detect edge orientations. Integrating this information over time can detect motion and its direction (Euler et al., 2002; J. S. Kim et al., 2014). Horizontal processing is accomplished by retinal neuron types with significant horizontal arbor branching: horizontal cells (in the OPL), and amacrine cells and RGCs (in the IPL).

Horizontal cells receive synaptic input directly from photoreceptors, and they transmit this information through the both locally and globally to bipolar cells, photoreceptors, and other horizontal cells using a variety of mechanisms, including multiple neurotransmitters and gap junctions (Grove et al., 2019; X. Liu et al., 2013; McMahon et al., 1989). These computations are thought to underlie the center-surround response properties of bipolar cells and enhance image contrast, provide color discrimination, and control visual gain and light adaptation (reviewed in (Chapot et al., 2017; Thoreson & Mangel, 2012)).

4

Retinal amacrine cells are interneurons which have their arbors in the IPL. Amacrine cells derive their name from the Greek for "without long process", referring to their stereotypical lack of axons. They instead often have their inputs and outputs on the same arbor branches, and their varied morphologies, synaptic connections, and synaptic distribution patterns permit them to perform a large array of different tasks, including detecting motion direction, enabling vision in low light, and driving innate behaviors in response to visual stimuli (Lagnado, 1998; Masland, 2012). To perform these computations, they receive excitatory inputs from bipolar cells and inhibitory inputs from other amacrine cells. They innervate bipolar cells, other amacrine cells, and RGCs. They primarily form GABA-ergic or glycinergic inhibitory synapses, though several types also make use of other neurotransmitters, such as acetylcholine, glutamate, and dopamine. There are over 60 types of amacrine cells (Yan et al., 2020), and their arbor morphologies include monostratified, bistratified, and diffuse arbors with spans ranging from tens of microns to several thousand (MacNeil et al., 1999; MacNeil & Masland, 1998; Strettoi & Masland, 1996).

Retinal Ganglion cells are the projection neurons of the retina, sending their axons out the back of the eye via the optic nerve and projecting to as many as 50 areas of the central nervous system (Martersteck et al., 2017). Approximately 40-45 types have been identified in the mammalian retina, with general agreement between classification strategies based on functional responses and on arbor morphology (Goetz et al., 2022). The dendritic morphologies and response characteristics of RGCs are diverse, with some types responding to motion in particular motion directions, edge orientations, sizes of moving objects, global motion of the entire retinal image, and other complex spatiotemporal features of the visual scene (Barlow, 1953; Barlow et al., 1964; Hartline, 1938; Kuffler, 1953; Maturana et al., 1959). To detect these features, RGC

arbors integrate information from both bipolar cells and amacrine cells, which usually provide excitatory and inhibitory inputs, respectively, and RGC arbors have been shown to perform both linear and non-linear summation of inputs (Demb et al., 1999; Enroth-Cugell & Robson, 1966; Khani & Gollisch, 2021; Kuffler, 1953; Rodieck & Stone, 1965). Like bipolar cells, RGC are commonly classified as ON or OFF by their responses to changes in light levels. However, since they can integrate information from multiple bipolar cell types, there are also ON-OFF RGC, which respond to both increases and decreases in light.

1.3 The vesicular glutamate transporter 3 (vGluT3)-expressing amacrine cell (VG3)

The vesicular glutamate transporter 3-expressing amacrine cell (VG3) is one of only two amacrine types to express a vesicular glutamate transporter (Yan et al., 2020), and the VG3 is the only known amacrine cell to form both glutamatergic and glycinergic output synapses (Fremeau et al., 2002; Haverkamp & Wässle, 2004). The VG3 has a small to medium size arbor which stratifies loosely in the middle of the IPL, where the axons of transient OFF and ON bipolar cells terminate (Gong et al., 2006; Stella et al., 2008). The VG3 arbor spans ~100um, overlaps with neighboring VG3 (Keeley et al., 2021), and, interestingly, its branches do not form separate OFF and ON stratifications, but are instead closely connected with branches traveling between the two layers (Grimes et al., 2011). Whole cell recording using full field light stimuli found that VG3 receives transient excitation from OFF bipolar cells, but that that this is outweighed by stronger inhibition during both ON and OFF stimuli (Grimes et al., 2011).

Further characterization of the light responses revealed that the VG3 receives both ON and OFF transient bipolar inputs and will depolarize in response to small central stimuli. But when the size of the stimulus was increased beyond the size of the dendritic arbor, input inhibition quickly overtook excitation and large stimulus sizes hyperpolarized the cell (T. Kim et al., 2015). The same study went on to discover that VG3 can act as a differential motion sensor, or object motion sensor (OMS), which hyperpolarizes during global motion or motion in the surround but depolarizes in response to motion only in the center of its receptive field.

The VG3 targets multiple types of other retinal neurons with its object-motion channel of information. Optogenetic stimulation of VG3 elicited excitatory responses in several RGC types involved with detecting object motion and the direction of motion, the W3-RGC and ON and ON-OFF direction-selective (DS) RGCs, respectively (Lee et al., 2014). The W3-RGC is the most numerous RGC type in the mouse retina, and it selectively responds to small object motion against featureless or motionless backgrounds (Y. Zhang et al., 2012). Further, in a vGluT3 knockout mouse, the W3-RGC lost a significant portion of its object motion sensing ability, implying that VG3 provides the W3-RGC with an object-motion-specific excitatory drive (T. Kim et al., 2015).

Calcium imaging later revealed that VG3 has heterogeneous arbor responses in its branches which varies according to their depth in the IPL, with OFF branch regions having stronger OFF responses and ON regions having stronger ON responses (Chen et al., 2017). Further, stimulus size preference was also shown to vary with IPL depth. Critically, the VG3 plexus, with its branch region autonomy and intermixed inputs and outputs, maintains local

response polarity and size preference and can transmit this information to its target neuron types with either excitatory or inhibitory synapses (Hsiang et al., 2017).

An example of these local stimulus preferences is the robust response of the VG3 OFF branch regions to small expanding dark shapes, also called "looming" stimuli (T. Kim et al., 2020), which has been well characterized in evoking innate fear responses such as freezing and fleeing (Yilmaz & Meister, 2013). In fact, multiple RGC targets of VG3 have been shown to be involved in these behaviors (Münch et al., 2009; Wang et al., 2021), and removal of VG3 from an adult mouse reduces freezing in response to looming stimuli, but doesn't affect performance on other visual tests (T. Kim et al., 2020).

1.4 Object motion detection in the retina

From the perspective of the retinal neurons, the visual scene is in constant motion due to movement of the eyes, head, and body. Even when gaze remains seemingly fixed, constant miniscule movements of the eye ensure that, at the level of individual photoreceptors, illumination is perpetually changing (Ditchburn & Ginsborg, 1953). In fact, when the retinal image is experimentally held perfectly still, visual perception rapidly malfunctions (Coppola & Purves, 1996; Martinez-Conde et al., 2006).

From the perspective of an individual photoreceptor (i.e., a single location on the retina), all types of motion manifest as changes in local light levels. However, after computations performed within the retina by horizontal, bipolar, and amacrine cells (reviewed in (Masland, 2012)), retinal ganglion cells can discern whether motion is in their preferred direction (Rousso et al., 2016), determine whether motion in the center of their receptive field differs from motion in the surround (Krishnaswamy et al., 2015), or encode the size and speed of an approaching object (Wang et al., 2021). If an animal needs to visually detect moving objects in its

8

environment, such as predators or prey items, the ability to distinguish between retinal motion generated by the observer and retinal motion generated by the movement of objects in the visual scene is of paramount importance (reviewed in (Kerschensteiner, 2022)).

Determining the presence of a moving object amid the constant self-generated motion requires higher-level processing to compare motion in one area with motion in the areas around it. Some amacrine cells and RGCs are selective for this *local* motion, where a region of visual space moves differently than its surroundings (Jacoby & Schwartz, 2017). Several of these RGC types are heavily innervated by VG3, though they integrate VG3 excitatory inputs in slightly different ways. For the transient-OFF-alpha RGC and W3-RGC, the VG3 provides nearly half of the excitatory synaptic drive during object motion (T. Kim et al., 2020). In ON and ON-OFF DS RGC, the VG3 provides an excitatory drive selective for object motion, while other amacrine cells impart direction selectivity. Other amacrine types, such as the AII, TH2, and SAC, contribute to the response properties of these RGC types, though primarily through selective inhibition (Brüggen et al., 2015; Grimes et al., 2022; T. Kim et al., 2015; Park et al., 2014). In addition to its excitatory contributions to motion detection, the VG3 provides inhibitory drive to the PAS4/5, an amacrine cell (Jia et al., 2020), and the suppressed-by-contrast (SbC) RGC, both of which display suppressed-by-contrast response properties (Jacoby et al., 2015; Tien et al., 2015, 2016).

A special case of local object motion is when the object is moving directly towards the observer. This "looming" stimulus may indicate an approaching predator or object to be avoided, and quick and reliable detection is crucial to survival (Ölveczky et al., 2003). There is a characterized innate freezing or fleeing response in many animals, including human infants, to looming stimuli (Ball & Tronick, 1971; Koehler et al., 2019). This freezing behavior relies on

RGCs with axonal projections to the superior colliculus, specifically the W3 and transient-OFF-alpha RGCs (Lees et al., 2020; Reinhard et al., 2019; Shang et al., 2018; Yilmaz & Meister, 2013).

VG3 innervates both these RGC types with glutamatergic synapses, and if VG3 are ablated in an adult mouse, looming stimuli will no longer elicit freezing, and the excitatory drive to the two RGC types is reduced by nearly half (T. Kim et al., 2020). Conversely, when transient-OFF-alpha RGCs are optogenetically activated, fleeing behavior is elicited, even in the absence of any looming stimuli (Wang et al., 2021). The VG3 is crucial to the function of these circuits and has been shown to extensively use subcellular processing of visual information to contribute to both object motion detection and suppressed-by-contrast visual pathways.

1.5 Correlative Light and Electron Microscopy

The development of fluorescent calcium reporters, molecules which change fluorescence in the presence of calcium ions, enables imaging of calcium transients which precede vesicle fusion and the subsequent release of neurotransmitters at chemical synapses (Heidelberger et al., 1994; Katz & Miledi, 1967; Sabatini & Regehr, 1996; Südhof, 2012). Two-photon microscopy, when used with calcium reporters, can image local calcium levels subcellularly, within individual branch regions of neuronal arbors (Hsiang et al., 2017; Moore et al., 2022; H. H. Yang et al., 2016). Importantly, calcium imaging allows simultaneous characterization of dendritic responses across entire neuronal arbors at subcellular resolution, enabling examination of dendritic response heterogeneity (Denk et al., 1996; Denk & Detwiler, 1999; Euler et al., 2002; Weitz et al., 2013; H. H. Yang et al., 2016).

Electron microscopy (EM) is useful for imaging the ultrastructure of biological specimens and can resolve tiny structures such as individual synaptic vesicles and gap junctions between cell membranes (De Robertis & Franchi, 1956). In neuroscience, EM has been used to study the structure and location of chemical and electrical synapses on neuritic arbors for decades. Reconstructing neuronal arbors and the distribution of synapses on their branches requires extending EM into the third dimension and the imaging of a large number of serial tissue sections (reviewed in (Kubota, Sohn, & Kawaguchi, 2018)). Advances in computing, data storage and sharing, automated tissue sectioning, and serial electron microscopy have greatly reduced the necessary resources to image volumes of tissue large enough to contain entire neuronal arbors and even circuits (reviewed in (Xu et al., 2021)).

Correlated (or correlative) light and electron microscopy (CLEM) combines the strengths of light and electron microscopy techniques while supplementing the limitations of each other (reviewed in (de Boer et al., 2015)). Fluorescence microscopic techniques using genetically expressed tags, immunolabeling, or functional imaging of calcium, voltage, glutamate, and other fluorescent reporter molecules can record activity in live cells, monitor for specific timepoints, and locate rare targets or events (reviewed in (Padmanabhan et al., 2010)). Electron microscopy has the power to acquire images of structures too small to resolve with light microscopy, such as membrane structures, cytoskeletal elements, synaptic vesicles, and other ultrastructural features (Spira & Hollenberg, 1973). However, functional imaging and imaging of live specimens are not possible with electron microscopy, and specific staining must be accomplished using electron dense materials such as gold nanoparticles (Fairén et al., 1977).

In combination, two-photon calcium imaging and serial section scanning electron microscopy have specific utility in neuroscience for directly comparing the ultrastructure of a

neuron, i.e., the fine morphology of the neuronal arbor and the locations, directions, and sizes of the synapses on its branches, with how different parts of the arbor depolarize in response to stimuli (Friedrichsen et al., 2022).

1.6 Rationale and Goals of Current Studies

How a neuron integrates information depends on the distribution of synapses on its arbor branches and morphology and membrane electrical properties of those branches (Jones & Kording, 2022; London & Häusser, 2005). The same set of synaptic inputs could be integrated in vastly different ways depending on their distributions. Likewise, different arbor morphologies and arbor membrane properties can drastically change the way that an arbor computes the same set of inputs (reviewed in (Baccus, 2007)).

Vision relies extensively on subcellular processing in the retina to efficiently extract relevant information about the visual scene (Azeredo da Silveira & Roska, 2011). There are many specialized retinal neurons with distinctive arbor shapes and arrangements of various types of synaptic inputs and outputs which can extract streams of salient visual information under a wide range of lighting and environmental conditions (reviewed in (Dowling, 1999; Field & Chichilnisky, 2007; Masland, 2001)).

In the case of retinal amacrine cells, output synapses are often located on the same branches as inputs, so each output synapse has a unique perspective of arbor morphology and integrates inputs according to their proximity to its specific location (Anderson et al., 2011; Marc et al., 2014). The VG3 amacrine cell integrates information at this subcellular level, shown by its heterogeneous arbor branch responses to different aspects of light stimuli (Hsiang et al., 2017). The VG3 receives synaptic inputs from multiple sources (central ON excitation, central OFF

excitation, surround ON and OFF inhibition) and computes the presence of local object motion or looming. It then delivers appropriate ON or OFF versions of this object-motion-selective information channel to specific target types using either excitatory or inhibitory synapses.

To better understand how the VG3 segregates and integrates information from different sources within its arbor branches, we must examine both the functional responses and structure of the VG3 at the level of individual branch regions and synaptic connections. Both dendritic calcium imaging and serial section electron microscopy have been used successfully in the retina to examine other amacrine types. Also, correlative light and electron microscopy studies of retinal tissue in mice and rabbits have created excellent resources including experimental protocols, image processing and analysis tools, and massive open-access datasets describing the morphology and functional properties of thousands of bipolar and retinal ganglion cells, which can be drawn upon to aid in cell identification and analysis.

Our first aim was to map subcellular light responses from live VG3 arbors onto nanometer-scale reconstructions of those same arbors, allowing us to know the precise branch structure and synaptic environment underlying the observed response patterns. To accomplish this, we developed a multiresolution correlated light and electron microscopy (mrCLEM) approach which successfully mapped calcium imaging and structural 3D light microscopy imaging onto 3D-EM reconstructions of VG3 arbor morphology and synaptic connectivity at the level of individual neurites. Using this method, we were reliably able to locate optically imaged VG3 soma and even individual neurites within our 3D-EM volume.

Our second aim was to define the functional neighborhoods within the VG3 arbor. Different regions of VG3 arbor respond differently to light stimuli, despite being in proximity to each other on a single contiguous neuronal arbor. How the arbor branch structure and input

13

synapses are arranged to be conducive to the observed dendritic autonomy is unknown. We first reconstructed VG3 arbors, their input synapses, and the presynaptic bipolar axons. We matched these reconstructions to the live calcium imaging, determining which branches exhibited which response patterns and the exact arrangement of input synapses producing the response. We used these input profiles, the distances between branch regions, and the ON OFF polarity of the light responses to determine the effective length constant of bipolar inputs within the VG3 arbor.

Our third aim was to determine whether the local environment affects selectivity in synapse formation. The VG3 receives ON and OFF excitatory inputs from bipolar cells and inhibitory inputs from other amacrine cells, and these are integrated into different output channels that are targeted to multiple amacrine and RGC types in local object motion and suppressed-by-contrast pathways. However, it is not known if inputs and outputs with specific cell types are clustered together to form specialized input-output pathways. We calculated density recovery profiles for different synapse types on distal branch tips to determine whether tip domains form synaptic motifs different from the rest of the arbor. Also, for each RGC output synapse, we calculated the relative influence of the different types of bipolar inputs. We then randomly redistributed synaptic inputs and outputs on the VG3 arbor branches, preserving their approximate IPL depth, to determine whether the distribution of synapses could be explained by costratification alone.

Chapter 2

Reconstructing Neural Circuits using Multiresolution Correlated Light and Electron Microscopy

2.1 Introduction

Electron microscopy (EM) can reveal the complete nanoscale arrangement of cells and organelles in a piece of tissue. Cells and subcellular structures are distinguished not by selective labeling, but by brute resolving power. Three dimensional EM (3DEM) is therefore ideal for mapping the dense networks of fine neurites and synaptic connections that delineate the flow of information through nervous tissue (Morgan & Lichtman, 2013). While this technique has been the gold standard for describing the synaptic connectivity of neurons for more than 60 years (Sjöstrand, 1958), obtaining the thousands of images required to reconstruct the synaptic connectivity of a significant proportion of even one neuron was extremely labor intensive (Famiglietti, 1991; Freed & Sterling, 1988; Hamos et al., 1985; White et al., 1986). Advances in EM tissue processing, imaging, and data management have made it feasible to digitize large volumes of neural tissue (3DEM) and reconstruct their circuitry (Bock et al., 2011; Hayworth et

al., 2014; Helmstaedter et al., 2013; Jain et al., 2010; Januszewski et al., 2018; Kasthuri et al., 2015; Morgan et al., 2016; Morgan & Lichtman, 2017; Turaga et al., 2010; Yin et al., 2020).

Chief among the tissue processing advances is automatic sectioning. Currently, the most common automated approach to sectioning is blockface EM where the surface of tissue block is removed with a diamond knife or focused ion beam so that the underlaying tissue is exposed for imaging with scanning electron microscopy(SEM) (Briggman et al., 2011). Sequential surface removal and imaging produces 3DEM volumes. Not having to deal with ultrathin sections eliminates many of challenges of traditional serial section electron microscopy, but it also eliminates the option to reimage tissue as the EM reconstruction provides more information about the tissue. An alternative approach, and the one applied here, is the automated collection of sections. The automated tape collecting ultramicrotome (ATUM) adds a conveyor belt to the back of the diamond knife waterboat in which ultrathin sections are traditionally collected (Hayworth et al., 2014; Schalek et al., 2012). This conveyor belt picks sections up as they are cut so that thousands of ultrathin sections can be cut and collected without stopping and starting the microtome and without manual intervention. Sections collected onto tape can be imaged either with SEM or transmission electron microscopy (TEM).

The primary limitations in studying the nervous system with 3DEM are: 1) Image volume size is limited by the long acquisition times, large data sizes, and long analysis times demanded by high pixel densities. 2) The tissue is fixed, metalized, plasticized, and sectioned so live imaging is not an option. 3) Labeling specific molecules, usually by antibody labeling, is challenging due to the heavy fixation and staining required for high-throughput EM. The heavy osmium staining provides enough signal for fast imaging but interferes with antibody binding. These limitations can be overcome by first imaging a piece of neural tissue optically and then

16

reconstructing targeted regions of the same tissue by 3DEM (Bock et al., 2011); a technique

called correlative light electron microscopy (CLEM) (de Boer et al., 2015). Optical data can

provide dynamic morphological, physiological, and molecular characterizations of neurons that

can then be mapped onto high-resolution EM anatomical reconstructions.

A major challenge of CLEM is targeting; directing high-resolution EM image acquisition

to the optically characterized region of the tissue and then locating optically characterized

neurons or synapses within the EM volume. In EM techniques in which the tissue is destroyed

during imaging (blockface scanning) care must be taken to identify landmarks during the single

pass of cutting that can be used to direct high resolution imaging. In techniques where sections

are preserved and imaged (serial section EM), targeting can be labor intensive because

landmarks must be identified in two dimensional images and extrapolated across thousands of

sections (Morgan et al., 2016).

One approach to CLEM targeting is to label tissue with a stain that is visible in both light

and electron micrographs. Most of these approaches involve labeling a cell with something that

will catalyze the oxidation of a diaminobenzidine (DAB) solution to produce precipitate that is

visible both optically and in tissue processed for electron microscopy. The approach commonly

used in electrophysiology is to label a cell by filling its recording electrode with horseradish

peroxidase (HRP) (Robson et al., 1978). Horseradish peroxidase (HRP) can also be bound to

antibodies to label specific proteins (Trachtenberg et al., 2002). Transgenic approaches to driving

the DAB reaction (mHRP (Li et al., 2010), miniSog (Shu et al., 2011), or APEX (Lam et al.,

2015; Martell et al., 2012; Q. Zhang et al., 2019)) can produce optical and EM labels targeted to

specific cell types or organelles. A wide range of fluorescent dyes can also drive the DAB

reaction directly through photoconversion (Maranto, 1982). One of the limitations of the DAB

approach to CLEM is that the DAB precipitate can obscure ultrastructural detail. Labeling native proteins or transgenic labels with electron-dense nanogold conjugated antibodies avoids the precipitate (Faulk & Taylor, 1971), but traditionally requires membrane permeabilization for non-surface labeling (see (Fulton & Briggman, 2021) for alternative). Light and EM visible fiducials can also be introduced with the optical microscope itself in the case of near-infrared branding (NIRB) (Bishop et al., 2011). The collection of electron-dense optical label approaches is varied, but these approaches suffer from the limitation that optimal tissue processing for generating the EM label diverges from the optimal tissue parameters for high-contrast / high-throughput 3DEM reconstruction of intact neuronal circuits.

A second approach for matching light and EM is to optically map ubiquitous biological features that can be recognized in an electron micrograph by their pattern (pattern matching vs label matching). Blood vessels and cell nuclei are attractive targets for this mapping as they are easy to label with fluorescent stains, are visible in any 3DEM preparation, and span pattern matching scales from centimeters to micrometers (Vishwanathan et al., 2017). Specific labeling and imaging of these features was successful in previous large-scale reconstructions of functionally characterized neural circuits (Bock et al., 2011). A principal challenge of this pattern matching approach is the difficulty in acquiring and annotating EM images that can be matched to optical images across a range of scales (millimeter to nanometer). Large EM fields of view are required for matching blood vessel morphology, while high-resolution images are required for reconstructing and matching neurite morphology. Furthermore, if optical images, EM images, and matching features do not all lie in the same plane, then 3D reconstruction of light and EM volumes may be required before correspondence can be identified.

Multi-shot EM imaging approaches allow for the same sections to be imaged multiple times at different resolutions and then matched to complimentary sets of optical images (Schifferer et al., 2021). Here we describe a multiresolution CLEM (mrCLEM) workflow, which combines 3D confocal maps of fixed tissue with automated-tape collecting ultramicrotomy (ATUM). ATUM preserves large numbers of ultrathin (~30-40 nm) sections on a stable substrate and is, therefore, uniquely suited for repeated imaging and mrCLEM (Hirabayashi et al., 2018; Schifferer et al., 2021; Snaidero et al., 2020). By combining ATUM with confocal mapping of dense features, we can first match the vasculature in a ~1000-nm resolution 3DEM volume to the vasculature of optical images of the same tissue, then match cell bodies and large neurites in a ~20-nm resolution 3DEM volume, and finally match fine neurites in an embedded 4-nm resolution 3DEM volume. In our workflow, we use 2-photon imaging for live imaging (penetration and repeated imaging without out-of-focus bleaching) and confocal imaging for mapping reference features in fixed tissue (4+ channel imaging, spectral separation, reflected light).

Below, we provide a guide to this approach as well as examples from mouse thalamus and mouse retina. To demonstrate the range of scale and modalities applied to a single piece of tissue, we walk through one CLEM experiment from the beginning. In this experiment, the response properties of the neurites of retinal amacrine cells are characterized with live 2-photon calcium imaging. The same neurites are then targeted for 3DEM circuit reconstruction. We also provide examples multiresolution CLEM is used in brain slices where 3DEM is used to examine the synaptic connectivity of retinal ganglion cell axons that have been fluorescently labeled according to whether they originate from the left or right eye.

2.2 Materials and equipment

Optical Microscopy Reagents: DAPI (Invitrogen D1306), Sulforhodamine (Chemodex S0025), FluoroMyelin (Invitrogen F34652).

Electron Microscopy Reagents: Paraformaldehyde (EMS, 16714), glutaraldehyde (EMS 50-262-17), calcium chloride (VWR BDH7308-1), phosphate buffer saline (Genesee Scientific 25-507B), sodium cacodylate (Fisher Scientific International 50-366-664), osmium tetroxide (Fisher Scientific Inc 50-332-09), ferricyanide (EMS 20150), pyrogallol (SIGMA 16040), thiocarbohydrazide (EMS 21900), maleate buffer (EMS 11730-08), uranyl acetate (Fisher Scientific International 22400-4), lead nitrate (EMSURE 10099-74-8), aspartic acid (SIGMA-Aldrich A93100), acetonitrile (Fisher Scientific International 50-980-146), Spurrs (EMS 14300), EMbed 812 (EMS 14121).

Tissue Preparation: For functional imaging, mouse retinas were isolated via dissection under infrared binocular stereo microscope. The retinas were immersed in mouse artificial cerebrospinal (mACSF) fluid buffered with sodium bicarbonate throughout the dissection and imaging. $mACSF_{NaHCO3}$ contained (in mM) 125 NaCl, 2.5 KCl, 1 $MgCl_2$, 1.25 NaH_2PO_4, 2 $CaCl_2$, 20 glucose, 26 $NaHCO_3$ and 0.5 L-Glutamine equilibrated with 95% O_2/5% CO_2. Retinas were flat mounted on transparent membrane discs (Anodisc 13, Whatman, Maidstone, UK, for two-photon imaging) or membrane disks (HABGO1300, MilliporeSigma, Burlington, MA, for confocal imaging).

For obtaining fixed dorsal lateral geniculate nucleus (dLGNs) of the thalamus, mice were transcardially perfused using a NE-1000 Single Syringe Pump (SyringePump.com, Farmingdale, NY)(Morgan et al., 2016). Sections were cut using a Compresstome vibratome (Precisionary VF-200-0Z).

Two-photon microscope: Two-photon images were acquired with a custom-built upright two-photon microscope (Scientifica, Uckfield, UK) and a Mai-Tai laser (Spectra-Physics, Santa Clara, CA). The microscope is controlled by the Scanimage r3.8 MATLAB toolbox (Pologruto et al., 2003).

Confocal microscope (For optical correlation mapping): We acquired confocal micrographs with an Olympus FV300 and an Olympus FV1000. The flexible emission filter settings of the FV1000 are helpful for imaging reflected light and autofluorescence. To image reflected light it is necessary to be able to adjust (or remove) emission filters so that light of the laser's wavelength can reach the detectors. For imaging autofluorescence, it is helpful to be able to set emission filters to capture as much light as possible while excluding the laser lines.

ATUM powertome: ATUM is a reel-to-reel conveyor belt that fits in the boat of an ultramicrotomy diamond knife (Baena et al., 2019; Hayworth et al., 2014; Schalek et al., 2012). Ultrathin sections float across the water's surface in the diamond knife boat and are either directly deposited on the conveyor belt as they are cut or are pushed onto the tape by the subsequent section. The ATUM allows for the continuous collection of sections in an isolation chamber, making it easier to collect long series of ultrathin sections (30-45 nm) with minimal section loss. This technology can be used to collect sections for both scanning electron microscopy and transmission electron microscopy. For scanning electron microscopy, we collect sections on conductive Kapton tape (Sheldahl). The conductive tape used in the datasets here was 8 mm wide Kapton tape coated with carbon in the laboratory of Jeff Lichtman or aluminum (Sheldahl, Northfield MN). Excellent performance can be obtained using carbon nanotube tape (Kubota, Sohn, Hatada, et al., 2018) commercially available through RMC Boeckeler (Tucson, AZ). Collecting sections on tape for scanning electron microscopy preserves sections on a stable

substrate that can be reimaged many times over many years (Hildebrand et al., 2017). For transmission electron microscopy, sections can be collected on tape that includes electron-lucent film-filled holes (Graham et al., 2019).

Ultramicrotome: An RMC Powertome is sold in conjunction with the RMC ATUM. The ATUM is also compatible with other microtomes. We used a Leica UC7 ultramicrotome for most of the work presented here. We trimmed section blocks with glass knives and a 90 degree or 20-degree Diatome (Hatfield, PA) trimming diamond knife. We used Diatome Ultra 45 and 35 knives for ultrathin sectioning. After sectioning, we cut the collection tape and mounted it onto conductive 4-inch diameter silicon wafers (University Wafer, South Boston, MA) using conductive carbon adhesive tape (EMS, Hatfield, PA).

Zeiss Merlin scanning electron microscope (SEM): The Merlin is a single beam field-emission scanning electron microscope. It is particularly well suited to multiresolution SEM as it allows for more than an order of magnitude range of electron currents, voltages, depths of fields, and working distances (see table). For instance, we mapped 4-inch wafers at low resolution using 10 mm wide field of view (FOV) mosaic tiles with high current (giving high signal, low resolution) and long working distances (wide FOV, low resolution) in high depth of field mode (high depth of field, low resolution)(Table 1). Once the target is identified, the small electron beam spot sizes (<1 - 20 nm depending on conditions) that are required for high-resolution imaging are obtained by reducing current and working distance and switching to high-resolution or analytic mode. We also use an Ibss plasma asher (Burlingame, CA) to plasma treat sections prior to imaging. This process increases sample contrast by etching plastic and removes surface contaminants that could cause burning during imaging (Morgan et al., 2016).

2.3 Methods

Our multiresolution CLEM approach depends on acquiring a large series of images at multiple scales across multiple modalities (Figure 2.1). The CLEM experiment we describe in the greatest detail begins with live two-photon calcium imaging of mouse tissue. A similar approach may be used with any optical characterization that does not damage tissue ultrastructure. The key links to efficiently combining light and electron microscopy in this approach are: 1) the acquisitions of fixed tissue 3D confocal microscopy feature maps at low resolution (cell body resolution) and high resolution (subcellular features) and 2) the ability to acquire fast, low resolution, large FOV electron micrographs (cell body resolution) of sectioned tissue prior to acquiring high-resolution (cell membrane resolution) electron micrographs.

We do not quantify the precise resolution limits for each mode of imaging discussed here because the functional resolution will vary according to experiment specific details. Roughly, the "high-resolution" optical imaging in this pipeline peaks at about 0.2 x 0.6 mm for a point spread
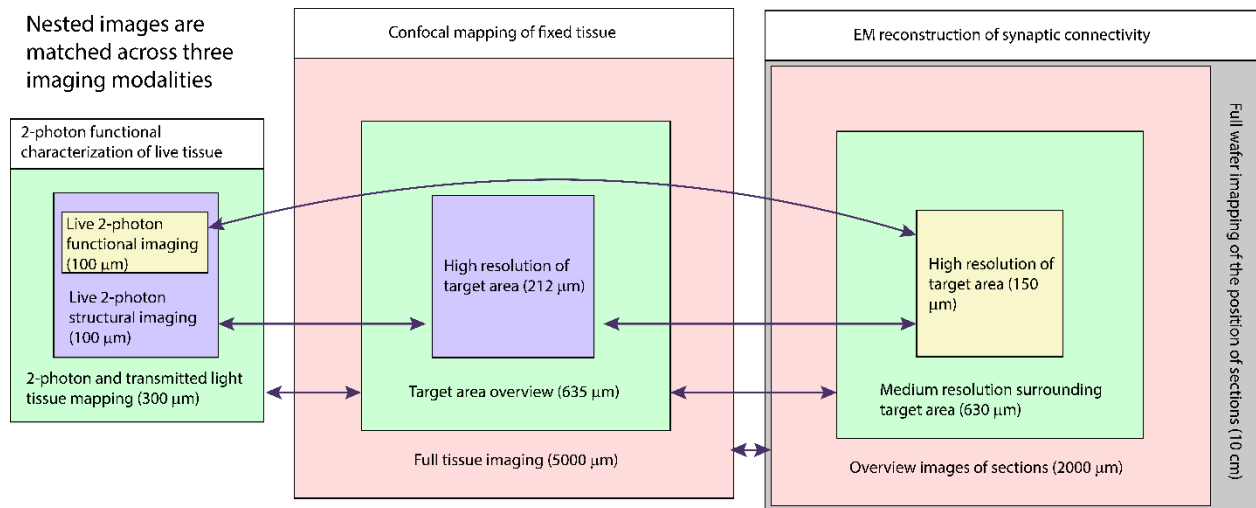
Figure 2.1. Schematic of multiresolution correlated light to EM. Nested image sets are shown for live 2-photon imaging (left), confocal mapping of fixed tissue (middle) and EM of synaptic connectivity (right). Matched image scales are indicated by color. The high-resolution image stacks providing the functional and connectivity data for the targeted cells are highlighted in yellow. Arrows indicate which images are typically compared for matching between modalities. From Friedrichsen et al, 2022.

function from confocal imaging with 60x 1.4na objective. This resolution is helpful for matching subcellular optical features such as neurites and synapses to EM reconstructions. We use a scanning electron microscope that is capable of sub-nanometer spot sizes. However, our imaging conditions balance resolving membranes with speed of imaging (more electrons = less resolution) so that our normal "high-resolution" EM spot size is about 8-15 nm across. For most image acquisitions, we follow the rule-of-thumb of choosing pixel sizes that double-sample the spot size.

All procedures in this study were approved by the Animal Studies Committee of Washington University School of Medicine (Protocols #20-190198 and #20-0055) and performed in compliance with the National Institutes of Health *Guide for the Care and Use of Laboratory Animals*.

Live two-photon imaging

Two-photon imaging can record activity in neurons expressing the calcium sensor GcamP6. The same microscope can image structural landmarks using fluorescence or transmitted light. One of the principal concerns in using 2-photon imaging in CLEM is that extended exposure of cells to the 2-photon laser can cause tissue damage. The need for higher signal (more laser power) and stimulus repeats (number of laser exposures) must weighed against the effects of the laser on tissue ultrastructure.

In our example experiment, calcium responses were imaged from retinal neurons using GCamp6f (Ai148 strain, Jax #030328 crossed to Vglut3-IRES2-Cre-D, Jax # 028534). Retinas were prepared for live imaging as described in Hsiang et al. 2017. Twelve sites (two XY positions, six depths, 100 x 13 µm each) were imaged at 9.5 Hz using 930 nm two-photon

excitation (Figure 2.2A) while visual stimuli were projected onto the retina. The overall laser intensity at the tissue was kept below 6 mW. The total functional imaging time for the twelve sites was 49 minutes with each site imaged for ~3 minutes.

After functional imaging, 3D two-photon image stacks were acquired that encompassed the functional ROIs (Figure 2.2A). These larger field of view stacks (100 and 300 µm XY, 40-50 µm in depth, Table 1) provided the 3D morphology of the functionally characterized cells that is later matched to 3DEM reconstructions of the same cells. These image stacks included a channel that collected transmitted laser light. The transmitted light reveals the vasculature surrounding the functionally characterized neurons (Figure 2.2A). Transmitted light images were bandpass filtered using a difference of gaussian kernel to enhance the visibility of blood vessels (see methods). After the 3D image stacks of the functionally characterized region were acquired, the target area was mapped relative to larger landmarks by acquiring a series of partially overlapping
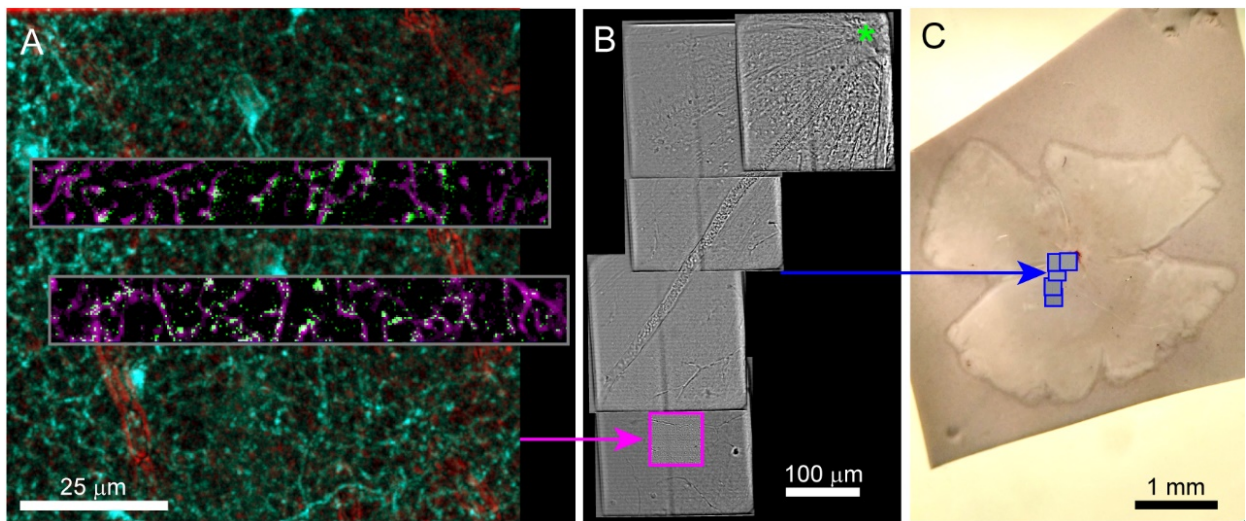
Figure 2.2. Live imaging of a retinal explant. A) Two-photon imaging of calcium responses (grey inset, single frame = green, time average = magenta) to visual stimuli acquired in two rectangular ROIs and at multiple depths in the retina. Functional ROIs are aligned within two-photon structural images of the surrounding transgenic expression of the calcium indicator (2-photon) in cyan and blood vessels (scanning transmitted) in red. Blood vessels in transmitted light images are enhanced using bandpass filtering. B) Scanning transmitted light images (grey, acquired on 2-photon microscope) are used to map the position of the characterized cells (pink box) relative to the optic nerve head (green asterisk). C) The blue boxes map the position of the grey images on the left onto the widefield transmitted image of the entire retina. From Friedrichsen et al, 2022.

full-field (300 x 300 μm^2) images. These images linked the target area to blood vessels, the optic disc, and the borders of the retina (Figure 2.2BC). If no gross anatomical features exist that can be used to keep track of the orientation of the tissue, large-scale landmarks can be cut into the tissue either immediately before or after fixation.

Dense feature labeling in fixed tissue

Mapping fixed tissue for CLEM using confocal microscopy has the advantage of 1) Multiple channels of information can be collected, 2) Optical sectioning enables easy 3D reconstruction, 3) Optical sectioning reduces out-of-focus light from glutaraldehyde. In widefield examinations of glutaraldehyde fixed tissue, background fluorescence can overwhelm signals from fluorescent labels and can discourage researchers from attempting optical imaging of tissue that has been fixed for electron microscopy. Confocal and two-photon imaging remove most of the out-of-focus, non-specific glutaraldehyde fluorescence leaving only the in-focus signal and background. Glutaraldehyde background signal can also be mitigated by initially fixing the tissue in lower concentrations. During initial aldehyde fixation, we used 1% glutaraldehyde and 2.5% paraformaldehyde (PFA), instead of the standard 2%/2%. For tissue that is tolerant phosphate-buffered saline (PBS), we perform our initial fixation in 0.1M PBS instead of the standard 0.1 M cacodylate buffer to reduce the exposure of microscopists to arsenic during optical mapping. After optical mapping, the tissue can be fixed again in 2% PFA, 2% glutaraldehyde in 0.1 M cacodylate buffer.

For confocal imaging, we mount tissue on a slide with a bridged coverslip for high NA oil objective imaging. Mapping can also be performed with high NA dipping cone objectives to minimize mechanical and osmotic stress on the tissue. The quality of optical maps can be
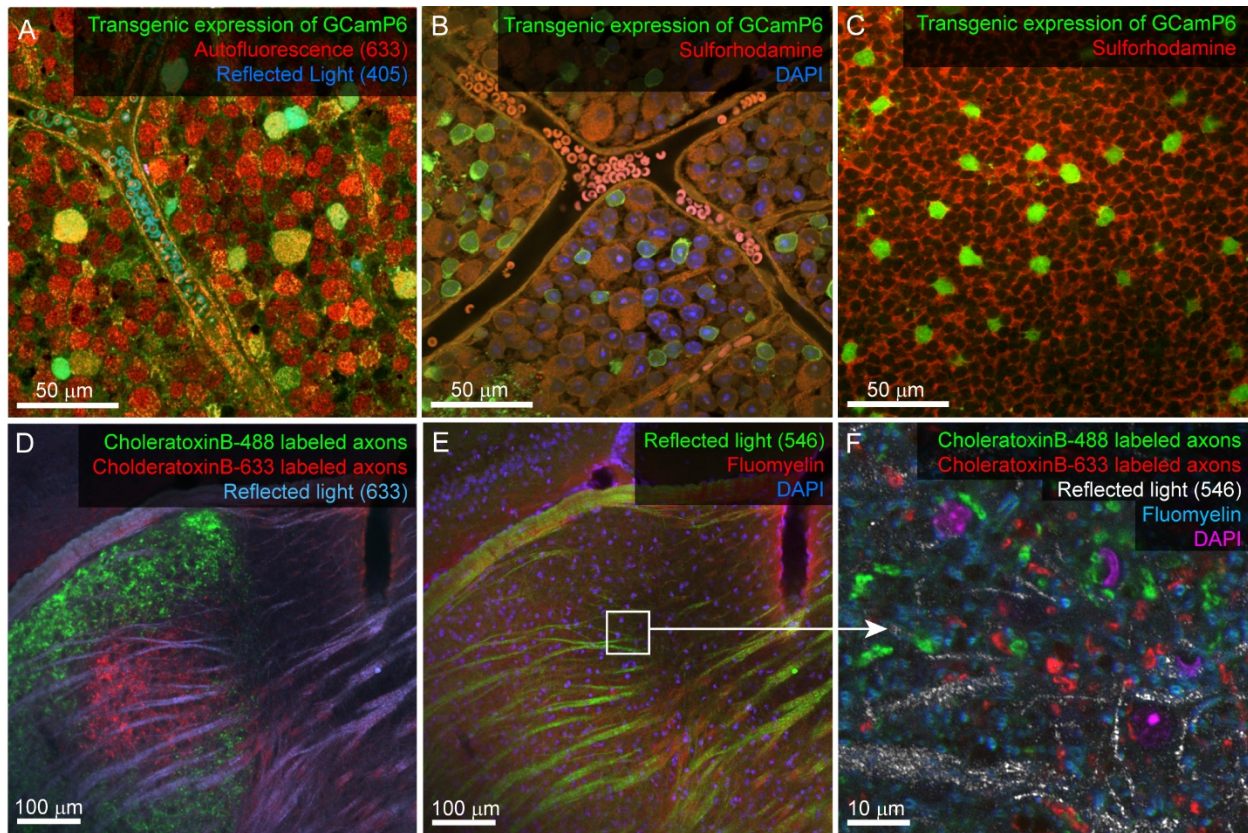
Figure 2.3. Multiscale anatomical features for mrCLEM mapping. Example confocal imaging of fixed retina (top) and visual thalamus (bottom) to map features for mrCLEM. A) Imaging of the ganglion-cell-side surface of a mouse retina (transgenic labeling green) with reflected 405 laser line (blue) and autofluorescence from the 633 laser line (red). Note clear cell bodies and vasculature. B) Imaging of the ganglion cell layer in mouse retina (transgenic labeling green) with Sulforhodamine (red), and DAPI (blue). C) Same tissue as panel B imaged 50 µm deeper in the inner nuclear layer. D) and E) Six-channel tissue mapping of a vibratome section of mouse dorsal lateral geniculate nucleus. D) Retinal ganglion cell axons from the contralateral eye labeled with CtB-488 (green), and the ipsilateral eye labeled with CtB-633 (red). Fiber tracks (blue) are imaged using reflected 633 laser line. E) Same image stack as panel D, showing DAPI (blue), FluoroMyelin (red), and 546 reflected light (green). White box indicates the field of view for panel F. F) Single plane from a high-resolution image stack acquired at the white box in E. High-frequency matching features (FluoroMyelin = cyan, retinal ganglion cell synaptic boutons = red and green) are shown in the context of medium-resolution features, (DAPI stained nuclei = magenta) and large-scale features (fiber tract = white). From Friedrichsen et al, 2022.

improved by partially clearing the tissue in 20-47% thiodiethanol (TDE) for ~20 minutes

(Aoyagi et al., 2015). This treatment improves resolution and imaging depth while minimally

distorting tissue (less distortion at 20%) and works well in CLEM studies (Costantini et al.,

2015). Because of light scatter in incompletely cleared tissue and the working distance of high-

resolution oil objectives, we only acquire high resolution features from the surface (<100 mm) of

27

the retina or brain slice. It is therefore important to map the surface that includes the cells of interest. More complete tissue clearing and/or 2-photon imaging can be used to extend the depth of high-resolution mapping.   Confocal mapping aims to produce a set of nested feature maps that link millimeter-scale features to micrometer-scale subcellular features. The mrCLEM features used here include (from large-scale to small-scale): 1) Gross morphology, 2) Fiber tracts, 3) Blood vessels, 4) Cell nuclei, 5) Cell bodies and neurites of labeled neurons, 6) Organelle stains (Table 2, Figure 2.3).

A considerable amount of unlabeled 3D structural data can be obtained from most fixed tissue using intrinsic signals. The autofluorescence of aldehydes reveals neuropil and cell nuclei (by the absence of signal). We generally image autofluorescence using 633 nm wavelength laser excitation and collecting all light longer than 633 nm (Figure 2.3A). Reflected laser light itself can also reveal various features, including blood vessels and fiber tracts. We usually acquire a reflected light signal by scanning with the 405 nm laser line and no barrier filter (Figure 2.3A,D,E). The reflected light signal is biased towards surfaces parallel to the imaging plane and

Signal source	Biological feature
Fluorescent protein expression	Cytosolic fill of targeted neurons
Transmitted light	Gross morphology, blood vessels
Aldehyde autofluorescence	Gross morphology, blood vessels, cell nuclei
Reflected light	Gross morphology, Myelination
DAPI	Cell nuclei, chromatin distribution
Sulforhodamine	Extracellular stain (live), Heterogeneous intracellular stain (fixed), Blood vessels
Fluoromyelin	Myelin
Fluorescent Choleratoxin B	Anterograde axon tracer

Table 2.1. List of optical imaging signal sources and typical features labeled for our light to EM feature mapping. From Friedrichsen et al.,2022

near the surface of the tissue. Most laser lines can be used to acquire both autofluorescence and reflected light, however, including high resolution reflected light (405 nm) and tissue penetrating

Image	Objective	FOV Size (µm)	voxel size (µm)	excitation wavelength (nm) electron voltage (keV)	Approximate Acquisition time	dwell time (µs x Kalman)
Live Two-photon functional imaging	60x 1.35nA	X = 100 Y = 13 Z = ~	X = 0.4 Y = 0.4 Z = ~	933 nm	49 min	2
Live Two-photon structural imaging (fluorescence and transmitted)	60x 1.35nA	X = 100 Y = 100 Z = 40	X = 0.2 Y = 0.2 Z = 0.2	933 nm	40 min	2
Live Two-photon tissue mapping (fluorescence and transmitted)	60x 1.35nA	X = 300 Y = 300 Z = ~50	X = 0.6 Y = 0.6 Z = 0.4	933 nm	40 min	2
Fixed optical confocal 10x map	10x 0.4na	X = 1270 Y = 1270 Z = ~	X = 0.600 Y = 0.6 Z = ~	405 nm, 488 nm, 635 nm	30 min	2
Fixed optical confocal 20x map	20x 0.8na	X = 635 Y = 636 Z = 96	X = 0.300 Y = 0.3 Z = 0.12	405 nm, 488 nm, 635 nm	1 hr	2 x4
Fixed confocal 60x map, intrinsic signals	60x 1.35na	X = 212 Y = 212 Z = 60	X = 0.100 Y = 0.1 Z = 0.3	405 nm, 488 nm, 635 nm	2 hr	2 x4
Fixed confocal 60x map, Sulforhodamine + DAPI	60x 1.35na	X = 212 Y = 212 Z = 60	X = 0.100 Y = 0.1 Z = 0.3	405 nm, 488 nm, 543 nm	2 hr	2 x4
EM overview images BSD or SE2 detector	37x	X = 2000 Y = 2000 Z = 42	X = 0.600 Y = 0.6 Z = 0.04	8 keV	7.5 hr	1
EM medium resolution BSD (targeting)	2500x	X = 164 Y = 164 Z = ~	X = 0.0440 Y = 0.04 Z = 0.04	8 keV	17 hr	0.3
EM High resolution	1900x	X = 120 Y = 120 Z = 42	X = 0.004 Y = 0.004 Z = 0.04	1 keV	6 weeks	0.2 - 0.4
EM medium resolution In Lens (large neurite reconstruction)	1500x	X = 630 Y = 630 Z = 34	X = 0.010 Y = 0.01 Z = 0.04	1 keV	3 weeks	0.1-0.2
EM medium resolution BSD (large neurite reconstruction)	350x	X = 630 Y = 630 Z = 8	X = 0.0110 Y = 0.01 Z = 0.04	8 keV	1 week	1

Table 2.2. Imaging conditions used for optical and EM imaging. To maximize resolution and prevent photo bleaching, we use low laser power and short dwell times for confocal imaging and then use Kalman averaging (2-6 repeats) to reduce noise. In fixed tissue with limited bleaching (GFP variants and Alexa dyes) we find repeated Kalman filtering works well. From Friedrichsen et al, 2022.

autofluorescence (633 nm) adds multiscale dense features to tissue labeled with more standard red and green fluorescent markers. Six channel imaging (2.3D,E) is accomplished by two serial scans using three lasers simultaneously in each scan. In this example DAPI and Fluoromyelin (blue and red) are acquired simultaneously as are Alexa 488 and Alexa 633 (green and far red). Channels collecting reflected light or autofluorescence can then be added to each scan without sacrificing scan speed, signal, or emission separation.

Reflected light and autofluorescence have the advantages of being quick, easy, and universal. Increased signal and additional feature selectivity can be achieved with stains. We find a combination of DAPI and Sulforhodamine particularly effective for performing mrCLEM (Table 3). DAPI staining has the advantage of revealing the pattern of chromatin density which varies between nuclei and is visible in low resolution (<1 µm pixel size) EM. DAPI does not seem to significantly impact ultrastructure (Tarnowski et al., 1991). In live
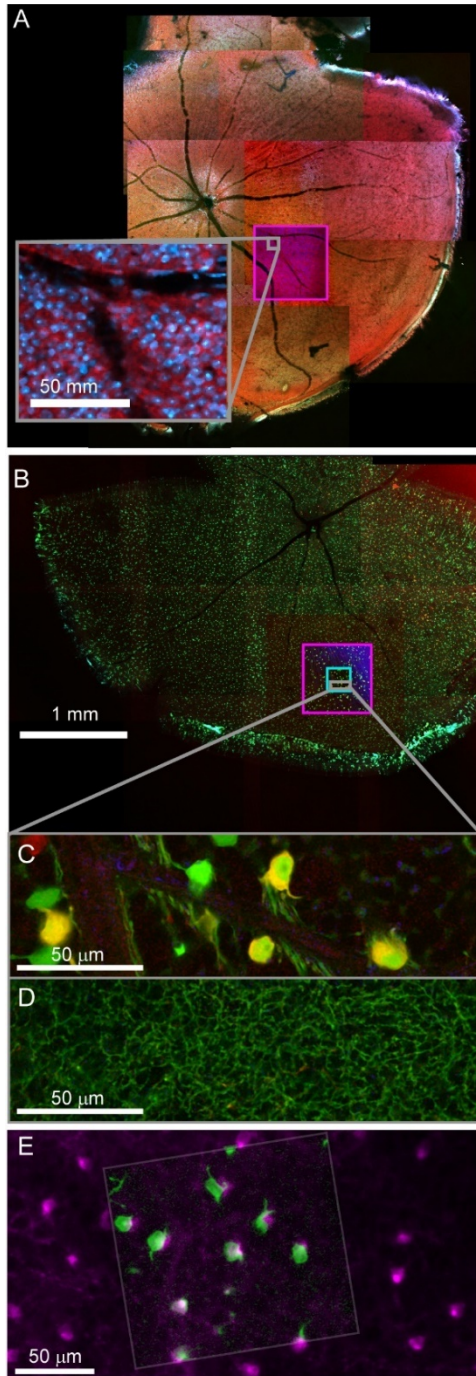
Figure 2.4. Confocal maps of fixed tissue. Low-resolution mosaics are acquired of the whole tissue, and higher-resolution image stacks are acquired that encompass targeted regions of interest. A) Mosaic of mouse retina stained with Sulforhodamine (red) and DAPI (blue). Pink box indicates targeting of image stack acquired with 20x objective. The grey insert provides a closer look at the images in the pink box. B) Mosaic of mouse retina transgenically expressing GCamp6 (green) and td-tomato (red). Pink and cyan boxes indicate targeting of 20x and 60x objective image stacks. C and D). Two planes of one high-resolution (60x) image stack with labeled cell bodies (C) and neurite plexus (D). E) Overlay of showing the alignment of cell body signal in a 2-photon live image of GCamp6 (green) and fixed confocal image stack of GCamp6 in the same region of tissue (magenta). From Friedrichsen et al, 2022.

tissue, Sulforhodamine is a primarily extracellular stain that labels blood vessels, astrocytes, or damaged cells (Schlichtenbrede et al., 2009). In fixed tissue, Sulforhodamine labeling in the cytosol is more common, such as in the case of retinal ganglion cells whose axons have been cut (Figure 2.3B). The resulting signal reveals blood vessels, nuclei (by their lack of labeling), and changes in tissue texture such as between neuropil and nuclear layers (Figure 2.3B,C). Additional organelle stains can generate higher frequency features for fine CLEM alignment. Here we show six-channel imaging of a brain slice where FluoroMyelin (ThermoFisher Scientific) generates dense optical labeling of myelinated axons in the visual thalamus (Figure 2.3D-F).

	0.1 M Cacodylate buffer or 0.1 M Phosphate buffer
5 min (3 times)	wash in buffer
1-24 hr	300 nM 4',6-diamidino-2-phenylindole (DAPI) in buffer. In 1h, the stain penetrates ~50 µm.
5 min (three times)	wash in buffer
5 min	7 µM Sulforhodamine 101 in buffer
	Rinse once without washing out stain

Table 2.3. Protocol for combined DAPI and Sulforhodamine stain. From Friedrichsen et al.,2022

Example of multiresolution optical mapping of functionally characterized mouse retinas

Fixed optical mapping begins with imaging the entire tissue (~4 mm wide for mouse retina) using a confocal mosaic of large field-of-view (FOV) tiles (10x objective, FOV = 1270 µm, pixel size = 0.6 µm) or wide-field epifluorescence scope. For a 150 µm thick retina, the gross morphology, blood vessels, and transgenic expression pattern could be mapped with one or a few z-planes per mosaic tile (fewer planes for gross morphology, more planes for cell bodies, Figure 2.4A,B). In confocal maps where transgenically labeled cell bodies are clearly visible, comparison of the fixed map to the live blood vessel map and live transgenic expression map are

sufficient to identify the cell bodies of the functionally characterized neurons in the confocal map. With the position of the functional ROIs identified, image stacks are acquired encompassing the target cells; a 635 µm FOV image stack acquired at 0.3 µm resolution (20x N.A. 0.85 objective) and a 212 µm FOV image stack acquired at 0.1 µm resolution (60x N.A. 1.35)(Figure 2.4C,D). Alignment of confocal and 2-photon stacks (Figure 2.4E) links the fixed confocal map to functional imaging. We chose imaging parameters to provide reliable reconstructions of neurites that could later be matched to both the structural two-photon images and EM reconstructions.

After confocal imaging, a subsection of the tissue (~1-5 mm x 1-5 mm) encompassing the region of interest is excised for EM processing. A scalpel is used to cut an asymmetric perimeter that can readily be used to identify the orientation of the tissue. Tracking this orientation makes it possible to position the tissue in an embedding capsule so that the tissue surface closest to the cells of interest can be targeted for selective cutting (if the whole depth of the tissue block is not required for reconstruction). Widefield imaging records the position of the tissue excision (Figure 2.5A). Images are also acquired during the trimming of the resin block to track the position of the optically characterized neurons (Figure 2.5B-D). The region of interest tracked first by comparing the borders of the excised tissue before and after embedding (Figure 2.5A vs B), then by aligning the borders of the resin block and trimming marks between stages of trimming (Figure 2.5B vs C), and finally by recording the position of the target area relative to the final blockface borders (Figure 2.5C vs D).
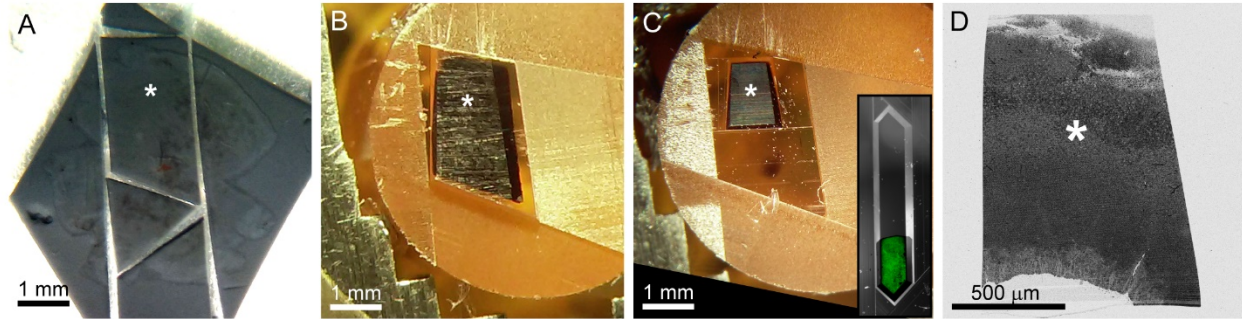
Figure 2.5. Tissue embedding in resin and blockface preparation. The optically characterized region of interest is excised from the aldehyde fixed tissue and processed for EM. A) A 2 mm x 3 mm asymmetric slab is excised from a retinal whole mount. Asterisk indicates the targeted region of interest in all panels. B) The tissue is stained and embedded in resin. C) The block is trimmed to a trapezoid approximately 800 µm x 1200 µm centered around the optically characterized region of interest. The grey inset shows how to trim a block (extended hexagon, different tissue block) for direct-to-tape automated cutting. The green channel shows that tissue features can be obtained from wide field reflected light imaging of the surface of a trimmed block face. D) Overview EM image of 40 nm-thick section taken from blockface in C. From Friedrichsen et al., 2022.

Tissue staining for electron microscopy

A significant advantage of mrCLEM is that it does not require additional EM labeling (e.g., metal particle antibodies, tissue marking, or DAB reaction). The EM staining protocol can therefore be optimized for maximum membrane staining (osmium tetroxide + osmium tetroxide + uranyl acetate + lead aspartate, Table 4) and integrity; properties critical for high throughput 3DEM circuit reconstructions. While the same mrCLEM approach can be implemented with different types of section preparation, producing high-contrast sections on a stable substrate is ideal for our multiresolution approach.

The protocol presented here is used for mouse retina, but also works well for vibratome brain slices by adjusting the osmium penetration times by approximately 1h/100 µm of penetration depth (Morgan et al., 2016).

	* All H₂O is filtered	
2 h	1% Glutaraldehyde, 2.5% Paraformaldehyde, 2 mM Calcium Chloride	RT
3 × 5 min	wash in 0.1 M Cacodylate buffer	RT
1 h	2% Osmium Tetroxide in 0.1 M Cacodylate buffer	RT
1 h	2.5% Ferrocyanide in 0.1M Cacodylate buffer	RT
5 × 10 min	wash 0.1M Cacodylate buffer	RT
20–45 min	0.1 – 1% Thiocarbohydrazide	40 C
5 × 10 min	wash H₂O	40 C
1 h	2% Osmium Tetroxide in H₂O	RT
5 × 10 min	wash with 0.05 Maleate Buffer	RT
12 h	1% Uranyl Acetate in 0.05 M Maleate Buffer	4 C
4 h	1% Uranyl Acetate in 0.05 M Maleate Buffer	50 C
5 × 10 min	wash with 0.05 Maleate Buffer	RT
5 × 10 min	wash H₂O	RT
10 min each	H₂O to Acetonitrile dehydration 30, 70, 80, 90, 95, 100%, (freshly opened) 100%, 100%	RT
> 2 h each	Acetonitrile: Resin, 3:1, 1:1, 1:3	RT
3 × 12 h	Pure Resin, rotating	RT
48 h	Polymerization in oven	60 C

Table 2.4. Generic protocol for heavy staining and resin embedding of tissue for electron microscopy. From Friedrichsen et al., 2022

The tissue is initially stained for 1 h in 2% osmium tetroxide (Table 4 for complete protocol). Following Hua (Hua et al., 2015), the osmium is then reduced with 2.5% ferrocyanide (ferricyanide is used in the EM images presented here but generally gives inferior results). After washout, the osmium linker thiocarbohydrazide (Tapia et al., 2012; Willingham & Rutherford, 1984) or pyrogallol (Genoud et al., 2018; Mikula & Denk, 2015) is used to bind a second layer of osmium to the first. The tissue is then treated with the second osmium stain, uranyl acid, and lead aspartate. Post-section staining with lead citrate (Morgan et al., 2016) can replace the lead aspartate staining to improve ultrathin sectioning and synapse labeling. The tissue is dehydrated in acetonitrile and embedded in Epon-812, Spurrs, or LX-112. In our experience, Epon-812 is reliable, but can produce large compression differences between tissue and non-tissue regions of

34

a blockface (leading to wrinkles). Spurrs and LX-112 (Wanner & Vishwanathan, 2018) tend to produce fewer wrinkles.

Tissue sectioning with Automated Tape Ultramicrotomy (ATUM)

Ultrathin sections are collected on conductive tape using the ATUM (Baena et al., 2019; Hayworth et al., 2014; Schalek et al., 2012). Tissue blocks are first trimmed either into a standard trapezoid shape or an extended hexagon (Morgan et al., 2016). Ideally, a trapezoid should be about 1.5 mm tall so that each section deposits the preceding section on the collection tape. Especially in the case of blockfaces wider than 1 mm, an extended hexagon face with a leading and trailing point can help with cutting reliability. The hexagonal block face must be long enough (>3mm) so that the section is picked up by the collection tape as it finishes cutting the section. For the retinal tissue, 40 nm thick sections were collected at 0.2 – 0.4 mm / second cutting speed. Thinner sectioning of a large section series is possible (10,000 sections at 30 nm, (Morgan et al., 2016)), but obtaining reliable sectioning is significantly more difficult below 40 nm and section quality degrades below 20 nm. Thicker sectioning can be appropriate for some tissue, but as sections become thicker, the range of membrane angles and neurite diameters that introduce reconstruction ambiguities increases. As most of the fine processes we are reconstructing in the mouse retina are ~100 nm diameter or larger, 40 nm section thickness provides a good balance of sampling frequency and sectioning reliability. In our experience, a fresh patch of a diamond knife can cut through approximately three meters of heavily stained tissue (3000 sections of a 1 mm tall piece of tissue from a >1mm wide block face) before knife wear prevents lossless ultrathin sectioning. Performance varies with the density and distribution of metal in the block.

During ultrathin sectioning, the water level in the knife boat is maintained automatically. Monitoring can be performed using software provided by Powertome or with our customizable Matlab water monitoring software (available here https://github.com/MorganLabShare/mrCLEM2021).

After collecting sections, the tape is cut and permanently attached to 10 cm wide silicon wafers using double sided vacuum-safe carbon tape (Schalek et al., 2012). The conductive surface of the Kapton tape is grounded by bridging all the tape surfaces to each other and to the silicon wafer with millimeter wide strips of conductive carbon tape. Wafer mounted sections (~100-200 per wafer) can be stored for years and reimaged many times (Hildebrand et al., 2017; Z. Liu et al., 2021). The primary limit to reimaging is that the sections can be damaged if intensive imaging interacts with contaminated surfaces. Allowing sections to outgas under vacuum for several hours or plasma cleaning the surface of the sections reduces this damage.

Electron micrograph tissue mapping

Wafers containing ultrathin sections are mapped using the custom Matlab package WaferMapper as previously described ((Hayworth et al., 2014), https://github.com/MorganLabShare/WaferMapper, Table 1). Section mapping and automated imaging can also be achieved using the array tomography software available with the Zeiss Merlin/Atlas system. Here, we use WaferMapper due to its customizability. For both accurate targeting and stitching tiles together, it is important that pixel positions accurately reflect stage positions. We, therefore, run a pixel-to-stage calibration between any change of imaging conditions (voltage, stage position, FOV) and data acquisition.

Image mosaics of the whole 10 cm wafer were acquired in the Merlin SEM using mosaics of 8 x 8 mm tiles at 8 µm pixel size (Backscatter detector, BSD). The full-wafer images are used to identify the positions of ultrathin tissue sections (Figure 2.6A). These section positions are then used to direct the automatic acquisition of section overview images (FOV = 3072 µm, pixel size = 0.75 µm, Figure 2.6B). The overview images can be acquired with the BSD detector (minimum imaging artifacts) or SE2 detector (fast). The overview images are then aligned to form a 3D map of the collected sections. Additional image stacks are acquired by defining points of interest within the aligned overview image volume.
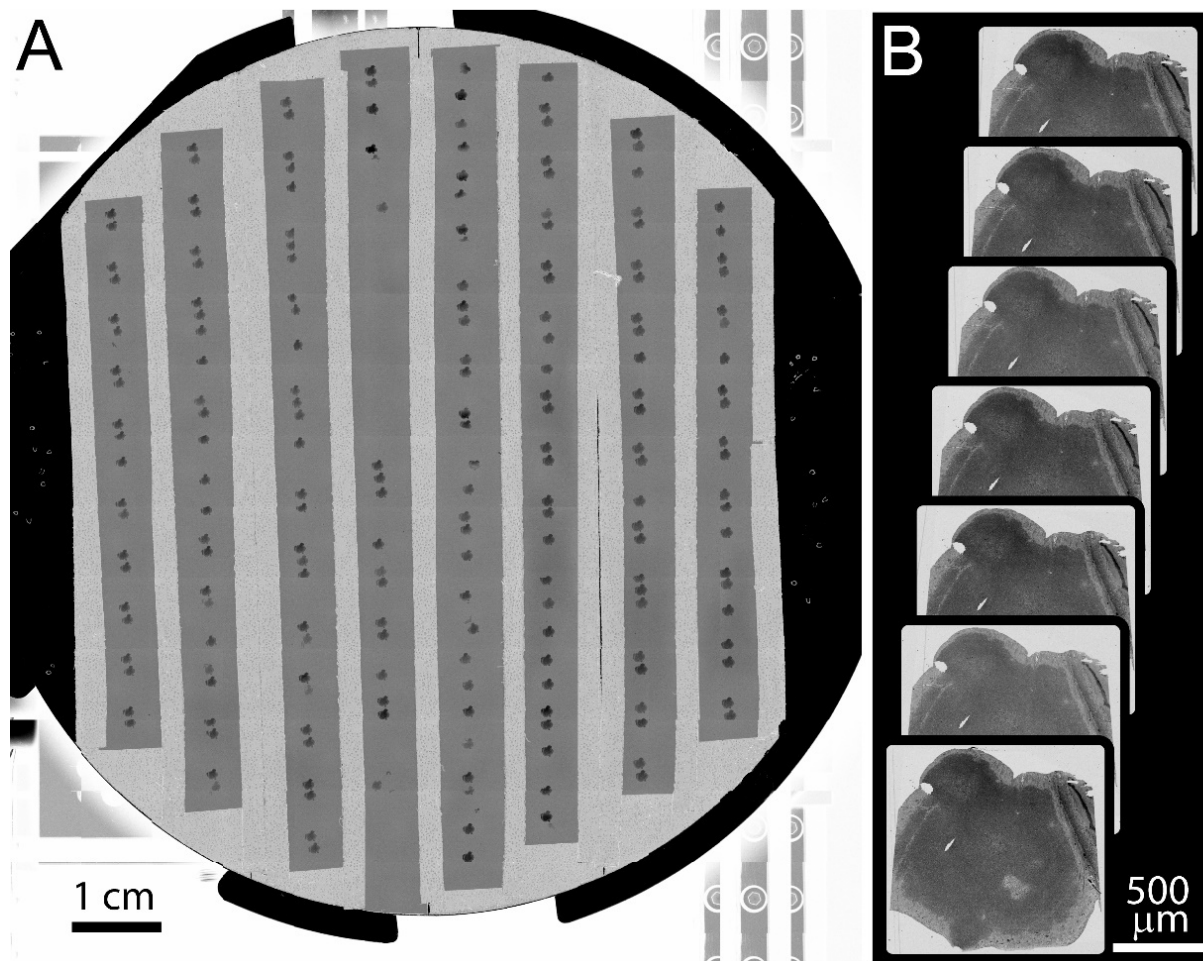
Figure 2.6. Example of full wafer image and section overview images. A) Full wafer EM image of the 10 cm wafer is acquired as a 14 x 12 tile mosaic. B) An overview image is acquired for each section. These overviews are then aligned to a template image to generate a 3D volume of the entire tissue. From Friedrichsen et al., 2022.

Gross morphology and blood vessels can readily be identified in the 3D alignment of overview images (Figure 2.7A-C). The EM images of these features can be matched to optical images of the same features. Manual matching of a small set of features by viewing the light and EM image stacks side by side (a few hours in ImageJ) is sufficient for picking ROIs for the next stages of higher resolution image acquisition.

Depending on the tissue and the quality of the overview imaging, it may be possible to identify cell nuclei well enough in the overview images to generate a nuclei-to-nuclei matching between the EM and optical maps. Otherwise, an additional medium-resolution EM image stack (FOV 630 µm, pixel size = 20 nm) can be targeted to the region of interest to align light and EM at the cell body level (Figure 2.7D-E). We match individual cells in light and EM images iteratively. In retinal tissue, we begin with matched blood vessels, then match nearby cell nuclei, then the nuclei close to those, continuing until we reach the cells of interest (<8 hrs, Figure 2.7G-H). Despite the structural uniformity within retinal layers, this method makes it relatively straightforward to identify the nuclei of optically characterized neurons in EM section space prior to high-resolution imaging. In other tissues, non-uniform features like myelinated axons tracts can make low resolution matching faster.

Once the relevant blood vessels, fiber tracts, and cell bodies have been matched between optical and EM tissue volumes, high-resolution image stacks (4 nm x 4 nm) can be targeted to individual optically characterized cells. For our high-resolution imaging conditions, the most efficient image tile size on our system is usually around 80 µm wide. Larger tiles reduce overlap in 2D mosaics and save tile to tile time, but image quality degrades with distance from the center of the FOV. Mosaics of these image tiles can be arbitrarily large, although automatic refocusing can become necessary for image tiles more than a hundred micrometers away from one another.

The critical limit to acquisition size for the single beam system is pixel rate. The Merlin SEM can acquire up to 20 million pixels per second (Morgan et al., 2016), however achieving enough signal to support these short dwell times is difficult, and image quality is likely to fall off at speeds greater than 5 million pixels per second. The limited pixel rate is made up for, to some extent, by the ease with which the single-beam SEM can reimage an area at a range of resolutions. Aside from being used to match optical features to EM, medium-resolution stacks (8-40 nm) can be used to trace relatively large features (such as large dendrites and myelinated axons) out of high-resolution volumes and across volumes too large to be imaged at high-resolution.

Image processing

For some optical images, we use median filters to reduce noise, FFT bandpass filters (ImageJ) or difference-of-gaussian filters (Matlab) to enhance signals at select frequencies, and/or edge detection (ImageJ) to enhance blood vessels. Frequency enhancement is particularly useful in emphasizing blood vessels in transmitted light images and enhancing cell nuclei in images with very low signal. For difference-of-gaussian filtering, the size of the central gaussian is chosen to match the size of the feature of interest (sigma ~5-10 mm, for blood vessels and cell bodies). The subtracted surround was a gaussian with a larger sigma. We tuned kernel sizes empirically.
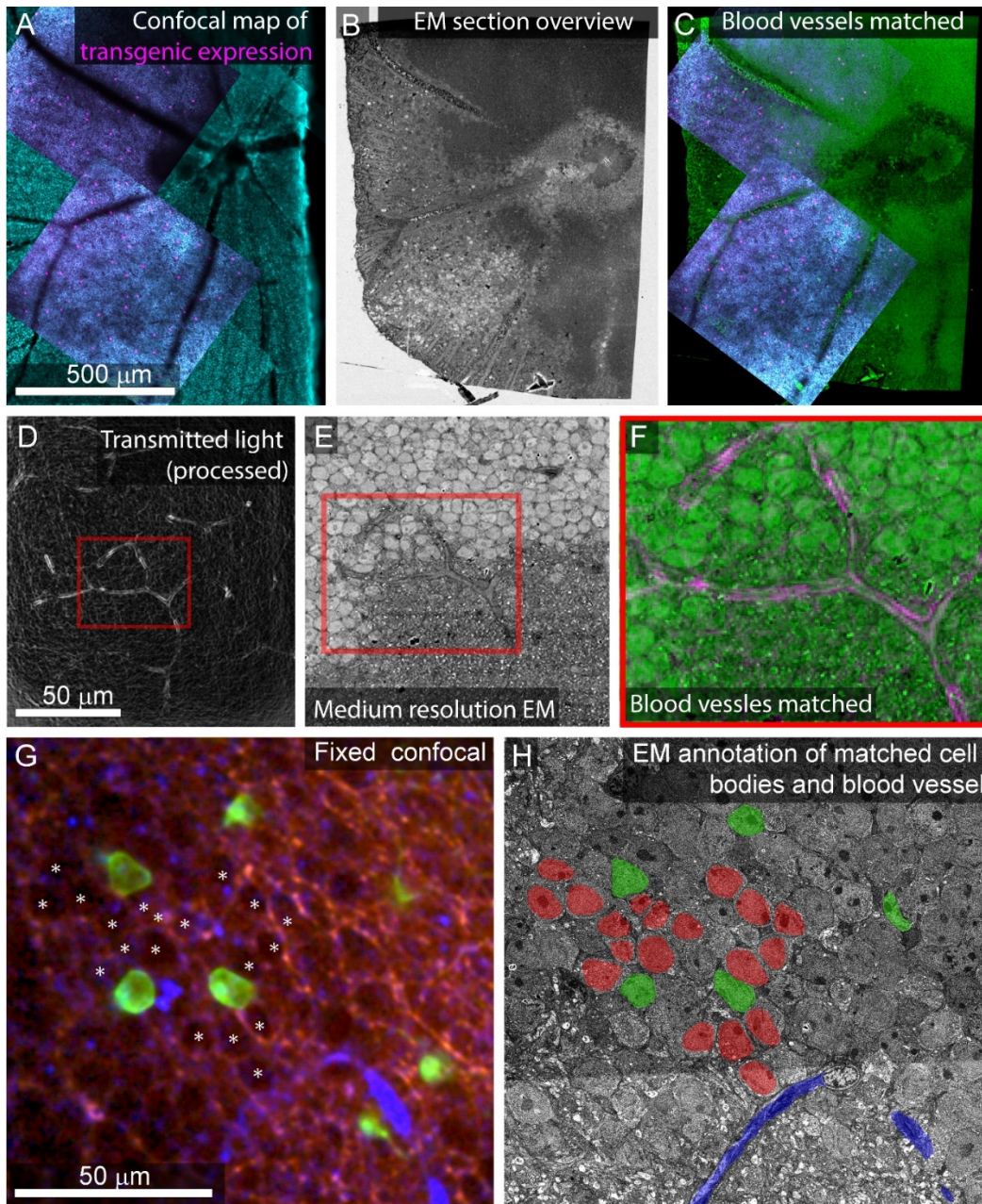
Figure 2.7. Feature matching between optical images and low-resolution EM. A) Multiscale confocal maps of transgenic expression (magenta) and DAPI (cyan) in fixed tissue. Note blood vessels visible by absence of staining. B) Same tissue as A. Section overview image (1 µm pixel size) of ultrathin section used to map tissue position on collection wafer. C) Alignment of blood vessels between the confocal map from A (blue, red) with the section overview from B (green). D) Transmitted light image of live retina filtered with edge detection to show blood vessels. Red box corresponds to the position of red box in panel E and F. E) Electron micrograph of tissue shown in panel D acquired at 40 nm pixel size. Note the blood vessel in the red box. F). Alignment of the blood vessel shown in red boxes in panel D (magenta) and E (green). G) Confocal stack of fixed tissue showing transgenically targeted cells expressing fluorescent protein (green), positions of surrounding cell nuclei (white asterisk) visible by the absence of autofluorescence (red), and blood vessels visible by reflected light (blue). H) Medium resolution (40 nm pixel size) EM section in which the blood vessel (blue), transgenically targeted cells (green), and surrounding nuclei (red) have been matched to the confocal stack in G. Friedrichsen et al., 2022.

To reduce noise in many of our electron micrographs, we median filter the images using a 3 x 2 kernel. We use a kernel that is smaller in the X dimension, because there can already be some signal spread along the X dimension when scan speed nears the frequency response limit of the detection system (~10 MHz). We then normalized the brightness and contrast of each image section to match the mean and range of intensities between images. Image stacks are registered using TrakEM2 within FIJI (ImageJ) using a SIFT-based rigid registration, followed by affine registration, manual landmark-based correction, and finally elastic registration (ScalableMinds, (Saalfeld et al., 2012)). Cells are then annotated by manual tracing using VAST (available at https://lichtman.rc.fas.harvard.edu/vast/, (Berger et al., 2018)).

Alignment of neurites between light and EM

For tissue where fine-scale features (such as neurites) are connected to cell bodies within the high-resolution EM volume, the initial link between cell body identification and matching of smaller features is straightforward. In the example retina dataset, neurites are reconstructed by tracing the primary neurites from the cell body located in medium resolution EM volumes into high-resolution EM volumes (Figure 2.8A). Cell matching and tracing accuracy is confirmed by superimposing 3D renderings of optical images and EM segmentations using Amira (ThermoFisher Scientific) (Figure 2.8B).

Once the target cells are reconstructed, the ease of matching subcellular features within an arbor depends on the structural details of the neurons and the quality and sparseness of the optical maps. For the live retinal imaging example, optical labeling of the neuropil was too dense for most neurites to be matched using a manual side-by-side comparison of the light and EM images. To align optical data and EM segmentations at the micrometer scale, we use matched

fiducial points from cell nuclei and large neurites to calculate an affine transformation of the optical data into the EM volume space (ImageJ). The matching is further refined using a thin plate spline transform with additional fiducial points. We then can view the optical images superimposed on the raw EM data and EM segmentations in VAST (Figure 2.8C) where we can identify additional fine correspondence between optical images and traced neurites. By iteratively adding more tracing, more correspondence points, and re-transforming the optical data, we generate a dense mapping of correspondence between the optical and EM images (Figure 2.8D,E).

The fine-scale projection of the optical data into the EM volume also allows us to identify optically characterized neurites that were not previously traced in the EM volume. Within a plexus of labeled neurites (Figure 2.1A,B), we could iteratively 1) identify a correlated neurite, 2) determine where the next closest optically imaged neurite should be, and 3) perform dense neurite segmentation in the projected region to find the neurite with morphology matching the optical image. Leapfrogging through the optically imaged plexus is significantly more difficult than matching neurites from labeled cell bodies. The general approach to matching light and EM neurites is described in detail by Drawitsch and colleagues (Drawitsch et al., 2018), and the efficiency of the approach is aided by starting with a saturated segmentation of all neurites in the region of interest.
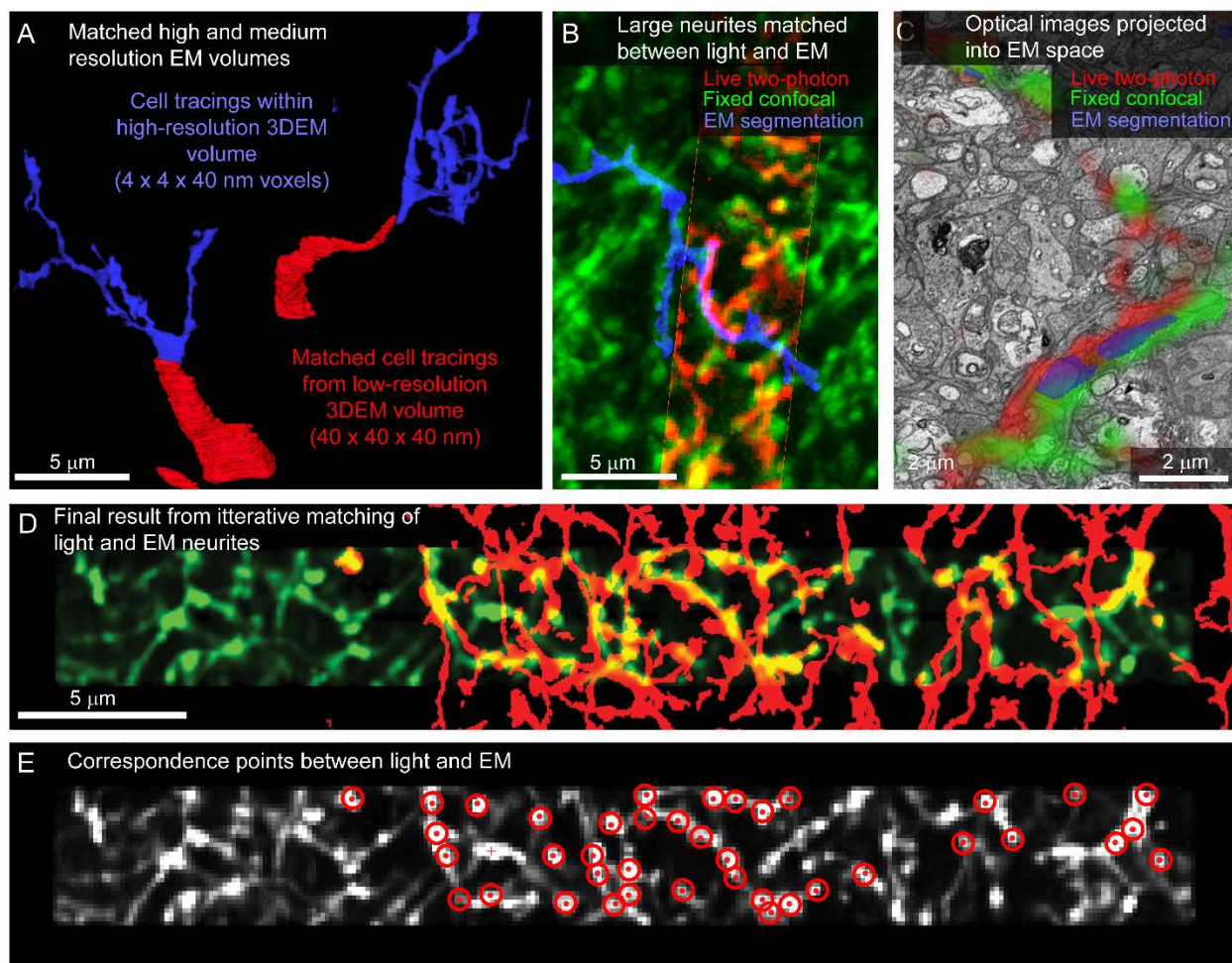
Figure 2.8. Matching neurites between optical images and EM. A) The proximal neurites (red) of cell bodies identified in a large field, medium resolution image volume (40 x 40 x 40 nm voxel size, Figure 2.5H) are traced into the high-resolution image volume (blue, 4 x 4 x 40 nm voxel size). B) Matching the morphology of EM reconstructed neurites (blue) to images from fixed (green) and live (red) optical imaging confirms the initial matching of cell bodies. C) Single slice from EM volume (viewed in VAST) where live two-photon (red) and fixed confocal (green) fluorescence images of the neurons of interest are aligned with the EM volume to determine neurite-to-neurite matches with EM traced (blue) neurons. D) Optical image (red) affine transformed to better fit the EM traced neurites (blue). E) Correspondence points (red targets) where positions in the optical image (grey) have been mapped onto positions of EM traced neurites. From Friedrichsen et al., 2022.

For tissue where the cell bodies of the neurites of interest are not included in the sectioned volume, it is possible to match features between scales using other dense correlation features. For example, to identify contralaterally projecting retinal ganglion cell boutons in the lateral geniculate nucleus, reflected light imaging of fiber tracts (low and medium-resolution

43

features), DAPI staining (medium and high-resolution markers), and fluorescently tagged

Cholera Toxin B (CtB) labeling of the axons of interest was sufficient (Figure 2.9). This

application benefits from the distinctive ultrastructural profile of retinal ganglion cell boutons.
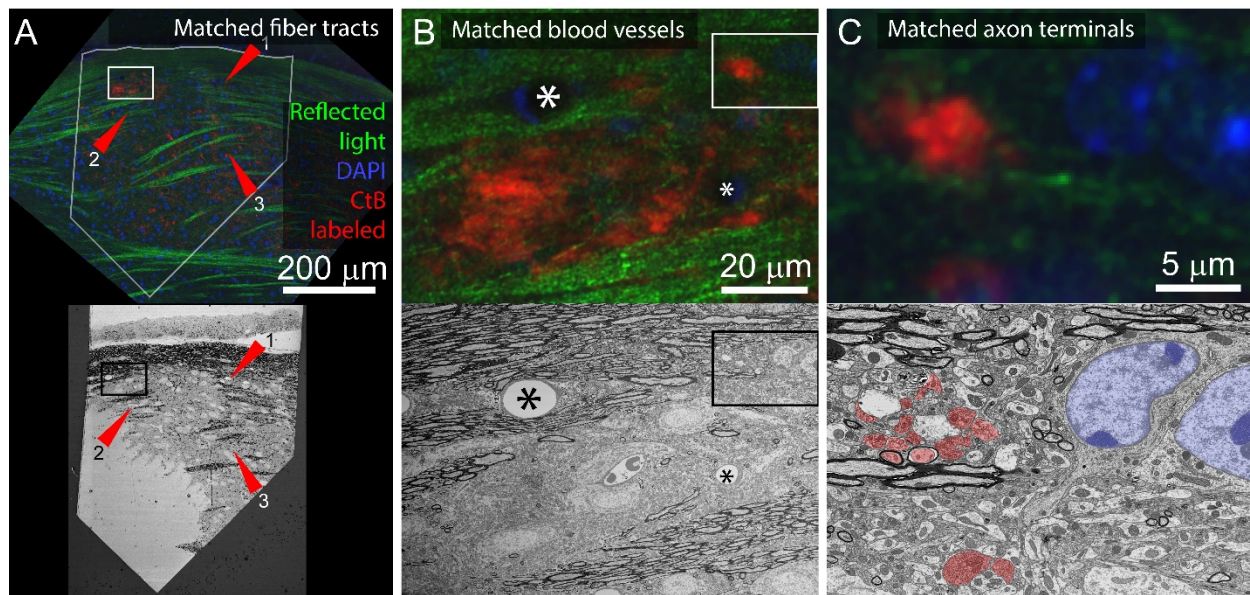
Figure 2.9. Application of multiresolution feature matching in a brain slice. A) The initial alignment of light and EM uses myelinated fiber tracts. Top panel shows confocal image of aldehyde fixed dLGN coronal slice. Red arrows indicate three myelinated tracts that are visible in both reflected light and EM. Green = reflected light, Blue = Nissel stain, Red = axon terminals of CtB injected retinal ganglion cells. Bottom panel shows EM image of the surface of the same brain slice. The white outline in the optical image indicates the position of the EM section. Rectangles indicate the position of images in panel B. B) Secondary alignment uses blood vessels. Top and bottom panels are higher resolution image acquisitions from positions shown in panel A. Corresponding blood vessels are indicated by asterisks. Rectangles indicate the position of panel C. C) Cropped images from B showing correspondences of synaptic bouton and chromatin signals. In the EM image, retinal ganglion cell boutons (ultrastructurally identified by light mitochondria) are highlighted in red and match with the CtB labeled boutons in the optical image. The nucleus and chromatin pattern in EM are highlighted in blue and corresponds to the DAPI labeling in the optical image. From Friedrichsen et al., 2022.

2.4 Results

Using the mrCLEM approach described above, it is possible to selectively image and reconstruct the

synaptic connectivity of optically characterized neurons and neurites (Figure 2.10A-C). The time devoted

to correlating light and EM using this approach is small relative to the time required to reconstruct circuits with EM. Acquiring the confocal images required to map a fixed piece of tissue can be completed in less than 12 hours (Table 1). Acquisition of the low- and medium-resolution EM images to be matched to the confocal maps requires one week (hundreds of sections) to several weeks (tens of thousands of sections).
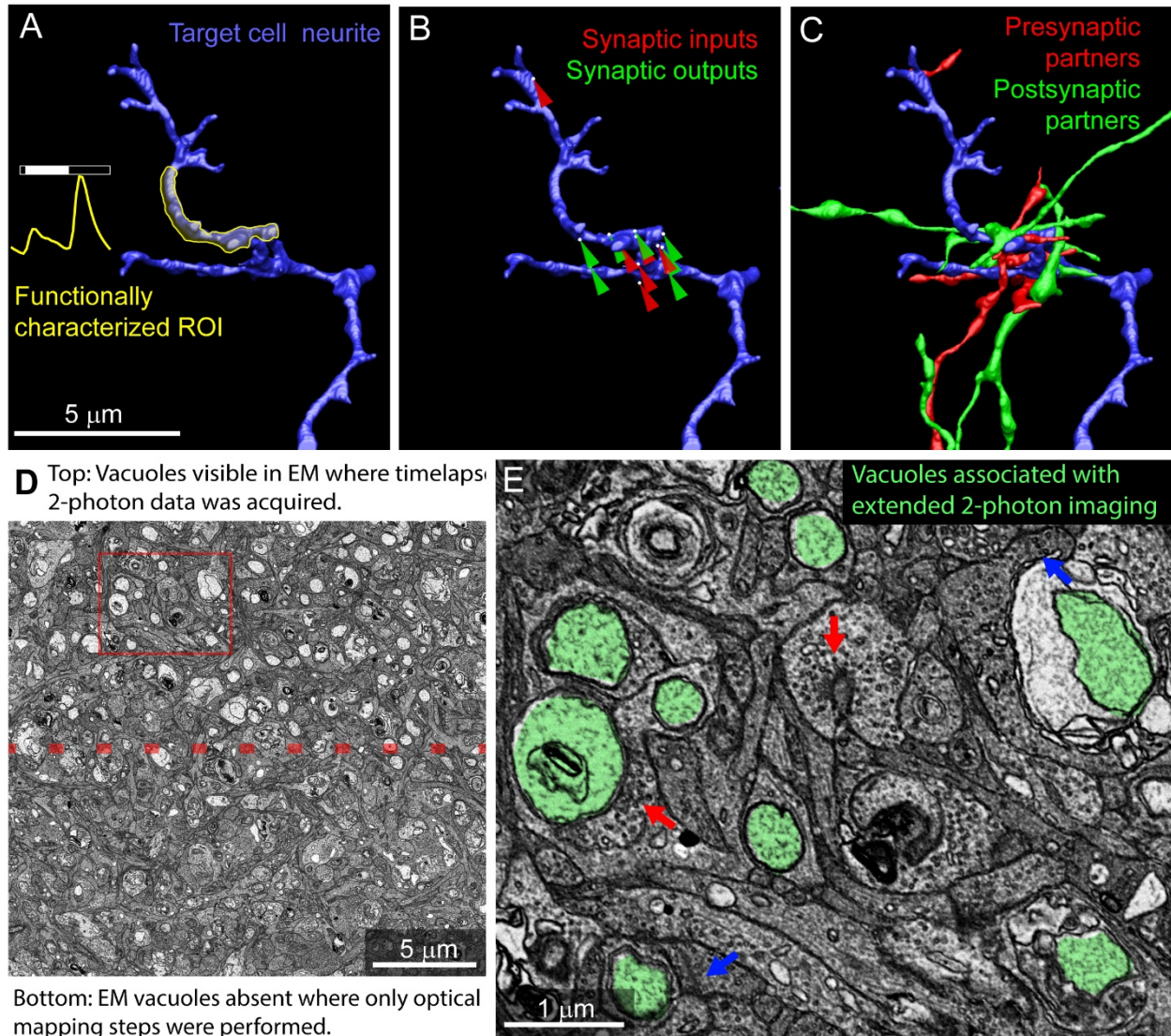
Figure 2.10. Example results from multiresolution matching of functional imaging and EM. A) Local neurite responses (yellow) are mapped onto EM reconstructions of targeted neurons (blue). Same neurite as in Fig 2.8B. B) Synaptic inputs (red) and outputs (green) are mapped on the neurite of interest. C) Pre (red) and postsynaptic (green) cells synaptically connected to the neurite of interest are reconstructed. D) Vacuoles appear in regions of EM tissue that have been imaged continuously with two-photon calcium imaging (top) but are uncommon in the surrounding, optically mapped tissue (bottom). The red box indicates the region shown in panel E. E) Ribbon synapses (blue arrows) and conventional synapses (red arrows) are still identifiable in the two-photon damaged tissue. Vacuoles are highlighted in green. From Friedrichsen et al., 2022.

45

Manually matching of features linking the confocal and EM images may take several days. By contrast, the high-resolution imaging of multi-terabyte EM datasets can take months and generates a dataset that can be mined for years. Figure 2.10C shows a cutout of a larger reconstruction of the functionally characterized cells in which synaptic inputs and outputs are identified and the synaptic partners of the functionally characterized neurites have been reconstructed.

The accuracy of selective imaging is limited by several processes. First, when wafers are reloaded into the microscope for new imaging sessions, slight differences in wafer position must be compensated for by comparing new images of fiducial points on the wafer to previous images. While this process can produce accurate (within ~10 μm) targeting of previously defined feature positions, there are also many sources of potential error that can result in mistargeting (~100 μm shift). To circumvent these reloading errors, a final round of image-based stage correction compares the current view of the targeted region of interest to the previously imaged and aligned overview images. Given a good alignment of these overview images and clear low-resolution features (such as cell bodies) this second targeting process can produce accurate cell-level automated image targeting. The current implementation produces a median section to section displacement of 1.08 μm (100 sections measured, max = 6.22 μm, 95% CI = [0.17 - 2.74 μm]).

Photodamage is a potential consequence of mapping tissue using repeated optical imaging. We have not observed ultrastructural damage associated with Sulforhodamine labeling, DAPI labeling, confocal mapping of fixed tissue, or two-photon structural mapping of live tissue. We have, however, observed ultrastructural signs of damage in regions of tissue where live calcium imaging was used to characterize neurite responses. In regions of the tissue subjected to two-photon imaging for extended periods of time, large pale vacuoles are common in the cytosol (Figure 2.10D,E). Most of these vacuoles are well contained within the cytosol of the cells and do not disrupt tracing. Some vacuoles are large enough to exclude surrounding cytosol, thereby increasing tracing ambiguity. Synapses within the heavily imaged region appeared ultrastructurally normal (Figure 2.10E). We conclude that, while photodamage

46

must be monitored in mrCLEM experiments, optical mapping steps can be performed at exposure levels conducive to circuit reconstruction.

2.5 Discussion

The multiresolution CLEM (mrCLEM) approach we describe here provides a practical and relatively low-cost path forward for combining connectomic, functional, and molecular data. Multiresolution approaches to CLEM can be executed using a variety of technologies. Here, we highlighted the advantages of our ATUM/SEM approach: 1) Sections mounted on ATUM collection tape can be imaged repeatedly without distortion. 2) Modern SEMs can readily switch between millimeter-scale fields of view and nanometer-resolution imaging and therefore are well adapted to automatically mapping and imaging large numbers of sections. 3) The easy generation of micrometer resolution 3DEM volumes makes mrCLEM through pattern matching relatively easy, thereby permitting optimal EM staining. 4) Optical imaging of dense features such as autofluorescence, reflected light, organelle stains, and non-specific stains provides excellent features for matching to medium-resolution EM maps.

   The imaging parameters provided here are meant to communicate the range of scales and modalities that can be linked together in the examination of a single piece of tissue. The specific parameters will vary from experiment to experiment. The most important factor to consider when replicating this multiresolution CLEM pipeline is the ease with which EM images can be acquired from the same tissue at multiple resolutions. Ideally, the electron microscope used should support being able to quickly acquire overview images that are several millimeters wide in which cell bodies can be resolved. The second critical issue is identifying the high-resolution

features that can be both labeled at a useful frequency (not too sparse or dense) in optical images and that can be efficiently annotated in the EM images.

In general, the mrCLEM approach presented here applies to a wide range of tissues because it depends on generic tissue features and labeling. Our example of retinal explants comes with both advantages and disadvantages. The flatness of the retina meant that all cells of interest were readily accessible with confocal microscopy. Performing CLEM on flat tissue also helped to ensure that the light and EM sectioning planes were parallel, thereby eliminating two degrees of freedom from the matching process. Both advantages can also be obtained in brain slices (< 1 mm thick), although tissue clearing and/or two-photon imaging might be required for thicker slices. The most crucial advantage of performing CLEM on retinal tissue was the proximity of the neurites of interest to their cell bodies. This proximity allows for easy linking between medium- and high-resolution matching features. At the same time, the uniformity of cells and neurites within retinal layers and the lack of myelinated axons make pattern matching in the retina more difficult than pattern matching in slices of the lateral geniculate nucleus.

If neurites of interest are connected (within a hundred micrometers or so) to large neurites or cell bodies that can be traced at lower resolution, the multiresolution CLEM approach is efficient. The most significant limit of the mrCLEM approach occurs when thin neurites of interest are not connected to any nearby large neurites (visible in medium resolution EM), myelin, the cell body, or other larger structure. This case requires crawling through dense labeling of optical features from one correlated feature to the next projected correlation. If hundreds of fine neurites need to be reconstructed by this leapfrogging, the efficiency of mrCLEM targeted reconstruction relative to dense reconstruction of all structures is reduced. In cases where easy linking between medium and high-resolution volumes is not available, and

dense reconstruction of large volumes is not required, CLEM through label matching such as NIRB or peroxidase labeling is likely to be a more efficient solution.

Advances in the speed with which serial section EM volumes can be acquired and analyzed have the potential to make major contributions to neuroscience. One application of these advances is the acquisition of petabyte-scale datasets that provide complete descriptions of the organization of important circuits. A parallel path for developing high-throughput volume EM is for terabyte-scale EM volumes to become integrated with the rest of neuroscientific data collection. For this path to be successful, 3DEM connectomic data will regularly be paired with other data modalities, and multiple EM volumes will be acquired for each experimental condition. Multiresolution CLEM, by merging data modalities and targeting connectomic reconstructions to cells and neurites of interest, can accelerate this process.

ACKNOWLEDGMENTS

AUTHOR CONTRIBUTIONS

JLM, DK, KF, and PR contributed to the conception and design of the study. JH performed live imaging. KF performed optical mapping and EM imaging of functionally imaged tissue. PR obtained optical maps with fluorescent dyes. KV prepared tissue for EM. All authors contributed to manuscript revision, read, and approved the submitted version.

Chapter 3

Subcellular pathways through VG3 amacrine cells provide regionally tuned object-motion-selective signals in mouse retina.

3.1 Introduction

In a simplified neuron model, inputs are summed together in a dendritic arbor and, if the sum passes a threshold, an action potential drives synaptic vesicle release to all postsynaptic targets. However, we know that the spatial distribution of input synapses can influence dendritic computations in complicated ways (Bicknell & Häusser, 2021; Borst & Egelhaaf, 1994; Koch et al., 1983). We also know that that there can be diversity and modulation of release probabilities within a single axonal arbor (Piccolino et al., 1984). Realistic modeling of neurons and their connectivity thus requires understanding how the spatial distribution of synapses relates to the subcellular integration and transmission of signals. Neurons with intermixed input and output synapses provide an extreme test case for this sort of analysis.

VG3 amacrine cells, like most other retinal amacrine cells, lack an axon and instead form input and output synapses on the same neurites. Unlike other amacrine cells, VG3s release both

glutamate and glycine (Gong et al., 2006; Haverkamp & Wässle, 2004; Stella et al., 2008). Their best understood function is to transform the motion sensitive light responses of transient bipolar cells into a small-object-motion selective signal that is then transmitted to RGCs and other amacrine cells. VG3s perform this function by integrating excitatory input from ON and OFF transient bipolar cells with inhibitory input from global-motion selective amacrine cells (T. Kim et al., 2015; Lee et al., 2014; Tien et al., 2016). They then drive small object motion responses in multiple ON, OFF, and ON/OFF RGC types (glutamatergic output) and suppress activity (glycinergic output) in suppressed by contrast RGCs and amacrine cells (Jia et al., 2020; Tien et al., 2016). VG3s are especially responsive to looming stimuli, small dark objects increasing in size, and are required for the stereotyped looming-fear response observed across multiple species of mammals (T. Kim et al., 2015).

Though VG3s are small field (~100 µm) amacrine cells, different parts of their arbors exhibit distinct light responses. Neurites differ in their polarity (ON vs OFF), receptive field size, and looming sensitivity depending on their depth within the ON and OFF sublamina of the inner plexiform layer (IPL) (Hsiang et al., 2017). Different areas of a single VG3 can also represent different positions in visual space, and thus the VG3 plexus has a resolution that is effectively smaller than the tiling of VG3 neurons (Chen et al., 2017).

The mixing of input and output synapses, compartmentalization of signal spread, and diverse input and output types all argue that VG3 signal processing should be understood as a system of subcellular pathways. Understanding these pathways requires tools that can characterize structure/function relationships with subcellular spatial resolution. Previous studies of amacrine cell signal integration have used subcellular calcium imaging to understand the extent of signal spread in amacrine cell arbors (Davenport et al., 2006; Denk & Detwiler, 1999;

Euler et al., 2002; Habermann et al., 2003). Serial section electron microscopy has been used to map the fine-scale distribution of synaptic connections across amacrine cell arbors (Famiglietti, 1991; Famiglietti & Kolb, 1975; Joesch et al., 2016; Strettoi et al., 1992; Yamada et al., 2003). Here we combine these two techniques in the same tissue. We first characterize the polarity of the ON/OFF light response in the neurites of a mouse VG3 plexus with calcium imaging. We then use 3D electron microscopy (3DEM) to reconstruct the synaptic connectivity of the same functionally characterized VG3 plexus. By combining these modalities, we generated a subcellular wiring diagram of signal flow through a plexus of neurites with mixed input/output neurites.

We found synapses between VG3s and most bipolar cell and RGC types that stratify in the middle of the IPL. However, VG3s exhibited a strong preference for type 3a bipolar cells and a subset of RGC subtypes. By comparing physiological recordings with our reconstruction of the VG3 plexus, we calculated a length constant for calcium spread and then used that length constant to approximate the VG3-mediated influence of different bipolar cell types on different RGC subtypes. This model predicts that all RGC target types should receive a mix of ON and OFF bipolar cell influence, but that this mix will be tuned towards the response properties of the RGC subtype. This tuning can be explained by the relative stratification depths of the synaptic partners of VG3s and does not require additional synapse specificity rules. We also found that the RGCs innervated by VG3s received excitatory drive from the same bipolar cells that innervate the VG3 plexus. VG3s therefore generate a plexus of excitatory synapses that overlaps the transient bipolar cell terminals and provides a complementary, surround-suppressed version of the local bipolar cell drive to a subset of RGC subtypes.

53

3.2 Materials and Methods

Functional imaging

We imaged retinal calcium responses using GCamp6f (Ai148 strain, Jax #030328 crossed to Vglut3-IRES2-Cre-D, Jax # 028534). Retinas were prepared for live imaging as described in (Hsiang et al., 2017). Twelve sites (two adjacent locations at six IPL depths, scanning area 100 x 13 µm) were imaged at 9.5 Hz using 930 nm two-photon with a pixel size of 0.39 µm^2 while visual stimuli consisting of light and dark bars at different lateral positions were projected onto the retina. We also collected 3D two-photon image stacks of the area at multiple magnifications and of both fluorescence and transmitted light (100 and 300 µm XY, 0.3 µm Z), which provided the 3D morphology of the VG3 and surrounding vasculature for matching to EM images.

After live imaging, tissue was fixed in 2.5% paraformaldehyde and 1% glutaraldehyde, and we acquired multi-resolution confocal tissue maps for CLEM. The tissue was then stained, embedded, and cut into ~1000 ultrathin 40 nm sections for EM imaging. We located functionally characterized VG3 in low resolution 3DEM by comparison of vasculature patterns with optical maps. We then acquired medium resolution (20 nm XY, 40 nm Z) and high resolution (4 nm XY, 40 nm Z) 3DEM volumes encompassing the functionally characterized VG3 (detailed in (Friedrichsen et al., 2022)). We manually traced and reconstructed VG3 arbors and their synapses. We reconstructed pre- and postsynaptic bipolar and RGC arbors from the point of synaptic contact with VG3. All manual tracing was accomplished using the VAST segmentation tool (Berger et al., 2018). We classified VG3-connected neurons as bipolar, amacrine, or RGC depending on the presence or absence of ribbon synapses, conventional synapses, and other ultrastructural indications. We determined the subtypes of connected bipolar cells and RGCs by

visual comparison to the library of retinal neuron morphologies from the Eyewire project

(http://museum.eyewire.org/) (Bae et al., 2018).

Monte Carlo simulations to test specificity of polarity were performed by redistributing

the synapses of each VG3 across their arbor while maintaining similar IPL depth ($\pm$ 0.5 µm). We

examined how 1000 repeated randomizations changed the predicted polarity of VG3 neurites

where the synapses were redistributed using a 16 µm µm length constant. To quantify specificity,

we measured how much the predicted polarity of synapses shifted towards the mean polarity of

the cell when bipolar input positions were fully randomized.

3.3 Results

We used 2-photon imaging to characterize subcellular light responses within the VG3

neuritic plexus. We recorded calcium responses in two nearby regions (Fig 3.1AB). Each

position was sampled at six IPL depths within the ON and OFF strata of the central IPL.

Response polarity was defined as the ON response minus the OFF response divided by the sum

of the ON and OFF responses (-1 for all OFF; 0 for even mix; 1 for all ON). The precise depth of

these recordings was determined by identifying their positions within the 3DEM volume (Figure

1C). VG3 neurite polarities were consistent with previous studies (Hsiang et al., 2017), with

neurites in the OFF sublamina having predominantly OFF polarity and neurites in the ON

sublamina having a more neutral polarity (Fig 3.1CD).

The arbors of VG3 cells were manually traced (Figure 3.2A, Table 1). During tracing,

1835 synaptic inputs and outputs were identified (Figure 3.2BC, Table 2). All cell

reconstructions are considered partial because tracing was limited by image ambiguities and the

edges of the imaged volume. However, a comparison of the arbor sizes of the most complete

VG3 reconstructions (convex hull area = 3,076, 3,830, 4,324, 4,562 μm^2, Table 1) with the arbor sizes observed in previously published optical images of VG3 cells (4723 ± 120, (n=66) (Keeley et al. 2021), 7662 ± 211 μm^2, (n=39) (Tahnbee Kim, Soto, and Kerschensteiner 2015)) indicates that most of the arbors were reconstructed in some VG3s.

For most of our results, we present averages and standard errors with the N equal to the six most reconstructed VG3s. It is important to be clear that these samples are not independent as they are all taken from the same region of the same mouse retina and are often connected to the same synaptic partners. The standard errors presented, therefore, reflect our confidence in estimating parameters within a limited set of cells. Characterizing variation within retinas and between animals will require imaging of additional samples.
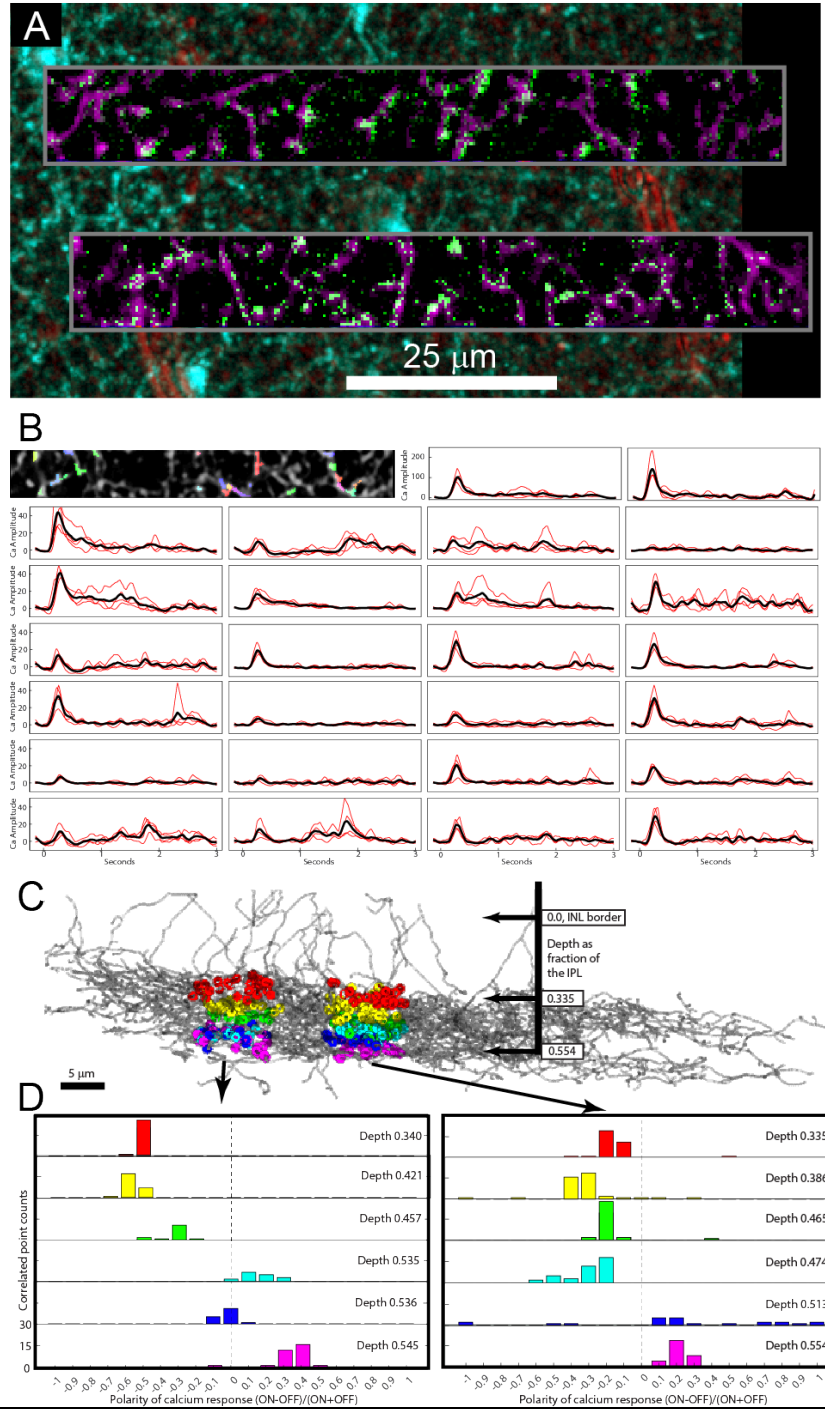
Figure 3.1. Calcium responses of VG3 neurites. A) Two photon imaging of GCamp6f expression in VG3s. Two-photon structural map of VG3 plexus shown in cyan. Transmitted light image of blood vessels in red. Averages of functional images of VG3 neurites shown in magenta. Single frame of calcium response to stimulus shown in green. B) Stimulus evoked changes in GCamp6 fluorescence. Upper left inset shows segmentation of neurites whose responses are shown in red traces. Average of four trials is shown in black. C) Colored dots show functionally characterized neurites that could be mapped onto the 3DEM reconstruction of the VG3 plexus (gray arbors). D) Histograms show ON/OFF polarities of neurites from each functional imaging plane.
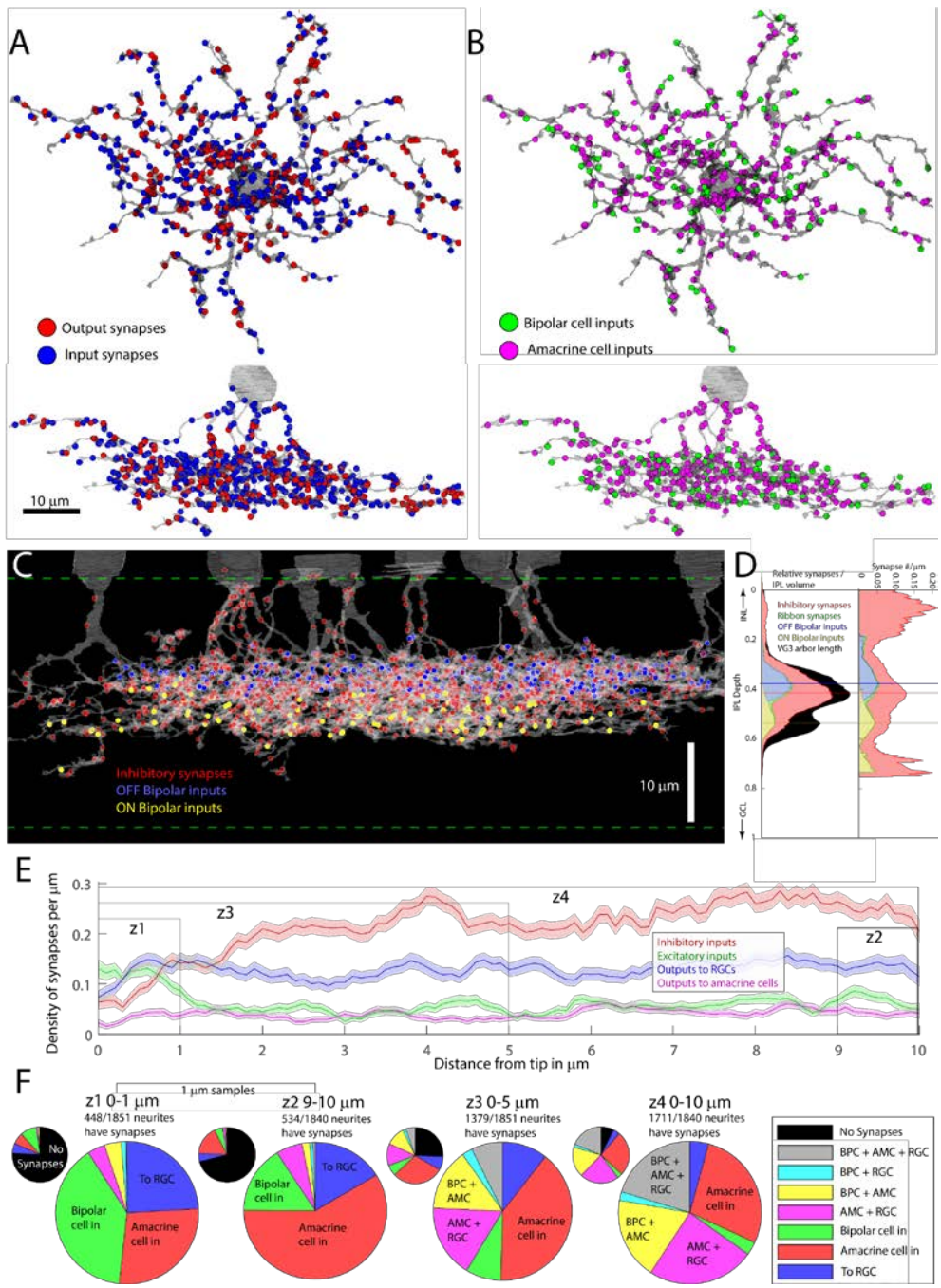
Figure 3.2. The spatial distribution of excitatory and inhibitory synapses on the VG3 arbor. A) Input and output synapses are intermixed on the same arbor branches. B) Excitatory and inhibitory inputs are mixed other than on primary neurites. C) ON and OFF bipolar inputs were concentrated in two strata with a small separation between them. D) Excitatory to inhibitory ratio is smallest in the zone between ON and OFF lamina and on primary neurites. E) Bipolar inputs have highest density at branch tips, followed by RGC outputs, then amacrine inputs. F) Synapse densities differ at neurite tips, but overall synapse densities at tips are too low to form significant numbers of bipolar-VG3-RGC pathways free of amacrine input.

cid	arbor µm	total syn density syn/um (#)	bipolar input syn/um	AMC input syn/um	AMC output syn/um	RGC output syn/um	total input syn/um	total output syn/um
2	1632	0.482 (787)	0.07	0.207	0.092	0.105	0.278	0.197
3	1526	0.37 (564)	0.074	0.155	0.064	0.065	0.229	0.129
4	1350	0.359 (485)	0.059	0.137	0.098	0.056	0.196	0.153
5	807	0.304 (245)	0.036	0.13	0.077	0.051	0.166	0.128
13	1223	0.474 (580)	0.061	0.213	0.119	0.07	0.273	0.189
14	918	0.37 (340)	0.07	0.17	0.076	0.05	0.24	0.126
All	1243	0.393 (500)	**0.062**	**0.169**	**0.088**	**0.066**	0.230	0.154
SE	134	0.029 (78.3)	0.006	0.014	0.008	0.008	0.018	0.013

Table 3.1. Arbor sizes and densities of different synaptic inputs and outputs from reconstructions of six VG3.

The reconstructed VG3 plexus spanned from 16% to 60% of IPL depth (95% length contained), consistent with the IPL depths where axon terminals of the ON and OFF transient bipolar cells stratify.

One amacrine cell (cid 5, table 3.1), identified as a VG3-AC in optical imaging by its expression of the Cre-driven calcium reporter, had arbor morphology significantly different from other VG3-AC. Many of its neurites branched relatively little, forming a sparse arbor with incomplete coverage of its dendritic field. However, despite different morphology, local branch synaptic connectivity patterns closely matched those of other VG3s. Because inputs and outputs are mixed in VG3s, it is possible that the local processing executed in this unusual arbor are not functionally distinct from that executed by differently shaped VG3s in the same plexus.

We identified 1777 input synapses across six VG3 cells (Table 3.2). Of these synapses, 26.1 ±1.9% (SE for n = 6 cells in one piece of tissue) were ribbon synapses from bipolar cells and 73.9% ±1.9% were conventional synapses from amacrine cells, giving an excitation to inhibition (E/I) balance of 0.35± 0.035.

The relative spatial distributions of excitatory and inhibitory synapses may impact signal integration in VG3s. Bipolar inputs were concentrated in two strata corresponding to the centers of the transient OFF bipolar cell axon terminals and the transient ON-bipolar cell terminals (Fig

3.2AB). In contrast, the density of amacrine cell inputs peaked between the ON and OFF bipolar cell input zones, as well as on the primary neurites of VG3s. The distribution of inhibitory inputs appears well-positioned to dynamically regulate signal spread between the ON and OFF neurites of VG3s and between different primary neurites on the same VG3. Further, the lower density of bipolar cell inputs on these potential crossover regions could contribute to the segregation of ON and OFF signals in the VG3 arbor.

During arbor tracing, we noted that neurite tips often received ribbon inputs. Analysis shows an increase in the density of bipolar cell inputs near the tips of neurites (Fig 3.2EF). Conversely, the RGC output and amacrine cell input density are below average at the tips of neurites. The high density of bipolar cell inputs and lower density of amacrine cell inputs at the ends of VG3 neurites suggested there might be amacrine-free paths from bipolar cells to RGCs at the scale of several micrometers. To test for these paths, we checked for different combinations of bipolar cell inputs, amacrine cell inputs, and output synapses to RGCs at the tips of neurites. We found that the density of synapses is too low for the variations in synapse density occurring at the last micrometer of VG3 neurite to impact microcircuitry (Figure 3.2F). When examining the last micron of neurite tips, only 28.9% of 2128 neurite tips had any synapses and only 0.61% had bipolar cell inputs, RGC outputs, and no amacrine cell inputs. Examining longer lengths of neurite (5, 10 µm) revealed more combinations of multiple synapse types, but tips which included bipolar inputs and RGC outputs with no nearby amacrine inputs were rare (Figure 3.2F). We were, therefore, unable to identify a clear impact of the divergence of synapse densities at VG3 neurite tips on the functional organization of local microcircuitry.

We were able to identify the subtype of 101 bipolar cells forming 428 of the 477 (89.7%) ribbon synapses onto VG3s. Classification criteria included morphology, stratification depth,

branch angle, and branch depth. Most bipolar cell types can be recognized solely by axon terminal stratification depth (Figure 3.3A). However, distinctions within the transient OFF group (3a, 3b, 4) and type 5 ON bipolar cell group (5t 5i 5o) were more difficult. For these distinctions we used a combination of arbor morphology and mosaics to assign subtypes (Figure 3.3B). Bipolar cells of the same subtype generally avoid homotypic overlap (Wässle et al., 2009). Often this tiling rule was expressed as branches terminating where they contacted another cell of the same subtype (Figure 3.3C).

Ribbon synapses onto the reconstructed VG3s were formed by bipolar cells of subtypes 3a (52.3±1.6%), 3b (8.1±1.8%), 4 (9.9±2.4%), 5o (15.8±1.8%), 5i (6.1±2.5%), 5t (3.5±1.4%), xbc (3.1±0.9%), and 6 (1.0±0.6%) (Fig 3.3D). OFF transient bipolar cells contributed 65.3% (±2.1%) of ribbon inputs while ON bipolar cells contributed 34.7% (±2.1%). This cohort of subtypes comprises all bipolar types with axonal arbors stratify at the same depth as the VG3 plexus. Other than rare synapses with type 6, we found no synapses with bipolar cells that stratify outside the main VG3 plexus (type 1, type 2, type 7, or type 8/9 bipolar cells).

These results might appear to argue for indiscriminate synapse formation between bipolar cell axon terminals and the neurites of the VG3 plexus. However, the strong bias towards type 3a bipolar input argues for a degree of synaptic preference. To quantify this apparent preference, we performed a Monte Carlo analysis which generated synapses between VG3s and bipolar cells based on the amount of overlap between VG3 and the library of bipolar cell arbors from Eyewire reconstructions (Figure 3.3E) (Bae et al., 2018).
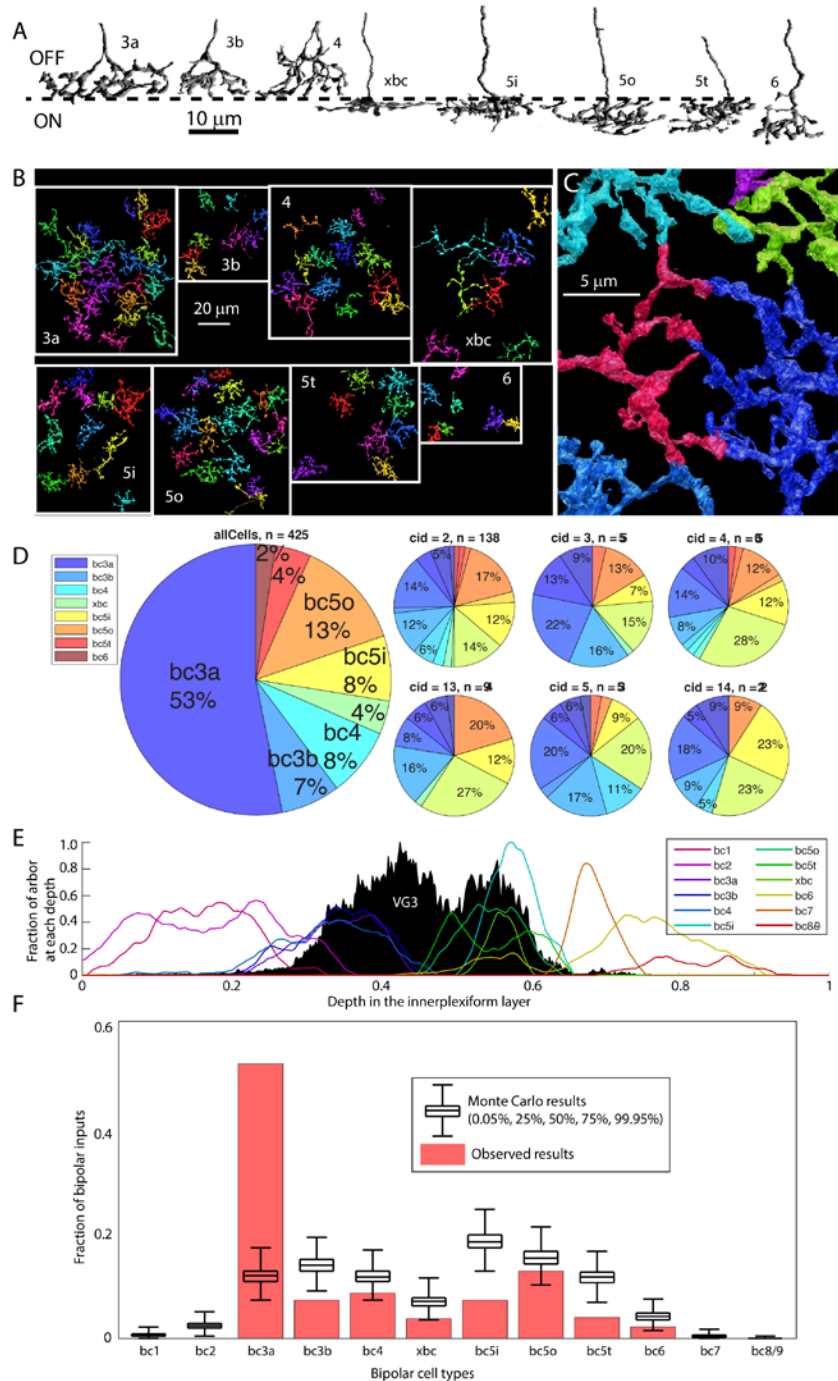
Figure 3.3. Patterns, relative proportions, and specificity of ribbon inputs from bipolar cells. A) Morphology and axon terminal depth of bipolar types innervating VG3 plexus. B) Mosaics of different bipolar subtypes. C) When axon terminal branches stop when they meet another bipolar axon terminal branch of the same subtype. D) Overall proportions of bipolar input from each subtype, with subgraphs for individual VG3. E) VG3 costratifies with multiple types of bipolar cells. Bipolar arbor depth distributions from Eyewire library. F) Monte Carlo estimating frequency of bipolar type innervation frequency based on arbor overlap showing strong preference for bc3a input and slightly low frequencies for other types of transient bipolar input.

We found that, in 99.9% of the Monte Carlo results, type 3a bipolar cells were responsible for between 7.5% to 17.1% of bipolar cell synapses onto VG3s (Figure 3.3F). In our reconstructions, type 3a bipolar cells contribute 53.2% of the bipolar inputs, more than three times what might be expected by chance. VG3 preference for type 3a bipolar cells is reflected both by the number of 3a bipolar cells innervating the VG3 plexus (23 cells) and by the number of synapses per bipolar cell (10.7 ± 1.4 synapses per 3a bipolar cell) (Table 3). The next most common input type, 5o, formed less than half as many synapses per bipolar cell (3.7 ± 0.6 synapses/cell (n=19)).

Type 5 bipolar cells include subtypes that differ in the speed of their responses (Hellmer et al., 2016; Ichinose et al., 2014). The motion sensitivity of VG3 amacrine cells suggests that they would primarily be innervated by bipolar cells with fast transient responses to light. However, by our classification, we found that both the fast transient and slower type 5 bipolar cells innervate VG3s. Distinguishing between bipolar type 5i, 5o, and 5t cells anatomically is difficult, and it is possible that there are errors in our classification. However, we observe multiple type 5 bipolar cells presynaptic to VG3s in the same territory (Figure 3.3B). Given the homotypic repulsion of bipolar cells, this observation indicates three separate mosaics of type 5 bipolar cells innervate VG3s. Regardless of the possibility of classification errors, the dense overlap strongly suggests that VG3s receive synapses from each of the subtypes.

bipolar cell type	number of bipolar cells	total number of synapses to VG3s	mean number of synapses (SEM)	Synapses per pairing (SEM)
bc3a	**27**	**227**	**8.41 (1.291)**	**3.97 (0.324)**
bc3b	9	30	3.33 (0.957)	1.73 (0.236)
bc4	15	35	2.33 (0.398)	1.87 (0.197)
bc5o	19	57	3.00 (0.535)	1.77 (0.171)
bc5i	12	33	2.75 (0.880)	1.40 (0.202)
bc5t	9	18	2.00 (0.553)	1.62 (0.257)
xbc	8	17	2.12 (0.515)	1.57 (0.266)
bc6	7	10	1.43 (0.297)	1.33 (0.314)

Table 3.2. Frequencies of innervation of VG3 by transient bipolar cell types.

We next determined which retinal neuron types were being innervated by the VG3s. We identified 1279 output synapses in the reconstructed VG3 plexus. We did not find any unambiguous outputs to bipolar cells, nor did we see any VG3-to-VG3 synaptic connections. To distinguish between synapses innervating RGCs and those innervating amacrine cells, the postsynaptic cells were traced until we encountered an output synapse (amacrine cell) or passed several branch points with no synaptic outputs. The majority of VG3 output synapses targeted other amacrine cells (n=714 (55.8%)). In total we identified 544 (42.5%) probable VG3 to RGC synapses.

Due to the wider dendritic fields of some target RGC types, tracing of dendrites frequently reached the edges of our high-resolution 3DEM volume. When possible, we continued tracing dendrites in our surrounding medium-resolution volume (20nm XY, ~600μm x 600μm x 36μm), aided by the fact that RGC neurites tend to become larger closer to the cell body. As with our bipolar reconstructions, we determined RGC type based off morphological characteristics and stratification depth.

We were able to identify the subtypes of 47 retinal ganglion cells innervated by 378 synapses from the VG3 plexus (Figure 3.4A). These retinal ganglion cells included 19 subtypes, with two-thirds of the subtypes being represented by only one or two examples (Table 3). Three synapses innervated an RGC with stratification consistent with an M3 RGC, but whose reconstruction is too fragmentary to identify confidently. Because of the limited sampling of the large number of total RGC subtypes (47), it is not possible to rule out any potential VG3-RGC combination using this dataset.

Much of the VG3 to RGC innervation targeted RGCs with small to medium ON, OFF, and ON-OFF receptive fields that are sensitive to moving stimuli. These included 5ti RGCs (W3, UHD, small-field transient ON-OFF, 19.8%, ±2.27%), type 63 RGCs (F-mini-ON, 11.6%, ±1.61%), and type 37 RGCs (ON-OFF direction-selective, 12.6%, ±1.74%). Almost a third of these synapses went to three types of monostratified transient OFF RGCs that stratify at the same depth within the IPL: 4i RGCs (7.7%, ±1.04%), 4on RGCs (6%, ±1.35%), and 4ow RGCs (transient OFF alpha RGC, 15.7%, ±1.77%). The prevalence of VG3 synapses to the 5ti (W3) and 4ow (t-OFF-α) RGCs makes sense given that physiological, genetic knockout, and behavioral evidence (T. Kim et al., 2020; Lees et al., 2020; Wang et al., 2021; Yilmaz & Meister, 2013) argue that the VG3 innervation of these two types of RGCs is responsible for responses to looming stimuli, a major function of VG3 cells (Chen et al., 2017; Hsiang et al., 2017; T. Kim et al., 2020). VG3s also heavily innervated the type 6sw monostratified transient ON RGCs (medium field transient ON, 13.9%, ±2.65%).

Very few synapses were found innervating RGCs with sustained responses. The type 8w (sustained ON Alpha, 0.2%, ±0.24%) was the only synaptic drive to sustained RGC subtypes we observed. The few synapses formed onto the 8w were formed by one neurite that strayed outside

of the main VG3 plexus and which was also unusual in being predominantly innervated by type 6 bipolar cells.

We were surprised to find little innervation of type 28 or 72, both suppressed-by-contrast (SbC) RGCs with similar morphology. Previous studies found that VG3s synaptically inhibit SbC RGCs and are important for their characteristic reduced firing in response to local visual stimuli (Lee et al., 2016; Tien et al., 2016). We found only one likely SbC RGC receiving only 5 synapses (1%, ±0.44% of total VG3 output to RGCs). The stratification of SbC RGCs (primarily outside of the Chat bands, (Tien et al., 2015)) may provide few opportunities to form synapses relative to other target RGC subtypes. Our reconstruction suggests the either the inhibitory role of VG3s onto RGCs constitutes only a small fraction of VG3 synaptic output, or that VG3s inhibit more subtypes than SbC RGCs.
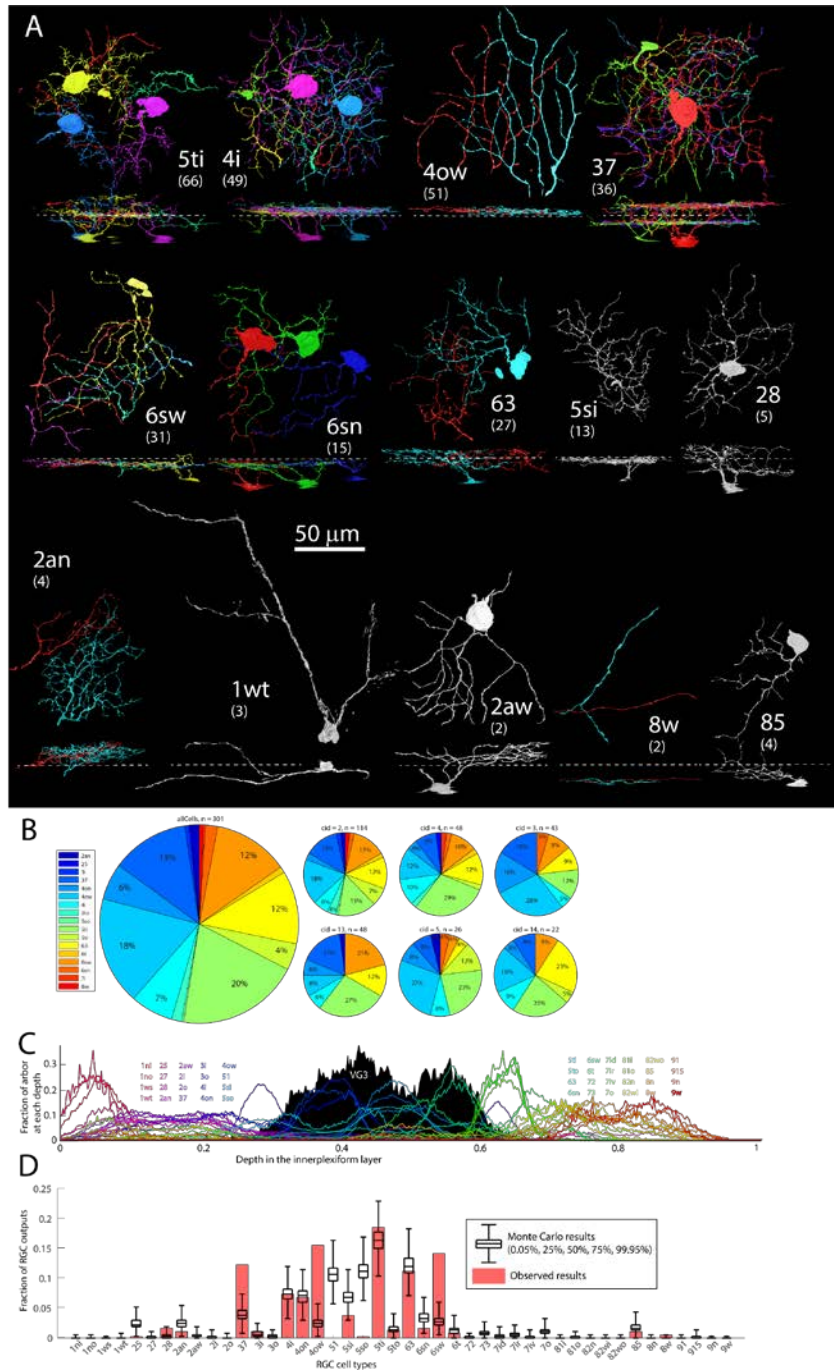
Figure 3.4. VG3 innervates many RGC types. A) Reconstructed RGC arbors of cells receiving VG3 innervation. B) Proportions of RGC types innervated by VG3, with subgraphs for individual VG3s. C) Arbor stratification overlap between VG3 and different RGC subtypes. RGC arbor depth distributions from Eyewire library. D) Monte Carlo estimating frequency of synaptic connections to different RGC types based on arbor overlap. Most connection frequencies are near expected ranges, with exceptions of enriched connection to types 37, 4ow, and 6sw and diminished connection to types 51, 5si, and 5so.

	number of cells	total number of synapses from VG3s	Synapses per pairing (SEM)
25	1	1	1.00 (0.000)
28	1	5	1.67 (0.667)
2an	2	4	1.00 (0.000)
37	9	45	2.05 (0.326)
3i	1	3	1.50 (0.500)
4i	2	25	2.27 (0.359)
4on	3	21	1.91 (0.476)
4ow	3	55	3.67 (1.153)
5si	1	14	3.50 (1.658)
5so	1	1	1.00 (0.000)
5ti	6	66	3.67 (0.667)
5to	1	5	2.50 (1.500)
63	3	41	2.93 (0.633)
6sn	2	6	1.20 (0.200)
6sw	5	53	2.65 (0.437)
6t	1	3	1.50 (0.500)
7i	1	2	1.00 (0.000)
85	1	4	4.00 (0.000)
8w	2	2	1.00 (0.000)
m3	1	3	1.00 (0.000)

Table 3.3. Frequencies of innervation of RGC types by VG3.

Although we did not see as strong of preferences in VG3 to RGC innervation as we saw in bipolar cell to VG3 innervation, five partner types (5ti, 4ow, 37, 63, and 6sw) accounted for 73.6% of VG3 to RGC synapses. To test whether the weighting of VG3 synapses towards a few RGC subtypes represented selective synapse formation or costratification with VG3s, we repeated the stratification-based Monte Carlo simulation for RGC subtypes. Broadly, incidences of synaptic connectivity were consistent with stratification-based predictions of high connectivity for RGCs stratifying between the ChAT bands (30%-70% of IPL depth, Figure 3.4D). Notably, the number of synapses formed with the most frequently connected subtype, 5ti, was well predicted by the high degree of overlap with the VG3 arbors. We found that the number of

synapses innervating three more tightly stratified RGC subtypes, 37 (45), 4ow (57), and 6sw(52) were more common than predicted by the model (99.9% CI = 4-28, 1-21, 2-22, respectively) (Figure 3.4D). However, we found that type 51 and 5so RGCs received far fewer synapses than would be expected from their overlap with VG3s (Figure 3.4D). These results are consistent with stratification playing a dominant role by determining opportunities for connectivity and cell type-specific synapse formation preferences enhancing connectivity with some cell types and suppressing connectivity with others.

An important caveat to this analysis is that the model treats the assignment of subtype to each synapse as an independent probability weighted by stratification. In reality, forming one synapse demands that the neurites are in close enough proximity to form additional synapses. An analysis of synapse clustering shows that RGC synapses are more common within 5 µm of other RGC synapses. We repeated our Monte Carlo analysis after randomly pruning synapses until no synapses between a pair of cells were within 10 µm of one another. This control did little to change the results with the observed number of synapses for 37 (40), 4ow (51), and 6sw (42) still well above the range of expected results (99.9% CI = 3-25, 1-18, 1-20, respectively).

To estimate the relative influence of VG3 versus bipolar cell input to an RGC, we counted bipolar inputs across the available arbors of three RGCs representing the most frequent RGC target types: 5ti, 4ow, and 37 (Supplementary figure XX, see also Figure 9). We found VG3s constituted 38.4% (38 VG3 inputs vs 61 bipolar cell inputs) of excitatory inputs onto 4ow, 27.9% (36 vs 93) onto 5ti, and 22.7% (22 vs 75) onto 37. While VG3 input was roughly on the same order as bipolar cell input, bipolar ribbon inputs outnumbered VG3 input for target RGC types.

While VG3s and their RGC targets sample from overlapping groups of bipolar cells, their samplings of these groups differ. As described above, the ON/OFF polarity of the targeted RGC subtypes can differ from the transient OFF-dominated VG3 plexus. In the case of the 5ti where we identified its bipolar cell inputs, we found that 45 were from transient ON bipolar cells, 11 from sustained OFF bipolar cells, and 31 were from transient OFF bipolar cells. The 38 synapses from the VG3 bipolar cells (mean polarity -0.39) therefore deliver a heavily OFF-biased signal to what would otherwise be a balanced ON/OFF drive.

In sum, while we found synapses between the VG3 plexus and most of the RGC types with significant stratifications in the middle retina, this innervation was heavily weighted towards a few transient OFF and transient ON/OFF RGCs. The output profile of VG3s, therefore, appears to result from a combination of stratification and subtype preference.

To understand how VG3 cells process visual information and transmit it to RGCs, we sought to determine the relative influences of bipolar cell inputs on output synapses to retinal ganglion cells. We created node-edge skeletons (internode length of ~0.1 μm) of traced VG3 arbors to determine the topological (through-the-arbor) distances between each pair of synapses. However, relating inter-synapse distances to relative influence requires a model of how bipolar input signals decay over distance. To robustly estimate a length constant for bipolar cell signal decay within VG3 arbors, we used three approaches comparing maps of VG3 connectivity to calcium imaging of VG3s.

We first estimated the VG3 length constant by comparing the EM reconstructions to previously published measurements of response polarity of the VG3 plexus at different IPL depths (Hsiang et al., 2017). We assigned each ribbon synapse a polarity based on bipolar cell type (ON or OFF). We then tested a range of length constants (1:150 µm) using a simple

electrotonic model. Based on those previous studies, the average polarity is -0.18 at IPL depth

0%, -0.44 at 21%, -0.45 at 29%, -0.32 at 37%, 0.02 at 44%, 0.22 at 51%, and 0.23 at 60%. When

we compared these measures to the predictions of our electrotonic model using the average

difference in polarity as an error metric, we found the best length constant was 19 μm. This

length constant produces polarities of -0.31, -0.31, -0.35, -0.30, -0.22, 0.19, 0.23 at the

corresponding depths (Fig 3.5A). Our anatomical prediction, therefore, roughly recapitulated the

transition from OFF-biased to ON-biased mixed VG3 light responses.

We next compared our anatomical predictions to our functional imaging of the same

neurites. We manually located 334 correlation points between locations in our 3DEM volume

and pixel locations in two-photon calcium imaging. To test the noisiness of our polarity

measures, we compared the functional polarity of correlation points that were anatomically close

enough that we would expect very similar functional responses. We found that the median

difference between ROI polarities less than 3 μm apart was 0.214 (242 correlation points). We

found that one calcium imaging frame was responsible for introducing the majority of errors at

close distances, and so we removed that frame from subsequent analyses (reduced to 202

comparisons with a median polarity difference of 0.156). We also found that we could reduce the

polarity differences of nearby ROIs difference to 0.122 by eliminating ROIs with significant

inter-trial variations in polarity (reduced to 54 correlation points). A polarity difference of about

0.12 can then be considered a ceiling for the accuracy with which we might be expected to match

functional measurements of polarity with anatomical estimates.

We next compared our anatomic model to functional recordings of the same neurons.

After grouping together correlation points less than a micrometer apart and filtering as described

above, we reduced our original 334 points to 124. To allow for technical differences in the extent

of ON/OFF mixing that could be due to noise, we searched for the best fit across a range of "noise" values that were added to both the ON and OFF anatomical predictions. We also tested a range of ON scaling factors (.2-5x) to allow for average differences in the strength of ON and OFF bipolar cell inputs. The length constant that produced the best overall fit for the functional ROIs was 10.2 µm with a mean polarity difference of 0.202 (Figure 3.5A). An error level of 0.22 includes length constants ranging from 4.8 to 22 µm. For comparison, we randomly scrambled the functional polarities among the correlation points and found a best length constant of 71 µm with an average error of 0.258. While the real fitting performed better than random, it did not approach the best possible fit (0.12) and the best length constant differed from that of the length constant based on a comparison to the previously reported polarities (19 µm). A possible source for the range of length constant results in the polarity fitting could be due to noise in our functional measurement of polarity or incorrect assumptions in how ON and OFF bipolar signals mix in VG3s. We, therefore, used a third length constant estimation that was independent of polarity.
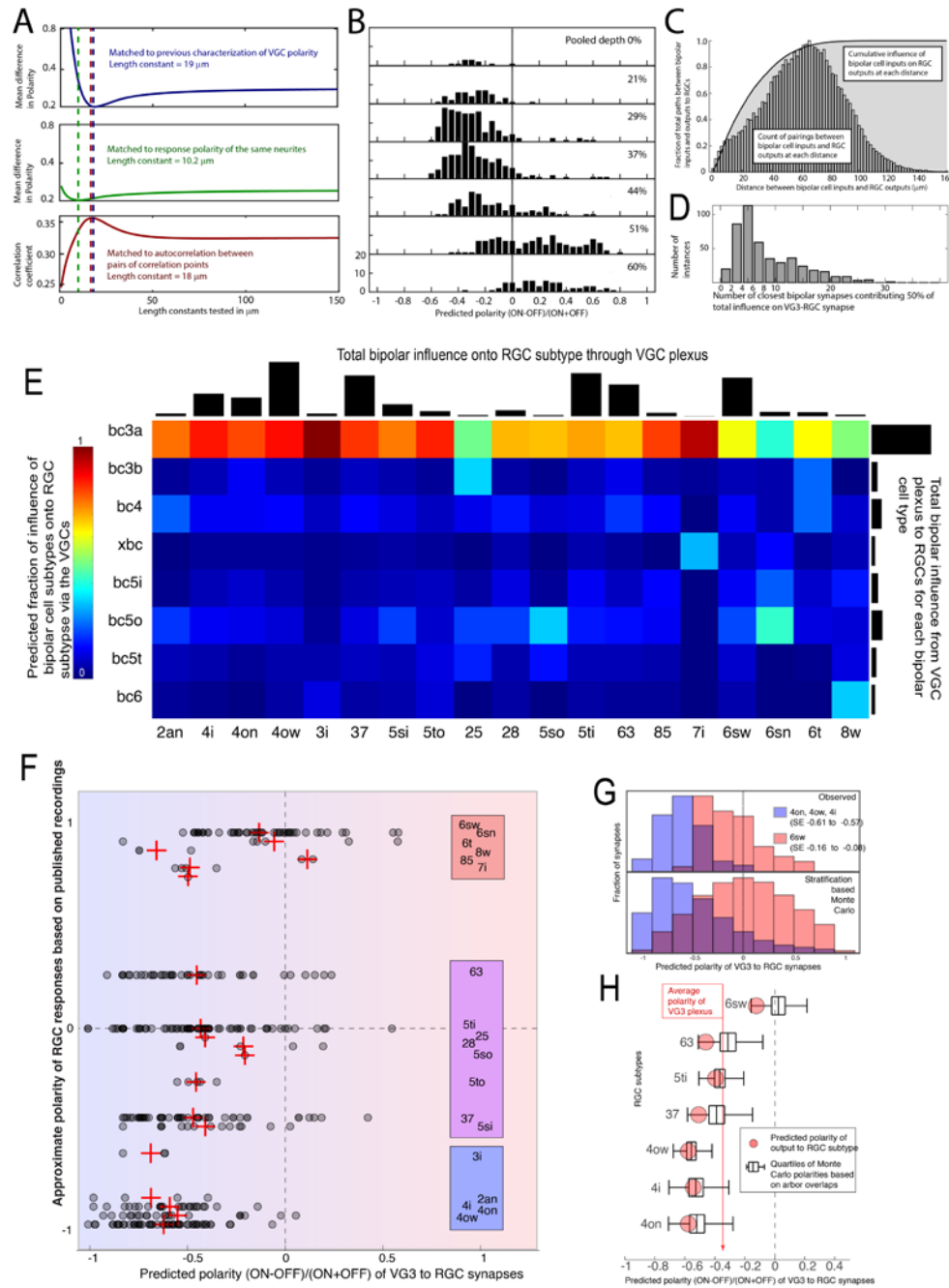
Figure 3.5. The influence of bipolar input polarity on estimated VGC to RGC synapse polarity. A) Estimation of bipolar signal length constant by 3 methods showed general agreement. B) Predicted polarity of CLEM correspondence points using 16 µm length constant. C) Half of total bipolar influence on RGC outputs originated from inputs within 21 µm. D) Most RGC output synapses were primarily influenced by between 2 and 20 bipolar inputs. E) Matrix showing influence of each bipolar type on each RGC subtype via the VG3. Influence from bc3a input predominates. F) Predicted polarity of VGC to RGC synapses ranges from strongly OFF for 4ow RGCs to mixed ON-OFF for 6sw RGCs. G) Monte Carlo simulation rearranging lateral branch positions of synapses reproduces observed polarity predictions. H) Monte Carlo simulation of predicted average polarity of VG3 to RGC synapses by RGC subtype reveals general agreement with slight OFF bias for some RGC types.

We calculated correlation coefficients for pairs of correspondence points using the raw calcium signal (ignoring stimulus timing). This calculation required that correspondence points be present in the same imaging plane and thus were likely to have similar ON/OFF polarities. We next found the correlation coefficients for bipolar cell influence. The correlation was calculated using the vector of the influence of each bipolar cell onto the correspondence points. The bipolar cell influence was predicted from the anatomic electrotonic model testing a range of length constants. We found that the length constant that best matched the functional and anatomical correlation coefficients was 18 µm (Fig 3.5A).

Considering the three models, we settled on a functional length constant of 16 µm (average of 10.2, 18, and 19). The distribution of estimated polarities across IPL depth using this length constant value is shown in Figure 3.5B. Consistent with its origin, this length constant predicts a shift from OFF biased responses to a more even balance, matching the calcium imaging (Figure 3.1D) and previous physiological characterizations of VG3s. Our length constant model does not consider neurite diameter, channel distribution, timing, or many other factors important to dendritic computation. Notably, the model we use here does not explicitly model the influence of inhibitory amacrine cell synapses dividing the ON/OFF sublamina. These amacrine inputs not only change membrane conductance but can shape responses in a feature-selective manner, i.e., alter polarity or correlation coefficients of neurites. However, the simple length constant model does provide a realistic baseline for estimating the functional relationship between bipolar cell inputs and VG3 responses. In particular, the calcium rises that constrain the model are closely tied to the neurotransmitter release that the model attempts to predict.

We used the influence length constant estimated above to determine which bipolar cell subtypes are likely to influence each RGC subtype via our reconstructed VG3s. We first

calculated the distance between every VG3 to RGC synapse and every bipolar cell to VG3 synapse and then calculated an influence value using our length constant of 16 µm. We found that half of the bipolar influence on the VG3-to-RGC synapses originated within 21 µm of the synapse (Figure 3.5C). We then summed these influences across RGC subtypes. Unsurprisingly, type 3a bipolar cells dominated the estimated influence on most RGC subtypes, and deviations from this pattern were only found in RGC types with small samples (Figure 3.5E).

To determine the distribution of ON vs OFF bipolar influence VG3s deliver to the IPL, we pooled the influences of ON bipolar cell types together (3a, 3b, 4) and OFF bipolar cell types together (5i, 5o, 5t, 6). A plot of the total ON and OFF influence (sum of influence from each neurite) provided by VG3s, shows roughly equal amounts of ON drive in the ON and OFF sublamina (Figure 3.5F). However, the OFF drive was asymmetric with a strong influence in the OFF sublamina and a much weaker drive in the ON sublamina. This difference can be explained by the fact that neurites in the ON sublamina are generally close to ON/OFF crossover points whereas neurites in the OFF sublamina can travel long distances and terminate without crossing over to the ON sublamina. The combined effect of these factors is a VG3 plexus with roughly equal ON and OFF drives in the ON sublamina and a strongly OFF-dominated drive in the OFF sublamina (Figure 3.5F).

We next asked if the polarity of VG3-to-RGC synapses matched target RGC subtype polarity. We plotted the predicted polarity of the VG3-to-RGC synaptic drive with the known response polarity of the RGC subtypes (Figure 3.5F). The correlation coefficient between the predicted polarity of excitatory synapses to RGCs and the reported polarities of their subtype was 0.33 (95%CI = 0.22-0.42, Kruskal-Wallis P<0.0001). Notably, polarity variation between synapses to the same RGC type is large relative to differences between RGC types. However, the

model predicts enough distance between the synapses innervating monostratified OFF RGCs and monostratified ON RGCs that the overall polarity of their VGC drive is distinct (Figure 3.5F).

We next asked whether arbor stratification depth is sufficient to explain the response polarities delivered to different RGC subtypes or if higher-order synapse clustering was required. For instance, ON bipolar cells could preferentially innervate VG3 neurites presynaptic to ON RGCs. Using a similar Monte Carlo approach as our bipolar synapse redistribution, we found that the VG3-to-RGC polarities generated by 10,000 iterations produced differences in polarity comparable to those in the real data (Figure 3.5G,H). The observed difference in predicted polarities between synapses innervating monostratified OFF RGCs (4i, 4on, 4ow) and monostratified ON RGCs (6sw) was 0.47, very close to the median and 95% range (0.49, 0.35-0.64) of the stratification-based Monte Carlo. Therefore, differences in RGC stratification depth seem to be sufficient to produce the predicted differences in VG3 signal polarity.

We next asked if the bipolar cells that influence RGCs through the VG3 plexus also directly innervate the same RGCs. That is, does VG3 supplement bipolar cell input to RGCs with a surround-inhibited version of the same signals, or does VG3 provide a different channel of bipolar cell information? While reconstructing RGCs, we recorded synapses from bipolar cells also presynaptic to the VG3 plexus. We also used an apposition detection algorithm to perform a more systematic search for such synapses on three RGCs representing some of the most frequently innervated RGC subtypes (4ow, 5ti, and 37). Altogether, we identified 427 connections between bipolar cells that innervate the VG3 plexus and RGCs innervated by the VG3 plexus (Figure 3.6A). These connections were produced by 409 ribbon synapses (some ribbons innervated multiple RGCs).

Most subtypes of bipolar cell and RGC associated with VG3s had direct synaptic contact. For the three RGCs surveyed at every bipolar cell apposition, we found 45 inputs to the 4ow from shared bipolar cells (compared to 36 VG3 inputs), 42 shared inputs to the 5ti (38 VG3 inputs), and 45 shared inputs to the type 37 (22 VG3 inputs) (Figure 3.6B-D). Input from bipolar cells that also innervate the VG3 plexus appear to be a substantial portion of their total bipolar cell input. We found that shared inputs constituted 48.4% (4ow, 45 of 93), 68.9% (5ti, 42 of 61), and 60.0% (37, 45 of 75) of the bipolar cell input in these regions (Figure 3.6B-E). Given that not all VG3s and associated bipolar cells in the region have been reconstructed, these numbers represent a lower bound. VG3s, therefore, appear to be delivering an indirect, surround-suppressed version of transient bipolar cell responses to RGCs in parallel to direct innervation from the same pool of bipolar cells.
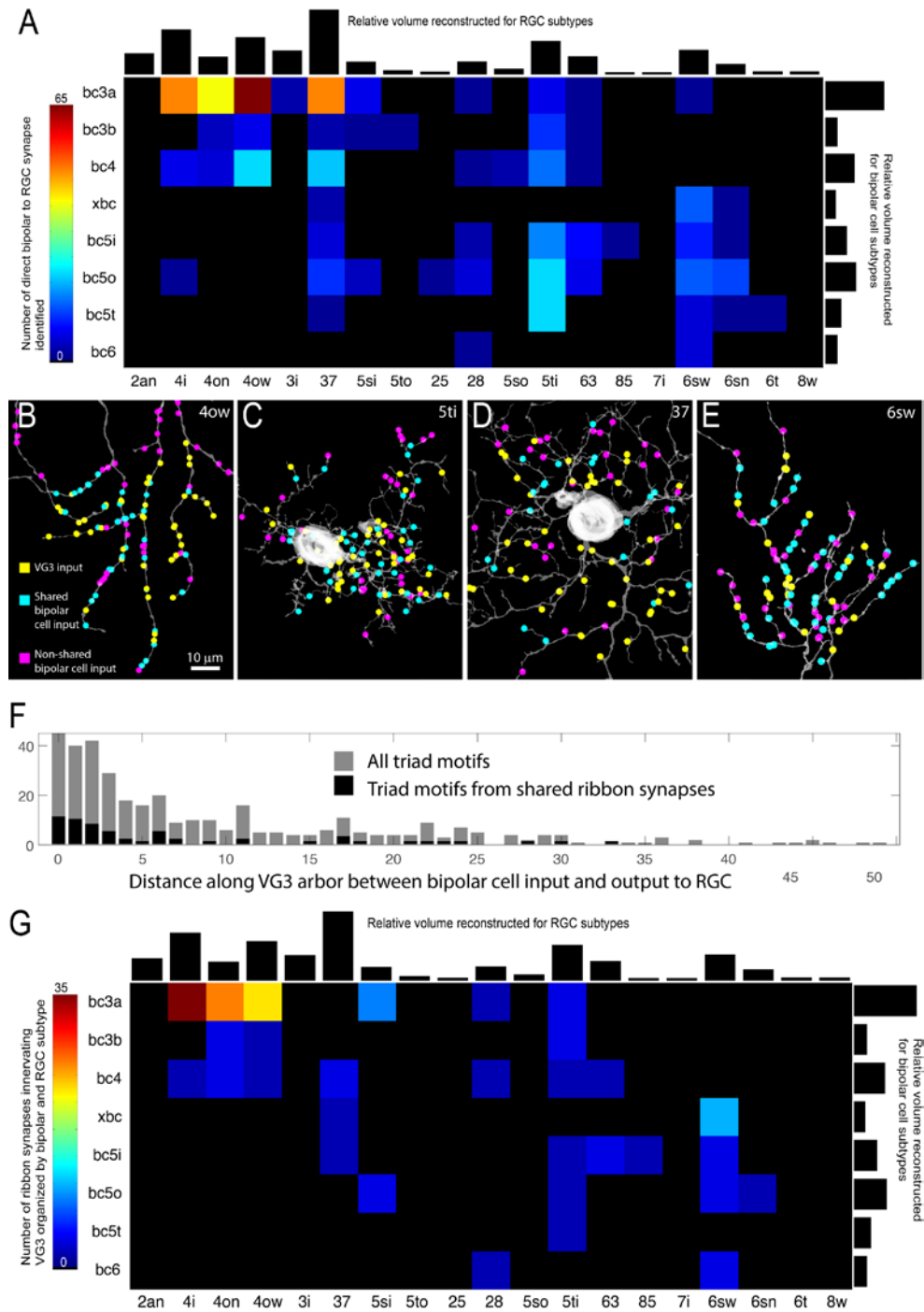
Figure 3.6. Shared and nonshared bipolar inputs to RGCs by bipolar cells presynaptic to VG3s. A) Direct innervation of RGCs by bipolar cells shows bipolar-RGC polarity agreement and overall pattern expected by arbor stratification overlap. B-E) All bipolar inputs were traced for sample RGCs from the 4 most frequently VGC-innervated subtypes, revealing a mix of VGC, shared bipolar, and non-shared bipolar input. F) Most RGCs sharing a ribbon input with a VG3 also received a VG3 synapse within a short distance. G) Number of shared ribbons with VG3 by postsynaptic RGC subtype and presynaptic bipolar type.

We next sought to determine whether the observed bipolar-VGC-RGC triad motifs reflect costratification of the participating cell types or a more local microcircuit. We measured the distances along VG3 neurites between the bipolar cell input and the output synapse to the RGC to determine how local the action of feed-forward excitation might be. The median distance between the VG3 input and output was 13.0 µm with only 5.6% under 1 µm (Figure 3.6F). This median distance between corresponds to a signal attenuation to 44.5% using our length constant of 16 µm. Therefore, while ultrastructurally compact, submicron-triad motifs were rare in the VG3 circuit, though most feedforward triads occurred at distances where the VG3 signal would retain significant influence from a shared bipolar cell input.

A special case of the triad motif is where the BC-VG3 and BC-RGC synapses were formed by the same bipolar cell ribbon synapse dyad. All the ribbon synapses innervating VG3 also innervated one (222 of 259 ribbons (86%)) or two (37 of 259 ribbons (14%)) other neurons. RGCs comprised 48% of the non-VG3 cells sharing these ribbons (the rest being amacrine cells). Of the RGC ribbon partners, 89.5% (119 of 133) were innervated by the VG3 plexus (Figure 3.6F). This percentage is a lower bound as both the VG3 and RGC reconstructions are incomplete. Therefore, an RGC sharing a ribbon synapse with a VG3 was a strong predictor that the RGC also received input from the VG3 plexus.

3.4 Discussion

Many retinal amacrine cell types exhibit clear directionality in the flow of information through their arbors. The primary input and output synapses of AII amacrines are segregated into

different strata of the inner plexiform layer of the retina (Marc et al., 2014). This arrangement provides for cross-channel inhibition of the OFF cone pathway by the rod pathway. In the case of starburst amacrine cells, the flow of information is not between strata, but laterally / centrifugal (J. S. Kim et al., 2014). The proximal-to-distal sequence of different types of inputs and then output synapses allows for the direction selective summation of signals of each starburst amacrine cell branch to be delivered to distinct target cells. Polyaxonal amacrine cells segregate input and output synapses into almost entirely separate arbors, integrating inputs locally and using long axon-like neurites to signal across distances of millimeters (Famiglietti, 1992a).

In contrast, the input and output synapses of the VG3 amacrine cells reconstructed here are evenly intermixed in the same strata and neurites. This intermixing results in a distinct network organization. VG3s generate a plexus that spans the center of the motion-sensitive IPL and distributes a signal that is complementary to the transient bipolar cells of a given depth and retinal position. The signal is complementary in that: 1) It is partially matched to nearby bipolar cells in terms of spatial position and polarity. 2) It is transmitted to the same RGCs that are innervated by the nearby bipolar cells. 3) The VG3 signal adds selectivity for small moving objects (surround inhibition) and looming stimuli.

Close intermixing of inputs and outputs on the VG3 arbor is similar to some other amacrine cells and as well as local inhibitory neurons in the dorsal lateral geniculate nucleus that generate inhibitory synaptic triads. In the retina a common synaptic motif is for an amacrine cell to deliver inhibition to a bipolar cell terminal that innervates it (Dowling & Boycott, 1966) or to a postsynaptic target of a bipolar cell terminal that innervates it. These synapses occur close enough together that the modulatory effect of the amacrine cell output can be seen as synapse specific, that is, it is primarily driven by the bipolar cell bouton that innervates it or that

innervates its target neurite. The feedforward excitation of VG3s does not appear to be synapse specific. The average input and output synapse on the VG3 arbors are far enough apart that output synapses are unlikely to be primarily driven by a single input synapse.

By reconstructing a network of mouse VG3s and their partners and combining this information with characterization of the response properties of the VG3 neurites, we attempted to provide a detailed view of the flow of visual information through a plexus of mixed input/output neurites. To our knowledge, there is not a previous connectomic reconstruction that combines subcellular calcium signals in this way. We found that the response properties of VG3s reflect a spatially biased mixing of their bipolar cell inputs. The short length constant for calcium spread means that different VG3 output synapses are influenced by different populations of VG3 inputs. At the same time, the large fraction of synapses from type 3a bipolar cells means that all output synapses should have a significant component of fast transient OFF drive.

The synaptic targets of the VG3 include most of the RGC types stratifying in or near the central band of transient bipolar cell terminations in the IPL (between the OFF and ON ChAT bands). Most of these RGCs are innervated by the same bipolar cell types that innervate the VG3 plexus. We observe this pattern across the RGC types most frequently innervated by the VG3s (transient OFF-alpha RGCs, W3 RGCs, and ON-OFF Direction Selective RGCs), which all receive a large amount of drive from the same bipolar cells as the VG3s (Fig 9B-D). The primary mode of transmission of VG3s is therefore to provide excitatory drive in parallel to the direct bipolar cell input they receive. This VG3 drive, however, is highly suppressed by activity in the surround of the VG3 receptive field. RGCs sampling from the transient band of the IPL, therefore, have an additional excitatory channel to sample from, one that includes built-in surround suppression.

Chapter 4

A polyaxonal amacrine cell exclusively targets the VGluT3 Amacrine Cell

4.1 Introduction

Information flow through the retina can be broadly divided into "vertical" and "horizontal" flow. Vertical flow concerns processing of information from one location in visual space, from the photoreceptors to the bipolar cells to the retinal ganglion cells (RGC), which project their axons out of the retina (Masland, 2001). Horizontal flow concerns comparing information from different locations, times, or visual pathway, and these comparisons allow discernment of edges and their orientations, motion and the motion of objects in the visual scene, and other complex visual features (Cook & McReynolds, 1999).

   Amacrine cells are retinal interneurons which perform many horizontal information processing tasks, and, across their 30-50 subtypes, their morphologies include both tightly stratified and diffuse neuronal arbors ranging in size from dozens to thousands of microns (Kolb, 1997; Kolb et al., 1981). Amacrine cells, named for their typical lack of axons, often instead have both their input and output synapses located on the same arbor branches. Amacrine cells target bipolar cells, other amacrine cells, and ganglion cells primarily with inhibitory synapses,

though some types additionally use excitatory neurotransmitters or gap junctions (reviewed in (Masland, 2012)) (Marc et al., 2018).

The vesicular glutamate transporter 3-expressing amacrine cell (VG3) is a small field amacrine cell which responds to local object motion as well as expanding dark spots, also called "looming" stimuli (T. Kim et al., 2020). VG3 are necessary for a mouse's "freeze or flee" response to looming stimuli. Patch-clamp recordings of VG3 responses to visual stimuli projected onto live retinas show that VG3 receive strong surround inhibition during global motion (T. Kim et al., 2015), and electron microscopic studies observed that inhibitory synapses from other amacrine cells outnumber excitatory bipolar inputs by approximately 2:1 (Friedrichsen, submitted). However, the types, morphologies, locations, and response characteristics of this population of amacrine cells remain unknown.

Polyaxonal amacrine cells (PAC) are medium to wide field amacrine cells with distinct axon-like processes separate from their dendritic arbors which can extend for several millimeters (Lin & Masland, 2006). Early Golgi staining studies showed their dendritic arbors to have few thick branches with many spines and which have a smaller span than the axon-like processes (Kolb et al., 1981, p. 81). Neurobiotin injection revealed that some PACs use gap junctions to electrically couple their dendritic arbors to other PACs of the same type or to RGCs, creating a network which can integrate information across a wide area of the retina and influence RGC activity and coordination (Ackert et al., 2007; Famiglietti, 1992a; Roy et al., 2017; Völgyi et al., 2009).

Polyaxonal amacrine cells match many of the predicted characteristics of the amacrine cells providing surround inhibition to VG3. Pharmacological manipulations blocking sodium channels and GABA receptors indicated that VG3 surround inhibition received during global

motion is provided by a population of spiking, GABA-ergic amacrine cells (Lee et al., 2014; Tien et al., 2015), which describes some types of PAC (Murphy-Baum & Taylor, 2015; Taylor, 1996). Thirty years ago, Famiglietti hypothesized from their distribution in the ventral retina and cone innervations that a possible role for a type of rabbit PAC could be enhancing detectability of small moving objects against a blue sky (Famiglietti, 1992b), a stimulus which elicits a strong response in VG3 (T. Kim et al., 2020). More recently, it was hypothesized that local object motion sensing RGCs are inhibited during global motion by transient, wide-field, polyaxonal amacrine cells (Ölveczky et al., 2003). The VG3 shares many response characteristics with the object motion sensing RGCs (T. Kim et al., 2015; Y. Zhang et al., 2012). It is possible that a wide-field, transient, PAC could also provide surround inhibition for the VG3.

Several types of wide field amacrine cells, some with axon-like processes, have been described which stratify in the same area of the IPL as the VG3. In the rabbit retina, the polyaxonal "PA1" cell has both its dendritic and axon-like arbors at the boundary between the ON and OFF sublamina of the IPL (Famiglietti, 1992a). A later study described a wide field "WF3-2" amacrine, reported to be equivalent to the PA1 (MacNeil et al., 1999; MacNeil & Masland, 1998). In the mouse, sparse labeling of amacrine cells revealed several types of polyaxonal amacrine cells (Badea & Nathans, 2004). A following study further characterized mouse wide field amacrine cells and described the "WF2-1", which has a dendritic arbor with a diameter ~340um at the ON OFF boundary of the IPL and an axon-like arbor which costratifies with the dendrites and extends to a diameter of ~3mm (Lin & Masland, 2006).

In our recent correlated light and electron microscopy study, we characterized the bipolar cell and RGC types synaptically connected to the VG3 to better understand its contributions to detecting object motion and background uniformity (Friedrichsen, submitted). We encountered a

PAC which almost exclusively targets VG3s with its axon-like processes. The dendritic arbor of this PAC also stratifies at the border between the ON and OFF sublamina of the IPL, where it is often innervated by VG3. Here, we give a description of the synaptic specificity, connectivity to other retinal neuron types, and morphology of this VG3-associated PAC (named "PACv").

4.2 Materials and Methods

This study utilizes a previously published multi-resolution correlated light and electron microscopy dataset comprising a high-resolution (4 nm xy, 40 nm z) ultrathin serial section electron microscopy (EM) volume (100 µm x 100 µm x 40 µm) of the inner plexiform layer of a mouse retina. This image volume is in the center of a lower resolution (20 nm xy, 40 nm z) EM volume including the surrounding area of retina (600 µm x 600 µm x 40 µm) (Friedrichsen et al., 2022).

This dataset was created to study the subcellular organization of the VG3 and its synaptic connectome. A large number of neuronal arbors and synapses were manually traced, including 12 partial VG3 arbors, 47 identified RGCs, 101 identified bipolar cells, 25 presumed PACv, and 529 non-PACv amacrine processes. When possible, annotation of RGC, PACv, and VG3 arbors was extended into the medium resolution EM to aid in cell type identification.

The following criteria were developed distinguish PACv processes from other amacrine types. Separate criteria were developed for dendritic and axon-like processes. Tracing of a PACv neurite began at its point of synaptic contact with a VG3.

For Dendritic Branches:

1. Branch contains only input synapses.

2. Medium to large neuritic diameter, sparsely branching, and stratifying at the ON-OFF boundary.

3. Cell body located in or near the INL.

For Axon-like Processes:

4. Branch contains only output synapses.

5. Consistent small diameter interspersed with nodes containing output synapses and mitochondria.

6. Branch divides rarely and at approximately 90-degree angles.

7. Branch has nearly no output synapses targeting bipolar cells or RGCs.

8. Branch has nearly no output synapses targeting non-VG3 amacrines.

These criteria resulted in many putative PACv branches, including both dendrites and axon-like processes as well as several partial arbors containing PACv cell bodies.

For the PACv with the most complete dendritic arbor reconstruction, we classified all input synapses as innervation from a bipolar cell, a VG3, or a non-VG3 amacrine cell.

To assess the proportion of amacrine input onto VG3 which is contributed by PACv, we traced amacrine cells presynaptic to VG3 for all synapses within a small central region of the high-resolution EM volume. Each amacrine neurite presynaptic to VG3 was traced until it had either violated the aforementioned PACv criteria or had exited the volume or become otherwise untraceable due to neurite diameter or imaging artifact.
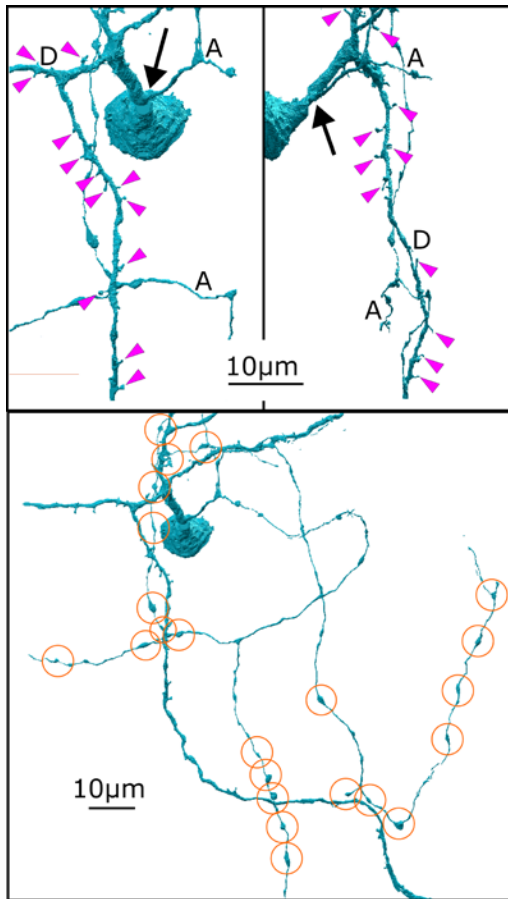
Figure 4.1. The morphology of the PACv neuritic arbor. The PACv dendrites (D) have many short spines which curve backward (magenta arrows). The axon-like processes (A) emerge from the proximal dendrite near the soma (black arrow) and then proceeded with a constant diameter, interrupted by boutons containing VG3-targeting synapses. (Friedrichsen et al., in preparation)

4.3 Results

While characterizing the VG3 connectome, we found a population of medium or wide field retinal neurons which had soma in the INL and dendritic arbors at the ON/OFF boundary of the IPL. Their dendritic arbors were sparsely branching, had many short spines, and received inputs from bipolar cells and amacrine cells, including the VG3. One of the somas was located within our high-resolution imaging volume, and we found that it additionally had an axon-like arbor which emanated from one of its dendrites near the soma (Figure 4.1). The axon-like processes were thin and uniform, branched rarely, received no synaptic inputs, and were interrupted at regular intervals by boutons where it formed output synapses almost exclusively with VG3. We dubbed this cell the VG3-associated PAC, or "PACv", reflecting its apparent synaptic exclusivity. It should be noted that our characterization of the PACv is derived from a limited number of partial arbors and dendritic or axon-like processes. Our 3D-EM imaging volumes were chosen to study the much smaller VG3, and thus we were unable to reconstruct the entirety of either PACv dendritic or axon-like arbors. However, we were able to document the types of cells providing synaptic inputs on the proximal dendritic branches within

approximately 50um of a PACv cell body, as well as characterize the synaptic targets of their axon-like processes.
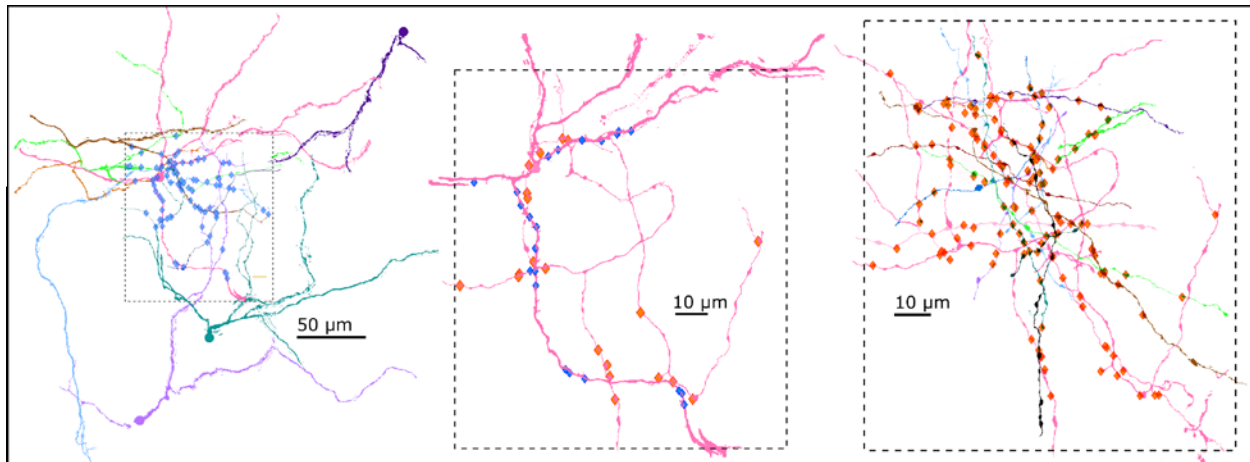
Figure 4.2. Reconstructed PACv neurites with VG3-connected synapses. The dashed box represents the boundaries of the high-resolution imaging volume where synapses were annotated. PACv dendritic arbor branches (left) received 87 synapses from VG3, and VG3 received 135 synapses from PACv axon-like processes (right). The PACv with both dendritic and axon-like processes traced (center) received 26 synapses from VG3 and contributed 27 synapses to VG3. (Friedrichsen et al., in preparation)

We reconstructed 8 partial PACv dendritic arbors. The most complete arbor had 6 branches extending radially from the soma. The dendrites branched minimally and had many small spines which curved back toward the soma. Dendrites maintained tight stratification at between 37%-47% IPL depth, near the boundary between the ON and OFF sublamina of the IPL. The PACv dendritic arbor targeted for full synaptic reconstruction was innervated 172 times. Synapses were contributed by both amacrine and bipolar cells, with approximately twice as many amacrine as bipolar inputs to give an excitatory/inhibitory ratio of 0.483 (56 vs 116). PACv dendrites received a mix of ON and OFF bipolar cell ribbon synapses (23 ON vs 33 OFF), and 37.5% of bipolar inputs were from bipolar cells which also innervated the VG3 plexus. We did not observe any obvious spatial patterns in synapses distributions, either radially or by IPL depth. We reconstructed 18 PACv axon-like processes, upon which we identified 147 output synapses, with 91.8% (135) targeting VG3 partners. When we located PACv output synapses onto unidentified cells, the unidentified branch could often be traced back to a VG3 arbor,

leading to the annotation of multiple VG3 arbor branches which had not been previously traced due to imaging volume borders or imaging artifacts. Of the 12 synapses that targeted other cells, 6 targeted a specific non-VG3 amacrine cell. We are confident this amacrine cell is not a VG3, because it did not express the calcium reporter under the vGluT3 promotor, had a single proximal dendrite which led to a thin, monostratified arbor restricted to the ON sublamina of the IPL, and received synaptic input from VG3 (which do not innervate each other).

The majority of VG3 synaptic connections are with other amacrine cells (65.4% of inputs and 58.5% of outputs). Within our sampled region, PACv contributed 29.5% (26 of 88) of amacrine input synapses on VG3 branches. Of the VG3 output synapses to amacrine cells, 14.9% (91 of 611) targeted PACv dendritic arbors.

The axon-like processes of PACv pass in close proximity to their dendritic arbors. The densities of the overlapping PACv dendritic and axon-like plexuses and the frequency of VG3 connections gives a mean Euclidean distance from a PACv to VG3 synapse (n=135) to the nearest VG3 to PACv synapse (n=91) of under 5 µm (mean=4.8 µm, median=4.1 µm).

4.4 Discussion

In this report we describe the morphology and synaptic connectivity of the PACv, a polyaxonal amacrine cell whose axonal processes specifically target VG3. The PACv is consistent with the descriptions of a putative wide field amacrine source of the surround inhibition which allows the VG3 to discriminate between local and global motion. The PACv is responsible for a significant portion VG3 inhibitory input (29.5%) and does not significantly innervate any other cell types (over 90% of PACv outputs target VG3). The VG3 devotes a significant portion of its synaptic output onto PACv dendrites, with synapse numbers comparable

to its most frequently targeted RGC types. The synapses contributed by VG3 make up over 20% of PACv amacrine inputs.
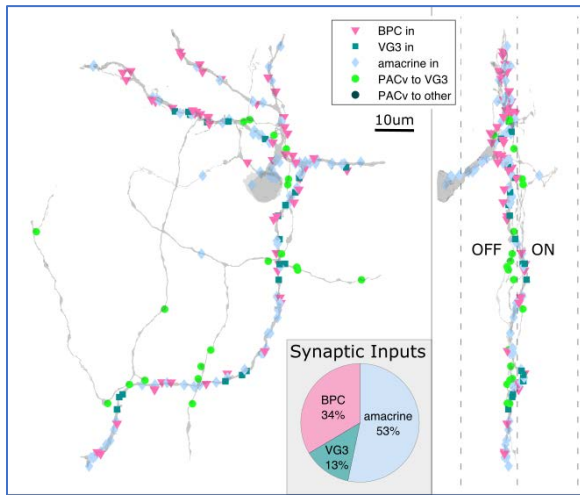
Figure 4.3. The distributions of synapses on the most completely reconstructed PACv arbor. Synapses are classified as innervations by bipolar cells, VG3, or unknown amacrine cells. We saw no obvious synapse density differences either radially or in IPL depth. (Friedrichsen et al., in preparation)

An outstanding question regarding the communication between the VG3 and the PACv is whether the innervations from VG3 to PACv are excitatory or inhibitory. Whereas most amacrine cells are strictly synaptically inhibitory and use GABA or glycine, the VG3 forms either glutamatergic or glycinergic synapses with its targets. The VG3 targets RGCs with either type of synapse, but it is unknown whether it targets any amacrine cells with excitatory synapses. A different type of PAC, the PAS4/5, receives direct glycinergic input from VG3, demonstrated in mice using an optogenetic approach (Jia et al., 2020). However, the PAS4/5 is located deep in the sustained ON sublamina of the IPL and has response properties similar to suppressed-by-contrast (SbC) RGCs, which also receive glycinergic input from the VG3 (Tien et al., 2016). The PACv dendritic arbor stratifies in the middle of the IPL, where it is contacted by many of the same bipolar cells which innervate the VG3 plexus. Many of the retinal neurons with arbors at the ON-OFF IPL boundary are responsive to motion, in contrast to the PAS4/5 and SbC-RGCs.

Further study is required to understand the role of the PACv in retinal processing, object motion sensing, and contributions to the function of the VG3. First, it must be confirmed that the VG3-targetting axon-like processes belong to the same population of amacrine cells as the

dendritic arbors we observed, because there was only a single PACv soma within our high-resolution volume where we could locate the point where the axon-like process emerged from the dendrite. More examples of PACv morphology will also aid in determining if the PACv is indeed the same amacrine type as the WF2-1, described by Lin and Masland (2006). Lastly, multiple PAC types have been found to engage in both homotypic and heterotypic coupling to RGCs and other amacrine cells via gap junctions. Coupling by the PACv could extend its receptive field and affect how the PACv plexus integrates inputs from VG3 and other amacrine cells, as well as provide an additional pathway by which the VG3 can influence the activity of RGCs outside its synaptic connectome.

Chapter 5

Discussion

5.1 Overview

The work presented here utilizes correlated light and electron microscopy to study subcellular processing in the unique VG3 amacrine cell, a dual-neurotransmitter retinal neuron which responds to local object motion. The VG3 integrates information both locally and globally, with individual branch regions responding heterogeneously depending on local inputs, but with a shared background signal provided by heavy innervation by a single bipolar cell type. The VG3 targets retinal neurons in multiple visual pathways with either excitatory or inhibitory object-motion-selective synaptic drive. Additionally, the VG3 is integral to innate freezing behaviors in response to looming shadows.

We develop and implement a multi-resolution correlated light and electron microscopy approach in the VG3 to spatially correlate two-photon calcium and confocal structural light microscopy imaging with 3D-EM volumes at the level of individual arbor branch regions within the VG3 neuritic plexus. With characterizations of the precise morphology and connectivity underpinning the calcium signals from the dense VG3 plexus, we can deduce anatomical distances between calcium imaging ROI and uncover the proximity at which regions with differing response characteristics can coexist and how they mix in the intervening space.

Our mrCLEM dataset is the first large scale electron microscopic reconstruction of the detailed morphology of the VG3 dendritic plexus, and we report the relative distributions of input and output synapses throughout the plexus, as well as what proportions of input and output are derived from and targeted to different types of bipolar cell, amacrine cell, and RGC. We show that VG3 combines partially shared local bipolar input, a short length constant, and global surround inhibition to create an object-motion-selective channel which is transmitted in parallel to their synaptic targets.

We also elucidate how the distribution of synapses and the morphology of the arbor create an environment where input from many types of bipolar cell, with the fast transient bc3a predominating, is combined with a short length constant to locally integrate nearby inputs while retaining a global influence from the predominant bipolar cell type.

Finally, we encounter a type of polyaxonal amacrine cell, the PACv, which matches multiple descriptions of a transient, GABA-ergic, wide field, spiking amacrine cell which imparts object motion selectivity onto the VG3 via surround inhibition. Interestingly, the PACv exclusively targets VG3, despite having access to many of the same object-motion-selective targets that are innervated by VG3. Further, 15% of VG3 output synapses target the PACv dendritic arbor, though it is not known if these synapses are excitatory or inhibitory. The VG3-PACv amacrine-amacrine microcircuit allows the VG3 to use its highly local information to influence the PACv's extremely wide-reaching axon-like arbor which, in turn, provides VG3 with feature-specific surround inhibition.

5.2 Subcellular Processing in the Retina

If the retina tried to transmit raw photoreceptor signals directly to the brain, the optic nerve would be larger than the eyeball, as photoreceptors outnumber ganglion cells over 100 to 1

(Jeon et al., 1998). Likewise, if the retina tried to fully process all aspects of visual information, the necessary volume of neural circuitry could not fit inside the eyeball. The retina must perform enough processing to sparsely code all relevant visual information, but it must do so as efficiently as possible. Increasing the drive for efficient processing is the fact that the photoreceptors are on the back of the retina. Therefore, the retina must be thin enough to be optically transparent, since photons must travel through the RGCs, amacrine cells, bipolar cells, and horizontal cells before reaching the photoreceptors. Compact, metabolically efficient retinal circuitry minimizes the necessary number of cells and amount of vasculature, thus minimizing scattering and absorption of incoming photons and maximizing the number of photons available to the photoreceptors.

Though the neuron types and processing steps are broadly the same across the retina (excluding the optic disc and fovea), there is no specific group of cells or circuits forming a retinal 'subunit' that repeats across the retina. Instead, the arbors of each type of bipolar cell, horizontal cell, amacrine cell, and RGC form a meshwork with unique computational properties determined by the cell spacing, arbor overlap, and degree of homotypic repulsion. When processing at this subcellular level, the local connections of a specific branch region can have a larger influence on its function than which arbor it belongs to. For example, two nearby branches originating from distant cell bodies may function more similarly to each other than to distant branches of their own arbors, due to shared local connectivity. This overall framework of overlapping meshworks operating at the subcellular level is highly flexible, with each area of the retina able to optimally extract visual information at that location in space by varying the densities and connections of the different cell type meshes. For instance, the degree of object motion selectivity in RGC responses in one area of retina can be tuned by varying the density,

synaptic connectivity, or immediate response characteristics of the arbors of the W3-RGCs, VG3, amacrine cells providing surround inhibition, or cone bipolar cells.

Within a single neuron, subcellular processing can occur simultaneously at different spatial scales. Both local and global integration occur within the arbor of the VG3. The two arbor regions where VG3 receives OFF and ON transient bipolar cell inputs are close in physical space, with only 5-10 microns of distance between bipolar inputs of opposite polarity. Such proximity between the two excitatory input regions would theoretically result in rampant signal mixing. However, inhibitory inputs to the VG3 arbor outnumber excitatory inputs by 2 to 1, and the ratio reaches over 5:1 in the depth band between the two bipolar input bands. This area of intense inhibition could serve to help electrically isolate the OFF and ON VG3 arbors from each other. However, inputs from the bc3a bipolar cells comprise half of all excitatory inputs to the VG3 arbor, and our model of signal spread in the VG3 arbor predicts that this strong transient OFF excitation will be able to bulldoze its way through the inhibitory region and reach all but the most distant parts of the arbor. This global fast OFF signal can still be observed in VG3 regions where local excitation is strictly ON in polarity. The inhibitory region does efficiently prevent ON signals from crossing the border, creating a unidirectional global integration pathway selective for response polarity.

5.3 Why even have a VG3?

VG3 is selective for object motion, a property that is found more commonly in RGCs than amacrine cells. Indeed, if the OMS-RGCs can compute object motion themselves using the same central excitation and global motion surround inhibition as the VG3, why is the VG3 necessary? A leading theory is that the delay introduced by the VG3 acting as an intermediary

between bipolar cells to the OMS-RGC improves object motion selectivity. Timing is key in discriminating between object motion and global motion. In global motion, the timing of motion in the surround is precisely the same as in the receptive field center. However, in the circuitry of the retina, the motion information must travel through the inhibitory amacrine cells in the surround prior to being transmitted to the central OMS-RGC, thus there is a very slight delay in inhibition to the OMS-RGC. The VG3 introduces a slight delay in the OMS-RGC's central excitation, better synchronizing it with the surround inhibition. Additionally, the inclusion of VG3 in this circuit introduces a third level at which center-surround interactions can occur (bipolar, amacrine, and RGC).

Besides enhancing object motion selectivity in its RGC targets, the inclusion of VG3 in retinal processing improves overall computational efficiency. The retina must be optically transparent, and, therefore, thin. The five most frequently innervated VG3 target RGC types (W3, F-mini-on, transient OFF and ON alpha RGCs, and ON-OFF direction selective RGC) comprise a significant portion of total RGCs (~30-40%). Each VG3 collects hundreds of bipolar and amacrine inputs from both the ON and OFF transient zones of the IPL to robustly compute local object motion. Rather than requiring each of the VG3 target types to extend arbor branches the center of the IPL and independently gather the relevant channels of information, the VG3 plexus calculates this ON-OFF OMS signal and transmits it to over one third of retinal RGCs.

5.4 Defensive Behaviors

Vision is important for evading predation, and, in animals ranging from mice to primates, a looming shadow overhead often elicits freezing or fleeing (reviewed in (Wu & Zhang, 2023)). The VG3 is necessary and sufficient for initiating this escape behavior (T. Kim et al., 2020), as

are the transient-OFF-alpha RGCs (established by work in Chapter 3 to be a primary target of VG3), as are the targets of the transient-OFF-alpha RGCs in the medial superior colliculus (Wang et al., 2021). Stimulation or ablation of any of these three neuron populations can potentiate or diminish the fleeing response to a looming stimulus.

The VG3 thus provides access to a direct, labeled-line, reliable pathway from visual stimulus to an innate, observable behavior. Innate, reliable behaviors such as those elicited by looming stimuli facilitate behavioral neuroscience research. Already, multiple studies have begun to delve into how defensive behaviors are modified by social interaction, previous experience, stress, alcohol consumption, and other environmental factors (Lenzi et al., 2022; Narushima et al., 2022; Neira et al., 2022; Tafreshiha et al., 2021). Importantly, this visually-evoked pathway gives easy and reliable access to the Defense Cascade, which is highly relevant in mental health research on post-traumatic stress disorder, peritraumatic stress, early life stress, and substance abuse (Calanni et al., 2022; Kozlowska et al., 2015). For this pathway to be maximally useful, it is important to understand the retinal circuitry underlying its initiation and how the characteristics of the stimulus and visual scene are integrated within the retina. This was highlighted by a finding that slight differences in visual stimuli can have a large effect on the type of defensive behavior initiated.

Freezing and fleeing are mutually exclusive responses, and yet both may be evoked by looming stimuli. The determination of whether a defensive response should be active (flee) or passive (freeze) is as critical to survival as the initial detection of a threat. A visual stimulus of a small dark stimulus moving across the sky (a "sweeping" stimulus) can also elicit freezing or fleeing. Both sweeping and looming stimuli prompt strong responses from VG3. Studies have compared responses from sweeping and looming stimuli and found that sweeping stimuli are

more likely result in freezing while a looming stimulus will cause the mouse to flee (De Franceschi et al., 2016; D. Liu et al., 2022; X. Yang et al., 2020). This result makes sense, as a sweeping stimulus could represent a more distant predator that is not yet aware of the observer, while a looming stimulus represents a more imminent threat that is quickly closing distance. A recent study reported that ablating specific populations of SC-projecting RGCs resulted in mice differentially impacted in either freezing or fleeing and only in response to looming or sweeping stimuli, suggesting that responses from distinct RGC types may underlie the initial calculation of which defense strategy is optimal (Lees et al., 2020). However, the strategy chosen has also been shown to be modulated by multiple projections between areas of the brain, and this question continues to be an extremely active area of research (Campagner et al., 2023; Deichler et al., 2020; Fratzl et al., 2021; Ma et al., 2021; Reinhard et al., 2019; Shang et al., 2018; Storchi et al., 2020; Wheatcroft et al., 2022).

5.5 The VG3 and the PACv

The PACv and VG3 both receive excitatory inputs from both transient OFF and ON bipolar cells and inhibitory inputs from other amacrine cells. About half of PACv bipolar inputs come from the same population of bipolar cells as VG3, which is similar to the proportion of bipolar inputs shared between VG3 and the transient-OFF-alpha RGC, with which the PACv closely costratifies. Additionally, they each contribute significant synaptic input to the other, with approximately 20% of PACv amacrine input coming from the VG3 and 30% of VG3 inhibitory input coming from PACv.

The scales at which they integrate their respective inputs, though, are quite different. Drawing upon descriptions of the PA1, WF3-2 and WF2-1 polyaxonal amacrine cells and from

our medium-resolution reconstructions, the dendritic arbor is likely between 300 and 600 µm across. The axon-like processes of the PACv likely extend much farther across the retina, up to several millimeters.

Why is PACv output seemingly exclusive to VG3? If PACv coverage and density are close to observations in other polyaxonal amacrine cells, a wide network of PACv dendrites receive thousands of excitatory and inhibitory synapses and integrates them to compute a probable global motion signal. This signal is then transmitted significant distances along extensive axon-like processes through the middle of the motion-sensitive strata of the IPL, and yet this useful channel of information is only provided to VG3, despite having many appositions with multiple RGC types, which, like the VG3, are selective for local object motion.

Another outstanding question concerns the necessity of the PACv for the function of VG3 and vice versa. As a significant contributor of inhibitory amacrine input from the surround, PACv is likely crucial for VG3 to discriminate between global motion and local object motion. Meanwhile, VG3 contributes a significant portion of amacrine input for the PACv and may also be crucial for PACv to sense motion or differentiate between local and global motion. This arrangement poses somewhat of a chicken and egg question where both the VG3 and PACv partially drive their own feature selectivity via significant synaptic connections with each other.

5.6 Future Directions

A fundamental question in neuroscience is how neuronal branch morphology and synapse distributions influence the flow of information through the arbor branches. In this work, we examined a unique retinal amacrine cell, the VG3, which has intermixed input and output synapses and is able to discern local object motion and provide that information via excitatory or

99

inhibitory synapses to specific types of amacrine cell and RGC in object-motion-sensing or uniformity detection and global motion pathways.

Our survey of synaptic targets of the VG3 uncovered several previously unknown RGC connections, as well as quantified existing synaptic relationships. This information can be used for future studies to target electrophysiological techniques like dual patch clamp to measure how VG3 influences target cells on an individual basis.

Polyaxonal amacrine cells and wide field amacrine cells are still a largely unknown group of retinal neurons. Studies over the past few decades have discovered homotypic coupling via gap junctions, as well as heterotypic coupling to multiple types of RGC. Most of the work characterizing polyaxonal amacrine cells has been in rabbits and primates. With the discovery of significant PACv participation in the VG3 microcircuit, a better understanding of the interplay between these two unique amacrine cells is needed. Electrophysiological approaches have appeal since the timing of the mutual inhibition between VG3 and PACv is likely critical to the balance of activity between the two.

References/Bibliography/Works Cited

Ackert, J. M., Farajian, R., Chheda, S., Volgyi, B., & Bloomfield, S. A. (2007). ON Direction Selective Ganglion Cells Display a Directional OFF Response Received via Gap Junctions With Polyaxonal Amacine Cells. *Investigative Ophthalmology & Visual Science*, *48*(13), 1162.

Anderson, J. R., Jones, B. W., Watt, C. B., Shaw, M. V., Yang, J.-H., DeMill, D., Lauritzen, J. S., Lin, Y., Rapp, K. D., Mastronarde, D., Koshevoy, P., Grimm, B., Tasdizen, T., Whitaker, R., & Marc, R. E. (2011). Exploring the retinal connectome. *Molecular Vision*, *17*, 355–379.

Aoyagi, Y., Kawakami, R., Osanai, H., Hibi, T., & Nemoto, T. (2015). A Rapid Optical Clearing Protocol Using 2,2′-Thiodiethanol for Microscopic Observation of Fixed Mouse Brain. *PLoS ONE*, *10*(1), e0116280. https://doi.org/10.1371/journal.pone.0116280

Azeredo da Silveira, R., & Roska, B. (2011). Cell types, circuits, computation. *Current Opinion in Neurobiology*, *21*(5), 664–671. https://doi.org/10.1016/j.conb.2011.05.007

Baccus, S. A. (2007). Timing and computation in inner retinal circuitry. *Annual Review of Physiology*, *69*, 271–290. https://doi.org/10.1146/annurev.physiol.69.120205.124451

Badea, T. C., & Nathans, J. (2004). Quantitative analysis of neuronal morphologies in the mouse retina visualized by using a genetically directed reporter. *Journal of Comparative Neurology*, *480*(4), 331–351. https://doi.org/10.1002/cne.20304

Bae, J. A., Mu, S., Kim, J. S., Turner, N. L., Tartavull, I., Kemnitz, N., Jordan, C. S., Norton, A. D., Silversmith, W. M., Prentki, R., Sorek, M., David, C., Jones, D. L., Bland, D., Sterling, A. L. R., Park, J., Briggman, K. L., & Seung, H. S. (2018). Digital Museum of Retinal Ganglion Cells with Dense Anatomy and Physiology. *Cell*, *173*(5), 1293-1306.e19. https://doi.org/10.1016/j.cell.2018.04.040

Baena, V., Schalek, R. L., Lichtman, J. W., & Terasaki, M. (2019). Serial-section electron microscopy using Automated Tape-Collecting Ultramicrotome (ATUM). *Methods in Cell Biology*, *152*, 41–67. https://doi.org/10.1016/bs.mcb.2019.04.004

Ball, W., & Tronick, E. (1971). Infant Responses to Impending Collision: Optical and Real. *Science*, *171*(3973), 818–820. https://doi.org/10.1126/science.171.3973.818

Barlow, H. B. (1953). Summation and inhibition in the frog's retina. *The Journal of Physiology*, *119*(1), 69–88. https://doi.org/10.1113/jphysiol.1953.sp004829

Barlow, H. B., Hill, R. M., & Levick, W. R. (1964). Retinal ganglion cells responding selectively to direction and speed of image motion in the rabbit. *The Journal of Physiology*, *173*(3), 377–407.

Berger, D. R., Seung, H. S., & Lichtman, J. W. (2018). VAST (Volume Annotation and Segmentation Tool): Efficient Manual and Semi-Automatic Labeling of Large 3D Image Stacks. *Frontiers in Neural Circuits*, *12*, 88. https://doi.org/10.3389/fncir.2018.00088

Bicknell, B. A., & Häusser, M. (2021). A synaptic learning rule for exploiting nonlinear dendritic computation. *Neuron*, *109*(24), 4001-4017.e10. https://doi.org/10.1016/j.neuron.2021.09.044

Bishop, D., Nikić, I., Brinkoetter, M., Knecht, S., Potz, S., Kerschensteiner, M., & Misgeld, T. (2011). Near-infrared branding efficiently correlates light and electron microscopy. *Nature Methods*, *8*(7), Article 7. https://doi.org/10.1038/nmeth.1622

Bock, D. D., Lee, W.-C. A., Kerlin, A. M., Andermann, M. L., Hood, G., Wetzel, A. W., Yurgenson, S., Soucy, E. R., Kim, H. S., & Reid, R. C. (2011). Network anatomy and in vivo physiology of visual cortical neurons. *Nature*, *471*(7337), 177–182. https://doi.org/10.1038/nature09802

Borst, A., & Egelhaaf, M. (1994). Dendritic processing of synaptic information by sensory interneurons. *Trends in Neurosciences*, *17*(6), 257–263. https://doi.org/10.1016/0166-2236(94)90009-4

Briggman, K. L., Helmstaedter, M., & Denk, W. (2011). Wiring specificity in the direction-selectivity circuit of the retina. *Nature*, *471*(7337), 183–188. https://doi.org/10.1038/nature09818

Brüggen, B., Meyer, A., Boven, F., Weiler, R., & Dedek, K. (2015). Type 2 wide-field amacrine cells in TH::GFP mice show a homogenous synapse distribution and contact small ganglion cells. *European Journal of Neuroscience*, *41*(6), 734–747. https://doi.org/10.1111/ejn.12813

Calanni, J. S., Dieguez, H. H., González Fleitas, M. F., Canepa, E., Berardino, B., Repetto, E. M., Villarreal, A., Dorfman, D., & Rosenstein, R. E. (2022). Early life stress induces visual dysfunction and retinal structural alterations in adult mice. *Journal of Neurochemistry*, *n/a*(n/a). https://doi.org/10.1111/jnc.15752

Campagner, D., Vale, R., Tan, Y. L., Iordanidou, P., Pavón Arocas, O., Claudi, F., Stempel, A. V., Keshavarzi, S., Petersen, R. S., Margrie, T. W., & Branco, T. (2023). A cortico-collicular circuit for orienting to shelter during escape. *Nature*, *613*(7942), Article 7942. https://doi.org/10.1038/s41586-022-05553-9

Chapot, C. A., Euler, T., & Schubert, T. (2017). How do horizontal cells 'talk' to cone photoreceptors? Different levels of complexity at the cone–horizontal cell synapse. *The Journal of Physiology*, *595*(16), 5495–5506. https://doi.org/10.1113/JP274177

Chen, M., Lee, S., & Zhou, Z. J. (2017). Local synaptic integration enables ON-OFF asymmetric and layer-specific visual information processing in vGluT3 amacrine cell dendrites. *Proceedings of the National Academy of Sciences*, *114*(43), 11518–11523. https://doi.org/10.1073/pnas.1711622114

Colbert, C. M., & Johnston, D. (1996). Axonal Action-Potential Initiation and Na+ Channel Densities in the Soma and Axon Initial Segment of Subicular Pyramidal Neurons. *The Journal of Neuroscience*, *16*(21), 6676–6686. https://doi.org/10.1523/JNEUROSCI.16-21-06676.1996

Cook, P., & McReynolds, J. (1999). Lateral inhibition in the inner retina is important for spatial tuning of ganglion cells. *Nature Neuroscience*, *1*, 714–719. https://doi.org/10.1038/3714

Coppola, D., & Purves, D. (1996). The extraordinarily rapid disappearance of entoptic images. *Proceedings of the National Academy of Sciences of the United States of America*, *93*(15), 8001–8004.

Costantini, I., Ghobril, J.-P., Di Giovanna, A. P., Mascaro, A. L. A., Silvestri, L., Müllenbroich, M. C., Onofri, L., Conti, V., Vanzi, F., Sacconi, L., Guerrini, R., Markram, H., Iannello, G., & Pavone, F. S. (2015). A versatile clearing agent for multi-modal brain imaging. *Scientific Reports*, *5*, 9808. https://doi.org/10.1038/srep09808

Davenport, C., Packer, O. S., Detwiler, P. B., & Dacey, D. M. (2006). Calcium Imaging in Primate A1 Amacrine Cells Reveals Evidence for Functional Polarity of Dendritic and Axon–Like Components. *Investigative Ophthalmology & Visual Science*, *47*(13), 2671.

de Boer, P., Hoogenboom, J. P., & Giepmans, B. N. G. (2015). Correlated light and electron microscopy: Ultrastructure lights up! *Nature Methods*, *12*(6), Article 6. https://doi.org/10.1038/nmeth.3400

De Franceschi, G., Vivattanasarn, T., Saleem, A. B., & Solomon, S. G. (2016). Vision Guides Selection of Freeze or Flight Defense Strategies in Mice. *Current Biology*, *26*(16), 2150–2154. https://doi.org/10.1016/j.cub.2016.06.006

De Robertis, E., & Franchi, C. M. (1956). Electron microscope observations on synaptic vesicles in synapses of the retinal rods and cones. *The Journal of Biophysical and Biochemical Cytology*, *2*(3), 307–318. https://doi.org/10.1083/jcb.2.3.307

Deichler, A., Carrasco, D., Lopez-Jury, L., Vega-Zuniga, T., Márquez, N., Mpodozis, J., & Marín, G. J. (2020). A specialized reciprocal connectivity suggests a link between the mechanisms by which the superior colliculus and parabigeminal nucleus produce defensive behaviors in rodents. *Scientific Reports*, *10*(1), 16220. https://doi.org/10.1038/s41598-020-72848-0

Demb, J. B., Haarsma, L., Freed, M. A., & Sterling, P. (1999). Functional circuitry of the retinal ganglion cell's nonlinear receptive field. *The Journal of Neuroscience: The Official Journal of the Society for Neuroscience*, *19*(22), 9756–9767. https://doi.org/10.1523/JNEUROSCI.19-22-09756.1999

Denk, W., & Detwiler, P. B. (1999). Optical recording of light-evoked calcium signals in the functionally intact retina. *Proceedings of the National Academy of Sciences*, *96*(12), 7035–7040. https://doi.org/10.1073/pnas.96.12.7035

Denk, W., Yuste, R., Svoboda, K., & Tank, D. W. (1996). Imaging calcium dynamics in dendritic spines. *Current Opinion in Neurobiology*, *6*(3), 372–378. https://doi.org/10.1016/s0959-4388(96)80122-x

Ditchburn, R. W., & Ginsborg, B. L. (1953). Involuntary eye movements during fixation. *The Journal of Physiology*, *119*(1), 1–17. https://doi.org/10.1113/jphysiol.1953.sp004824

Dowling, J. E. (1999). Retinal processing of visual information. *Brain Research Bulletin*, *50*(5), 317. https://doi.org/10.1016/S0361-9230(99)00154-9

Dowling, J. E., & Boycott, B. B. (1966). Organization of the primate retina: Electron microscopy. *Proceedings of the Royal Society of London. Series B, Biological Sciences*, *166*(1002), 80–111. https://doi.org/10.1098/rspb.1966.0086

Drawitsch, F., Karimi, A., Boergens, K. M., & Helmstaedter, M. (2018). FluoEM, virtual labeling of axons in three-dimensional electron microscopy data for long-range connectomics. *ELife*, *7*, e38976. https://doi.org/10.7554/eLife.38976

Enroth-Cugell, C., & Robson, J. G. (1966). The contrast sensitivity of retinal ganglion cells of the cat. *The Journal of Physiology*, *187*(3), 517–552. https://doi.org/10.1113/jphysiol.1966.sp008107

Euler, T., Detwiler, P. B., & Denk, W. (2002). Directionally selective calcium signals in dendrites of starburst amacrine cells. *Nature*, *418*(6900), 845–852. https://doi.org/10.1038/nature00931

Fairén, A., Peters, A., & Saldanha, J. (1977). A new procedure for examining Golgi impregnated neurons by light and electron microscopy. *Journal of Neurocytology*, *6*(3), 311–337. https://doi.org/10.1007/BF01175194

Famiglietti, E. V. (1991). Synaptic organization of starburst amacrine cells in rabbit retina: Analysis of serial thin sections by electron microscopy and graphic reconstruction.

Journal of Comparative Neurology, *309*(1), 40–70.
https://doi.org/10.1002/cne.903090105

Famiglietti, E. V. (1992a). Polyaxonal amacrine cells of rabbit retina: Morphology and
stratification of PA1 cells. *Journal of Comparative Neurology*, *316*(4), 391–405.
https://doi.org/10.1002/cne.903160402

Famiglietti, E. V. (1992b). Polyaxonal amacrine cells of rabbit retina: PA2, PA3, and PA4 cells.
Light and electron microscopic studies with a functional interpretation. *Journal of
Comparative Neurology*, *316*(4), 422–446. https://doi.org/10.1002/cne.903160404

Famiglietti, E. V., & Kolb, H. (1975). A bistratified amacrine cell and synaptic cirucitry in the
inner plexiform layer of the retina. *Brain Research*, *84*(2), 293–300.
https://doi.org/10.1016/0006-8993(75)90983-x

Faulk, W., & Taylor, M. (1971). Communication to the editors: An immunocolloid method for
the electron microscope. *Immunochemistry*, *8*(11), 1081–1083.
https://doi.org/10.1016/0019-2791(71)90496-4

Field, G. D., & Chichilnisky, E. J. (2007). Information processing in the primate retina: Circuitry
and coding. *Annual Review of Neuroscience*, *30*, 1–30.
https://doi.org/10.1146/annurev.neuro.30.051606.094252

Fratzl, A., Koltchev, A. M., Vissers, N., Tan, Y. L., Marques-Smith, A., Stempel, A. V., Branco,
T., & Hofer, S. B. (2021). Flexible inhibitory control of visually evoked defensive
behavior by the ventral lateral geniculate nucleus. *Neuron*, *109*(23), 3810-3822.e9.
https://doi.org/10.1016/j.neuron.2021.09.003

Freed, M., & Sterling, P. (1988). The ON-alpha ganglion cell of the cat retina and its presynaptic
cell types. *The Journal of Neuroscience*, *8*(7), 2303–2320.
https://doi.org/10.1523/JNEUROSCI.08-07-02303.1988

Fremeau, R. T., Burman, J., Qureshi, T., Tran, C. H., Proctor, J., Johnson, J., Zhang, H., Sulzer,
D., Copenhagen, D. R., Storm-Mathisen, J., Reimer, R. J., Chaudhry, F. A., & Edwards,
R. H. (2002). The identification of vesicular glutamate transporter 3 suggests novel
modes of signaling by glutamate. *Proceedings of the National Academy of Sciences*,
99(22), 14488–14493. https://doi.org/10.1073/pnas.222546799

Friedrichsen, K., Ramakrishna, P., Hsiang, J.-C., Valkova, K., Kerschensteiner, D., & Morgan, J.
L. (2022). Reconstructing neural circuits using multiresolution correlated light and
electron microscopy. *Frontiers in Neural Circuits*, *16*, 753496.
https://doi.org/10.3389/fncir.2022.753496

Fulton, K. A., & Briggman, K. L. (2021). Permeabilization-free en bloc immunohistochemistry
for correlative microscopy. *ELife*, *10*, e63392. https://doi.org/10.7554/eLife.63392

Genoud, C., Titze, B., Graff-Meyer, A., & Friedrich, R. W. (2018). Fast Homogeneous En Bloc
Staining of Large Tissue Samples for Volume Electron Microscopy. *Frontiers in
Neuroanatomy*, *12*, 76. https://doi.org/10.3389/fnana.2018.00076

Goetz, J., Jessen, Z. F., Jacobi, A., Mani, A., Cooler, S., Greer, D., Kadri, S., Segal, J., Shekhar,
K., Sanes, J. R., & Schwartz, G. W. (2022). Unified classification of mouse retinal
ganglion cells using function, morphology, and gene expression. *Cell Reports*, *40*(2),
111040. https://doi.org/10.1016/j.celrep.2022.111040

Gong, J., Jellali, A., Mutterer, J., Sahel, J. A., Rendon, A., & Picaud, S. (2006). Distribution of
vesicular glutamate transporters in rat and human retina. *Brain Research*, *1082*(1), 73–85.
https://doi.org/10.1016/j.brainres.2006.01.111

Graham, B. J., Hildebrand, D. G. C., Kuan, A. T., Maniates-Selvin, J. T., Thomas, L. A., Shanny, B. L., & Lee, W.-C. A. (2019). *High-throughput transmission electron microscopy with automated serial sectioning* (p. 657346). bioRxiv. https://doi.org/10.1101/657346

Grimes, W. N., Seal, R. P., Oesch, N., Edwards, R. H., & Diamond, J. S. (2011). Genetic targeting and physiological features of VGLUT3+ amacrine cells. *Visual Neuroscience*, *28*(5), 381–392. https://doi.org/10.1017/S0952523811000290

Grimes, W. N., Sedlacek, M., Musgrove, M., Nath, A., Tian, H., Hoon, M., Rieke, F., Singer, J. H., & Diamond, J. S. (2022). Dendro-somatic synaptic inputs to ganglion cells contradict receptive field and connectivity conventions in the mammalian retina. *Current Biology : CB*, *32*(2), 315-328.e4. https://doi.org/10.1016/j.cub.2021.11.005

Grove, J. C. R., Hirano, A. A., de Los Santos, J., McHugh, C. F., Purohit, S., Field, G. D., Brecha, N. C., & Barnes, S. (2019). Novel hybrid action of GABA mediates inhibitory feedback in the mammalian retina. *PLoS Biology*, *17*(4), e3000200. https://doi.org/10.1371/journal.pbio.3000200

Habermann, C. J., O'Brien, B. J., Wässle, H., & Protti, D. A. (2003). AII Amacrine Cells Express L-Type Calcium Channels at Their Output Synapses. *The Journal of Neuroscience*, *23*(17), 6904–6913. https://doi.org/10.1523/JNEUROSCI.23-17-06904.2003

Hamos, J. E., Van Horn, S. C., Raczkowski, D., Uhlrich, D. J., & Sherman, S. M. (1985). Synaptic connectivity of a local circuit neurone in lateral geniculate nucleus of the cat. *Nature*, *317*(6038), Article 6038. https://doi.org/10.1038/317618a0

Hartline, H. K. (1938). The response of single optic nerve fibers of the vertebrate eye to illumination of the retina. *American Journal of Physiology*, *121*, 400–415.

Haverkamp, S., & Wässle, H. (2004). Characterization of an amacrine cell type of the mammalian retina immunoreactive for vesicular glutamate transporter 3. *Journal of Comparative Neurology*, *468*(2), 251–263. https://doi.org/10.1002/cne.10962

Hayworth, K. J., Morgan, J. L., Schalek, R., Berger, D. R., Hildebrand, D. G. C., & Lichtman, J. W. (2014). Imaging ATUM ultrathin section libraries with WaferMapper: A multi-scale approach to EM reconstruction of neural circuits. *Frontiers in Neural Circuits*, *8*, 68. https://doi.org/10.3389/fncir.2014.00068

Heidelberger, R., Heinemann, C., Neher, E., & Matthews, G. (1994). Calcium dependence of the rate of exocytosis in a synaptic terminal. *Nature*, *371*(6497), Article 6497. https://doi.org/10.1038/371513a0

Hellmer, C. B., Zhou, Y., Fyk-Kolodziej, B., Hu, Z., & Ichinose, T. (2016). Morphological and physiological analysis of type-5 and other bipolar cells in the Mouse Retina. *Neuroscience*, *315*, 246–258. https://doi.org/10.1016/j.neuroscience.2015.12.016

Helmstaedter, M., Briggman, K. L., Turaga, S. C., Jain, V., Seung, H. S., & Denk, W. (2013). Connectomic reconstruction of the inner plexiform layer in the mouse retina. *Nature*, *500*(7461), 168–174. https://doi.org/10.1038/nature12346

Hildebrand, D. G. C., Cicconet, M., Torres, R. M., Choi, W., Quan, T. M., Moon, J., Wetzel, A. W., Champion, A. S., Graham, B. J., Randlett, O., Plummer, G. S., Portugues, R., Bianco, I. H., Saalfeld, S., Baden, A. D., Lillaney, K., Burns, R., Vogelstein, J. T., Schier, A. F., … Engert, F. (2017). Whole-brain serial-section electron microscopy in larval zebrafish. *Nature*, *545*(7654), 345–349. https://doi.org/10.1038/nature22356

Hirabayashi, Y., Tapia, J. C., & Polleux, F. (2018). Correlated Light-Serial Scanning Electron Microscopy (CoLSSEM) for ultrastructural visualization of single neurons in vivo. *Scientific Reports*, *8*, 14491. https://doi.org/10.1038/s41598-018-32820-5

Holt, G. R., & Koch, C. (1997). Shunting inhibition does not have a divisive effect on firing rates. *Neural Computation*, *9*(5), 1001–1013. https://doi.org/10.1162/neco.1997.9.5.1001

Hsiang, J.-C., Johnson, K. P., Madisen, L., Zeng, H., & Kerschensteiner, D. (2017). Local processing in neurites of VGluT3-expressing amacrine cells differentially organizes visual information. *ELife*, *6*, e31307. https://doi.org/10.7554/eLife.31307

Hua, Y., Laserstein, P., & Helmstaedter, M. (2015). Large-volume en-bloc staining for electron microscopy-based connectomics. *Nature Communications*, *6*, 7923. https://doi.org/10.1038/ncomms8923

Ichinose, T., Fyk-Kolodziej, B., & Cohn, J. (2014). Roles of ON Cone Bipolar Cell Subtypes in Temporal Coding in the Mouse Retina. *Journal of Neuroscience*, *34*(26), 8761–8771. https://doi.org/10.1523/JNEUROSCI.3965-13.2014

Ichinose, T., & Habib, S. (2022). On and off signaling pathways in the retina and the visual system. *Frontiers in Ophthalmology*, *2*. https://www.frontiersin.org/articles/10.3389/fopht.2022.989002

Jacoby, J., & Schwartz, G. W. (2017). Three Small-Receptive-Field Ganglion Cells in the Mouse Retina Are Distinctly Tuned to Size, Speed, and Object Motion. *The Journal of Neuroscience*, *37*(3), 610–625. https://doi.org/10.1523/JNEUROSCI.2804-16.2016

Jacoby, J., Zhu, Y., DeVries, S. H., & Schwartz, G. W. (2015). An Amacrine Cell Circuit for Signaling Steady Illumination in the Retina. *Cell Reports*, *13*(12), 2663–2670. https://doi.org/10.1016/j.celrep.2015.11.062

Jain, V., Seung, H. S., & Turaga, S. C. (2010). Machines that learn to segment images: A crucial technology for connectomics. *Current Opinion in Neurobiology*, *20*(5), 653–666. https://doi.org/10.1016/j.conb.2010.07.004

Januszewski, M., Kornfeld, J., Li, P. H., Pope, A., Blakely, T., Lindsey, L., Maitin-Shepard, J., Tyka, M., Denk, W., & Jain, V. (2018). High-precision automated reconstruction of neurons with flood-filling networks. *Nature Methods*, *15*(8), Article 8. https://doi.org/10.1038/s41592-018-0049-4

Jeon, C.-J., Strettoi, E., & Masland, R. H. (1998). The Major Cell Populations of the Mouse Retina. *The Journal of Neuroscience*, *18*(21), 8936–8946. https://doi.org/10.1523/JNEUROSCI.18-21-08936.1998

Jia, Y., Lee, S., Zhuo, Y., & Zhou, Z. J. (2020). A retinal circuit for the suppressed-by-contrast receptive field of a polyaxonal amacrine cell. *Proceedings of the National Academy of Sciences*, *117*(17), 9577–9583. https://doi.org/10.1073/pnas.1913417117

Joesch, M., Mankus, D., Yamagata, M., Shahbazi, A., Schalek, R., Suissa-Peleg, A., Meister, M., Lichtman, J. W., Scheirer, W. J., & Sanes, J. R. (2016). Reconstruction of genetically identified neurons imaged by serial-section electron microscopy. *ELife*, *5*, e15015. https://doi.org/10.7554/eLife.15015

Jones, I. S., & Kording, K. P. (2022). Do Biological Constraints Impair Dendritic Computation? *Neuroscience*, *489*, 262–274. https://doi.org/10.1016/j.neuroscience.2021.07.036

Kasthuri, N., Hayworth, K. J., Berger, D. R., Schalek, R. L., Conchello, J. A., Knowles-Barley, S., Lee, D., Vázquez-Reina, A., Kaynig, V., Jones, T. R., Roberts, M., Morgan, J. L., Tapia, J. C., Seung, H. S., Roncal, W. G., Vogelstein, J. T., Burns, R., Sussman, D. L.,

Priebe, C. E., … Lichtman, J. W. (2015). Saturated Reconstruction of a Volume of Neocortex. *Cell*, *162*(3), 648–661. https://doi.org/10.1016/j.cell.2015.06.054

Katz, B., & Miledi, R. (1967). Ionic Requirements of Synaptic Transmitter Release. *Nature*, *215*(5101), Article 5101. https://doi.org/10.1038/215651a0

Keeley, P. W., Lebo, M. C., Vieler, J. D., Kim, J. J., St John, A. J., & Reese, B. E. (2021). Interrelationships between Cellular Density, Mosaic Patterning, and Dendritic Coverage of VGluT3 Amacrine Cells. *The Journal of Neuroscience: The Official Journal of the Society for Neuroscience*, *41*(1), 103–117. https://doi.org/10.1523/JNEUROSCI.1027-20.2020

Kerschensteiner, D. (2022). Feature Detection by Retinal Ganglion Cells. *Annual Review of Vision Science*, *8*(1), 135–169. https://doi.org/10.1146/annurev-vision-100419-112009

Kesserwani, H. (2020). The Biophysics of Visual Edge Detection: A Review of Basic Principles. *Cureus*, *12*(10), e11218. https://doi.org/10.7759/cureus.11218

Khani, M. H., & Gollisch, T. (2021). Linear and nonlinear chromatic integration in the mouse retina. *Nature Communications*, *12*(1), Article 1. https://doi.org/10.1038/s41467-021-22042-1

Kim, J. S., Greene, M. J., Zlateski, A., Lee, K., Richardson, M., Turaga, S. C., Purcaro, M., Balkam, M., Robinson, A., Behabadi, B. F., Campos, M., Denk, W., & Seung, H. S. (2014). Space–time wiring specificity supports direction selectivity in the retina. *Nature*, *509*(7500), Article 7500. https://doi.org/10.1038/nature13240

Kim, T., Shen, N., Hsiang, J.-C., Johnson, K. P., & Kerschensteiner, D. (2020). Dendritic and parallel processing of visual threats in the retina control defensive responses. *Science Advances*, *6*(47), eabc9920. https://doi.org/10.1126/sciadv.abc9920

Kim, T., Soto, F., & Kerschensteiner, D. (2015). An excitatory amacrine cell detects object motion and provides feature-selective input to ganglion cells in the mouse retina. *ELife*, *4*, e08025. https://doi.org/10.7554/eLife.08025

Koch, C., Poggio, T., & Torre, V. (1983). Nonlinear interactions in a dendritic tree: Localization, timing, and role in information processing. *Proceedings of the National Academy of Sciences of the United States of America*, *80*(9), 2799–2802. https://doi.org/10.1073/pnas.80.9.2799

Koehler, C. C., Hall, L. M., Hellmer, C. B., & Ichinose, T. (2019). Using Looming Visual Stimuli to Evaluate Mouse Vision. *Journal of Visualized Experiments*, *148*, 59766. https://doi.org/10.3791/59766

Kolb, H. (1997). Amacrine cells of the mammalian retina: Neurocircuitry and functional roles. *Eye*, *11*(6), Article 6. https://doi.org/10.1038/eye.1997.230

Kolb, H., Nelson, R., & Mariani, A. (1981). Amacrine cells, bipolar cells and ganglion cells of the cat retina: A Golgi study. *Vision Research*, *21*(7), 1081–1114. https://doi.org/10.1016/0042-6989(81)90013-4

Kozlowska, K., Walker, P., McLean, L., & Carrive, P. (2015). Fear and the Defense Cascade: Clinical Implications and Management. *Harvard Review of Psychiatry*, *23*(4), 263–287. https://doi.org/10.1097/HRP.0000000000000065

Krishnaswamy, A., Yamagata, M., Duan, X., Hong, Y. K., & Sanes, J. R. (2015). Sidekick 2 directs formation of a retinal circuit that detects differential motion. *Nature*, *524*(7566), Article 7566. https://doi.org/10.1038/nature14682

Kubota, Y., Sohn, J., Hatada, S., Schurr, M., Straehle, J., Gour, A., Neujahr, R., Miki, T., Mikula, S., & Kawaguchi, Y. (2018). A carbon nanotube tape for serial-section electron

microscopy of brain ultrastructure. *Nature Communications*, *9*, 437. https://doi.org/10.1038/s41467-017-02768-7

Kubota, Y., Sohn, J., & Kawaguchi, Y. (2018). Large Volume Electron Microscopy and Neural Microcircuit Analysis. *Frontiers in Neural Circuits*, *12*, 98. https://doi.org/10.3389/fncir.2018.00098

Kuffler, S. W. (1953). Discharge patterns and functional organization of mammalian retina. *Journal of Neurophysiology*, *16*(1), 37–68. https://doi.org/10.1152/jn.1953.16.1.37

Lagnado, L. (1998). Retinal processing: Amacrine cells keep it short and sweet. *Current Biology*, *8*(17), R598–R600. https://doi.org/10.1016/S0960-9822(98)70385-9

Lam, S. S., Martell, J. D., Kamer, K. J., Deerinck, T. J., Ellisman, M. H., Mootha, V. K., & Ting, A. Y. (2015). Directed evolution of APEX2 for electron microscopy and proteomics. *Nature Methods*, *12*(1), 51–54. https://doi.org/10.1038/nmeth.3179

Lee, S., Chen, L., Chen, M., Ye, M., Seal, R. P., & Zhou, Z. J. (2014). An Unconventional Glutamatergic Circuit in the Retina Formed by vGluT3 Amacrine Cells. *Neuron*, *84*(4), 708–715. https://doi.org/10.1016/j.neuron.2014.10.021

Lee, S., Zhang, Y., Chen, M., & Zhou, Z. J. (2016). Segregated glycine-glutamate co-transmission from vGluT3 amacrine cells to contrast-suppressed and contrast-enhanced retinal circuits. *Neuron*, *90*(1), 27–34. https://doi.org/10.1016/j.neuron.2016.02.023

Lees, R. N., Akbar, A. F., & Badea, T. C. (2020). Retinal ganglion cell defects cause decision shifts in visually evoked defense responses. *Journal of Neurophysiology*, *124*(5), 1530–1549. https://doi.org/10.1152/jn.00474.2019

Lenzi, S. C., Cossell, L., Grainger, B., Olesen, S. F., Branco, T., & Margrie, T. W. (2022). Threat history controls flexible escape behavior in mice. *Current Biology: CB*, *32*(13), 2972-2979.e3. https://doi.org/10.1016/j.cub.2022.05.022

Li, J., Wang, Y., Chiu, S.-L., & Cline, H. T. (2010). Membrane Targeted Horseradish Peroxidase as a Marker for Correlative Fluorescence and Electron Microscopy Studies. *Frontiers in Neural Circuits*, *4*, 6. https://doi.org/10.3389/neuro.04.006.2010

Lin, B., & Masland, R. H. (2006). Populations of wide-field amacrine cells in the mouse retina. *Journal of Comparative Neurology*, *499*(5), 797–809. https://doi.org/10.1002/cne.21126

Liu, D., Li, S., Ren, L., Liu, X., Li, X., & Wang, Z. (2022). Different coding characteristics between flight and freezing in dorsal periaqueductal gray of mice during exposure to innate threats. *Animal Models and Experimental Medicine*, *5*(6), 491–501. https://doi.org/10.1002/ame2.12276

Liu, X., Hirano, A. A., Sun, X., Brecha, N. C., & Barnes, S. (2013). Calcium channels in rat horizontal cells regulate feedback inhibition of photoreceptors through an unconventional GABA- and pH-sensitive mechanism. *The Journal of Physiology*, *591*(13), 3309–3324. https://doi.org/10.1113/jphysiol.2012.248179

Liu, Z., Kimura, Y., Higashijima, S., Hildebrand, D. G. C., Morgan, J. L., & Bagnall, M. W. (2021). Central vestibular tuning arises from patterned convergence of otolith afferents. *Neuron*, *109*(5), 905. https://doi.org/10.1016/j.neuron.2021.02.005

London, M., & Häusser, M. (2005). Dendritic Computation. *Annual Review of Neuroscience*, *28*(1), 503–532. https://doi.org/10.1146/annurev.neuro.28.061604.135703

Ma, J., du Hoffmann, J., Kindel, M., Beas, B. S., Chudasama, Y., & Penzo, M. A. (2021). Divergent projections of the paraventricular nucleus of the thalamus mediate the selection of passive and active defensive behaviors. *Nature Neuroscience*, *24*(10), 1429–1440. https://doi.org/10.1038/s41593-021-00912-7

MacNeil, M. A., Heussy, J. K., Dacheux, R. F., Raviola, E., & Masland, R. H. (1999). The shapes and numbers of amacrine cells: Matching of photofilled with Golgi-stained cells in the rabbit retina and comparison with other mammalian species. *The Journal of Comparative Neurology*, *413*(2), 305–326.

MacNeil, M. A., & Masland, R. H. (1998). Extreme diversity among amacrine cells: Implications for function. *Neuron*, *20*(5), 971–982. https://doi.org/10.1016/s0896-6273(00)80478-x

Magee, J. C. (2000). Dendritic integration of excitatory synaptic input. *Nature Reviews. Neuroscience*, *1*(3), 181–190. https://doi.org/10.1038/35044552

Maranto, A. R. (1982). Neuronal Mapping: A Photooxidation Reaction Makes Lucifer Yellow Useful for Electron Microscopy. *Science*, *217*(4563), 953–955. https://doi.org/10.1126/science.7112109

Marc, R. E., Anderson, J. R., Jones, B. W., Sigulinsky, C. L., & Lauritzen, J. S. (2014). The AII amacrine cell connectome: A dense network hub. *Frontiers in Neural Circuits*, *8*, 104. https://doi.org/10.3389/fncir.2014.00104

Marc, R. E., Sigulinsky, C. L., Pfeiffer, R. L., Emrich, D., Anderson, J. R., & Jones, B. W. (2018). Heterocellular Coupling Between Amacrine Cells and Ganglion Cells. *Frontiers in Neural Circuits*, *12*. https://www.frontiersin.org/articles/10.3389/fncir.2018.00090

Martell, J. D., Deerinck, T. J., Sancak, Y., Poulos, T. L., Mootha, V. K., Sosinsky, G. E., Ellisman, M. H., & Ting, A. Y. (2012). Engineered ascorbate peroxidase as a genetically encoded reporter for electron microscopy. *Nature Biotechnology*, *30*(11), Article 11. https://doi.org/10.1038/nbt.2375

Martersteck, E. M., Hirokawa, K. E., Evarts, M., Bernard, A., Duan, X., Li, Y., Ng, L., Oh, S. W., Ouellette, B., Royall, J. J., Stoecklin, M., Wang, Q., Zeng, H., Sanes, J. R., & Harris, J. A. (2017). Diverse Central Projection Patterns of Retinal Ganglion Cells. *Cell Reports*, *18*(8), 2058–2072. https://doi.org/10.1016/j.celrep.2017.01.075

Martinez-Conde, S., Macknik, S. L., Troncoso, X. G., & Dyar, T. A. (2006). Microsaccades counteract visual fading during fixation. *Neuron*, *49*(2), 297–305. https://doi.org/10.1016/j.neuron.2005.11.033

Masland, R. H. (2001). The fundamental plan of the retina. *Nature Neuroscience*, *4*(9), Article 9. https://doi.org/10.1038/nn0901-877

Masland, R. H. (2012). The tasks of amacrine cells. *Visual Neuroscience*, *29*(1), 3–9. https://doi.org/10.1017/S0952523811000344

Maturana, H. R., Lettvin, J. Y., McCulloch, W. S., & Pitts, W. H. (1959). Evidence That Cut Optic Nerve Fibers in a Frog Regenerate to Their Proper Places in the Tectum. *Science*, *130*(3390), 1709–1710. https://doi.org/10.1126/science.130.3390.1709

McMahon, D. G., Knapp, A. G., & Dowling, J. E. (1989). Horizontal cell gap junctions: Single-channel conductance and modulation by dopamine. *Proceedings of the National Academy of Sciences of the United States of America*, *86*(19), 7639–7643. https://doi.org/10.1073/pnas.86.19.7639

Mikula, S., & Denk, W. (2015). High-resolution whole-brain staining for electron microscopic circuit reconstruction. *Nature Methods*, *12*(6), Article 6. https://doi.org/10.1038/nmeth.3361

Moore, J. J., Robert, V., Rashid, S. K., & Basu, J. (2022). Assessing Local and Branch-Specific Activity in Dendrites. *Neuroscience*, *489*, 143–164. https://doi.org/10.1016/j.neuroscience.2021.10.022

Morgan, J. L., Berger, D. R., Wetzel, A. W., & Lichtman, J. W. (2016). The Fuzzy Logic of Network Connectivity in Mouse Visual Thalamus. *Cell*, *165*(1), 192–206. https://doi.org/10.1016/j.cell.2016.02.033

Morgan, J. L., & Lichtman, J. W. (2013). Why not connectomics? *Nature Methods*, *10*(6), 494–500. https://doi.org/10.1038/nmeth.2480

Morgan, J. L., & Lichtman, J. W. (2017). Digital tissue and what it may reveal about the brain. *BMC Biology*, *15*(1), Article 1. https://doi.org/10.1186/s12915-017-0436-9

Münch, T. A., da Silveira, R. A., Siegert, S., Viney, T. J., Awatramani, G. B., & Roska, B. (2009). Approach sensitivity in the retina processed by a multifunctional neural circuit. *Nature Neuroscience*, *12*(10), Article 10. https://doi.org/10.1038/nn.2389

Murphy-Baum, B. L., & Taylor, W. R. (2015). The Synaptic and Morphological Basis of Orientation Selectivity in a Polyaxonal Amacrine Cell of the Rabbit Retina. *The Journal of Neuroscience*, *35*(39), 13336–13350. https://doi.org/10.1523/JNEUROSCI.1712-15.2015

Narushima, M., Agetsuma, M., & Nabekura, J. (2022). Development and experience-dependent modulation of the defensive behaviors of mice to visual threats. *The Journal of Physiological Sciences: JPS*, *72*(1), 5. https://doi.org/10.1186/s12576-022-00831-7

Neira, S., Hassanein, L. A., Stanhope, C. M., Buccini, M. C., D'Ambrosio, S. L., Flanigan, M. E., Haun, H. L., Boyt, K. M., Bains, J. S., & Kash, T. L. (2022). *Chronic Alcohol Consumption Alters Home-Cage Behaviors and Responses to Ethologically Relevant Predator Tasks in Mice* (p. 2022.02.04.479122). bioRxiv. https://doi.org/10.1101/2022.02.04.479122

Ölveczky, B. P., Baccus, S. A., & Meister, M. (2003). Segregation of object and background motion in the retina. *Nature*, *423*(6938), Article 6938. https://doi.org/10.1038/nature01652

Padmanabhan, K., Andrews, S. E., & Fitzpatrick, J. A. J. (2010). Multi-photon imaging. *Current Protocols in Cytometry*, *Chapter 2*, Unit2.9. https://doi.org/10.1002/0471142956.cy0209s54

Park, S. J. H., Kim, I.-J., Looger, L. L., Demb, J. B., & Borghuis, B. G. (2014). Excitatory synaptic inputs to mouse on-off direction-selective retinal ganglion cells lack direction tuning. *The Journal of Neuroscience: The Official Journal of the Society for Neuroscience*, *34*(11), 3976–3981. https://doi.org/10.1523/JNEUROSCI.5017-13.2014

Piccolino, M., Neyton, J., & Gerschenfeld, H. M. (1984). Decrease of gap junction permeability induced by dopamine and cyclic adenosine 3':5'-monophosphate in horizontal cells of turtle retina. *The Journal of Neuroscience: The Official Journal of the Society for Neuroscience*, *4*(10), 2477–2488. https://doi.org/10.1523/JNEUROSCI.04-10-02477.1984

Pologruto, T. A., Sabatini, B. L., & Svoboda, K. (2003). ScanImage: Flexible software for operating laser scanning microscopes. *BioMedical Engineering OnLine*, *2*(1), Article 1. https://doi.org/10.1186/1475-925X-2-13

Prescott, S. A., & De Koninck, Y. (2003). Gain control of firing rate by shunting inhibition: Roles of synaptic noise and dendritic saturation. *Proceedings of the National Academy of Sciences*, *100*(4), 2076–2081. https://doi.org/10.1073/pnas.0337591100

Rall, W. (1967). Distinguishing theoretical synaptic potentials computed for different soma-dendritic distributions of synaptic input. *Journal of Neurophysiology*, *30*(5), 1138–1168. https://doi.org/10.1152/jn.1967.30.5.1138

Rall, W. (1969). Time Constants and Electrotonic Length of Membrane Cylinders and Neurons. *Biophysical Journal*, *9*(12), 1483–1508.

Reinhard, K., Li, C., Do, Q., Burke, E. G., Heynderickx, S., & Farrow, K. (2019). A projection specific logic to sampling visual inputs in mouse superior colliculus. *ELife*, *8*, e50697. https://doi.org/10.7554/eLife.50697

Richardson, T. L., Turner, R. W., & Miller, J. J. (1987). Action-potential discharge in hippocampal CA1 pyramidal neurons: Current source-density analysis. *Journal of Neurophysiology*, *58*(5), 981–996. https://doi.org/10.1152/jn.1987.58.5.981

Robson, J. A., Mason, C. A., & Guillery, R. W. (1978). Terminal Arbors of Axons That Have Formed Abnormal Connections. *Science*, *201*(4356), 635–637. https://doi.org/10.1126/science.675248

Rodieck, R. W., & Stone, J. (1965). Analysis of receptive fields of cat retinal ganglion cells. *Journal of Neurophysiology*, *28*(5), 833–849. https://doi.org/10.1152/jn.1965.28.5.833

Rousso, D. L., Qiao, M., Kagan, R. D., Yamagata, M., Palmiter, R. D., & Sanes, J. R. (2016). Two pairs of ON and OFF retinal ganglion cells are defined by intersectional patterns of transcription factor expression. *Cell Reports*, *15*(9), 1930–1944. https://doi.org/10.1016/j.celrep.2016.04.069

Roy, K., Kumar, S., & Bloomfield, S. A. (2017). Gap junctional coupling between retinal amacrine and ganglion cells underlies coherent activity integral to global object perception. *Proceedings of the National Academy of Sciences*, *114*(48), E10484–E10493. https://doi.org/10.1073/pnas.1708261114

Saalfeld, S., Fetter, R., Cardona, A., & Tomancak, P. (2012). Elastic volume reconstruction from series of ultra-thin microscopy sections. *Nature Methods*, *9*(7), Article 7. https://doi.org/10.1038/nmeth.2072

Sabatini, B. L., & Regehr, W. G. (1996). Timing of neurotransmission at fast synapses in the mammalian brain. *Nature*, *384*(6605), Article 6605. https://doi.org/10.1038/384170a0

Schalek, R., Wilson, A., Lichtman, J., Josh, M., Kasthuri, N., Berger, D., Seung, S., Anger, P., Hayworth, K., & Aderhold, D. (2012). ATUM-based SEM for High-Speed Large-Volume Biological Reconstructions. *Microscopy and Microanalysis*, *18*(S2), 572–573. https://doi.org/10.1017/S1431927612004710

Schifferer, M., Snaidero, N., Djannatian, M., Kerschensteiner, M., & Misgeld, T. (2021). Niwaki Instead of Random Forests: Targeted Serial Sectioning Scanning Electron Microscopy With Reimaging Capabilities for Exploring Central Nervous System Cell Biology and Pathology. *Frontiers in Neuroanatomy*, *15*. https://www.frontiersin.org/articles/10.3389/fnana.2021.732506

Schlichtenbrede, F. C., Mittmann, W., Rensch, F., vom Hagen, F., Jonas, J. B., & Euler, T. (2009). Toxicity Assessment of Intravitreal Triamcinolone and Bevacizumab in a Retinal Explant Mouse Model Using Two-Photon Microscopy. *Investigative Ophthalmology & Visual Science*, *50*(12), 5880–5887. https://doi.org/10.1167/iovs.08-3078

Shang, C., Chen, Z., Liu, A., Li, Y., Zhang, J., Qu, B., Yan, F., Zhang, Y., Liu, W., Liu, Z., Guo, X., Li, D., Wang, Y., & Cao, P. (2018). Divergent midbrain circuits orchestrate escape and freezing responses to looming stimuli in mice. *Nature Communications*, *9*(1), 1232. https://doi.org/10.1038/s41467-018-03580-7

Shu, X., Lev-Ram, V., Deerinck, T. J., Qi, Y., Ramko, E. B., Davidson, M. W., Jin, Y., Ellisman, M. H., & Tsien, R. Y. (2011). A Genetically Encoded Tag for Correlated Light and

Electron Microscopy of Intact Cells, Tissues, and Organisms. *PLoS Biology*, *9*(4), e1001041. https://doi.org/10.1371/journal.pbio.1001041

Sjöstrand, F. S. (1958). Ultrastructure of retinal rod synapses of the guinea pig eye as revealed by three-dimensional reconstructions from serial sections. *Journal of Ultrastructure Research*, *2*(1), 122–170. https://doi.org/10.1016/S0022-5320(58)90050-9

Snaidero, N., Schifferer, M., Mezydlo, A., Zalc, B., Kerschensteiner, M., & Misgeld, T. (2020). Myelin replacement triggered by single-cell demyelination in mouse cortex. *Nature Communications*, *11*(1), Article 1. https://doi.org/10.1038/s41467-020-18632-0

Spira, A. W., & Hollenberg, M. J. (1973). Human retinal development: Ultrastructure of the inner retinal layers. *Developmental Biology*, *31*(1), 1–21.

Stella, S. L., Li, S., Sabatini, A., Vila, A., & Brecha, N. C. (2008). Comparison of the ontogeny of the vesicular glutamate transporter 3 (VGLUT3) with VGLUT1 and VGLUT2 in the rat retina. *Brain Research*, *1215*, 20–29. https://doi.org/10.1016/j.brainres.2008.03.038

Storchi, R., Milosavljevic, N., Allen, A. E., Zippo, A. G., Agnihotri, A., Cootes, T. F., & Lucas, R. J. (2020). A High-Dimensional Quantification of Mouse Defensive Behaviors Reveals Enhanced Diversity and Stimulus Specificity. *Current Biology: CB*, *30*(23), 4619-4630.e5. https://doi.org/10.1016/j.cub.2020.09.007

Strettoi, E., & Masland, R. H. (1996). The number of unidentified amacrine cells in the mammalian retina. *Proceedings of the National Academy of Sciences*, *93*(25), 14906–14911. https://doi.org/10.1073/pnas.93.25.14906

Strettoi, E., Raviola, E., & Dacheux, R. F. (1992). Synaptic connections of the narrow-field, bistratified rod amacrine cell (AII) in the rabbit retina. *Journal of Comparative Neurology*, *325*(2), 152–168. https://doi.org/10.1002/cne.903250203

Südhof, T. C. (2012). Calcium Control of Neurotransmitter Release. *Cold Spring Harbor Perspectives in Biology*, *4*(1), a011353. https://doi.org/10.1101/cshperspect.a011353

Tafreshiha, A., van der Burg, S. A., Smits, K., Blömer, L. A., & Heimel, J. A. (2021). Visual stimulus-specific habituation of innate defensive behaviour in mice. *Journal of Experimental Biology*, *224*(6), jeb230433. https://doi.org/10.1242/jeb.230433

Tapia, J. C., Kasthuri, N., Hayworth, K. J., Schalek, R., Lichtman, J. W., Smith, S. J., & Buchanan, J. (2012). High-contrast en bloc staining of neuronal tissue for field emission scanning electron microscopy. *Nature Protocols*, *7*(2), Article 2. https://doi.org/10.1038/nprot.2011.439

Tarnowski, B. I., Spinale, F. G., & Nicholson, J. H. (1991). DAPI as a useful stain for nuclear quantitation. *Biotechnic & Histochemistry: Official Publication of the Biological Stain Commission*, *66*(6), 297–302.

Taylor, W. R. (1996). Response properties of long-range axon-bearing amacrine cells in the dark-adapted rabbit retina. *Visual Neuroscience*, *13*(4), 599–604. https://doi.org/10.1017/s0952523800008506

Thoreson, W. B., & Mangel, S. C. (2012). Lateral interactions in the outer retina. *Progress in Retinal and Eye Research*, *31*(5), 407–441. https://doi.org/10.1016/j.preteyeres.2012.04.003

Tien, N.-W., Kim, T., & Kerschensteiner, D. (2016). Target-specific glycinergic transmission from VGluT3-expressing amacrine cells shapes suppressive contrast responses in the retina. *Cell Reports*, *15*(7), 1369–1375. https://doi.org/10.1016/j.celrep.2016.04.025

Tien, N.-W., Pearson, J. T., Heller, C. R., Demas, J., & Kerschensteiner, D. (2015). Genetically Identified Suppressed-by-Contrast Retinal Ganglion Cells Reliably Signal Self-Generated

Visual Stimuli. *The Journal of Neuroscience*, *35*(30), 10815–10820. https://doi.org/10.1523/JNEUROSCI.1521-15.2015

Trachtenberg, J. T., Chen, B. E., Knott, G. W., Feng, G., Sanes, J. R., Welker, E., & Svoboda, K. (2002). Long-term in vivo imaging of experience-dependent synaptic plasticity in adult cortex. *Nature*, *420*(6917), Article 6917. https://doi.org/10.1038/nature01273

Tran-Van-Minh, A., Cazé, R. D., Abrahamsson, T., Cathala, L., Gutkin, B. S., & DiGregorio, D. A. (2015). Contribution of sublinear and supralinear dendritic integration to neuronal computations. *Frontiers in Cellular Neuroscience*, *9*. https://www.frontiersin.org/articles/10.3389/fncel.2015.00067

Turaga, S. C., Murray, J. F., Jain, V., Roth, F., Helmstaedter, M., Briggman, K., Denk, W., & Seung, H. S. (2010). Convolutional Networks Can Learn to Generate Affinity Graphs for Image Segmentation. *Neural Computation*, *22*(2), 511–538. https://doi.org/10.1162/neco.2009.10-08-881

Vishwanathan, A., Daie, K., Ramirez, A. D., Lichtman, J. W., Aksay, E. R. F., & Seung, H. S. (2017). Electron Microscopic Reconstruction of Functionally Identified Cells in a Neural Integrator. *Current Biology*, *27*(14), 2137-2147.e3. https://doi.org/10.1016/j.cub.2017.06.028

Völgyi, B., Chheda, S., & Bloomfield, S. A. (2009). Tracer coupling patterns of the ganglion cell subtypes in the mouse retina. *Journal of Comparative Neurology*, *512*(5), 664–687. https://doi.org/10.1002/cne.21912

Wang, F., Li, E., De, L., Wu, Q., & Zhang, Y. (2021). OFF-transient alpha RGCs mediate looming triggered innate defensive response. *Current Biology*, *31*(11), 2263-2273.e3. https://doi.org/10.1016/j.cub.2021.03.025

Wanner, A. A., & Vishwanathan, A. (2018). Methods for Mapping Neuronal Activity to Synaptic Connectivity: Lessons From Larval Zebrafish. *Frontiers in Neural Circuits*, *12*, 89. https://doi.org/10.3389/fncir.2018.00089

Wässle, H., Puller, C., Müller, F., & Haverkamp, S. (2009). Cone contacts, mosaics, and territories of bipolar cells in the mouse retina. *The Journal of Neuroscience: The Official Journal of the Society for Neuroscience*, *29*(1), 106–117. https://doi.org/10.1523/JNEUROSCI.4442-08.2009

Weitz, A. C., Behrend, M. R., Lee, N. S., Klein, R. L., Chiodo, V. A., Hauswirth, W. W., Humayun, M. S., Weiland, J. D., & Chow, R. H. (2013). Imaging the response of the retina to electrical stimulation with genetically encoded calcium indicators. *Journal of Neurophysiology*, *109*(7), 1979–1988. https://doi.org/10.1152/jn.00852.2012

Wheatcroft, T., Saleem, A. B., & Solomon, S. G. (2022). Functional Organisation of the Mouse Superior Colliculus. *Frontiers in Neural Circuits*, *16*, 792959. https://doi.org/10.3389/fncir.2022.792959

White, J. G., Southgate, E., Thomson, J. N., & Brenner, S. (1986). The structure of the nervous system of the nematode Caenorhabditis elegans. *Philosophical Transactions of the Royal Society of London. Series B, Biological Sciences*, *314*(1165), 1–340. https://doi.org/10.1098/rstb.1986.0056

Willingham, M. C., & Rutherford, A. V. (1984). The use of osmium-thiocarbohydrazide-osmium (OTO) and ferrocyanide-reduced osmium methods to enhance membrane contrast and preservation in cultured cells. *Journal of Histochemistry & Cytochemistry*, *32*(4), 455–460. https://doi.org/10.1177/32.4.6323574

Wu, Q., & Zhang, Y. (2023). Neural Circuit Mechanisms Involved in Animals' Detection of and Response to Visual Threats. *Neuroscience Bulletin*. https://doi.org/10.1007/s12264-023-01021-0

Xu, C. S., Pang, S., Shtengel, G., Müller, A., Ritter, A. T., Hoffman, H. K., Takemura, S.-Y., Lu, Z., Pasolli, H. A., Iyer, N., Chung, J., Bennett, D., Weigel, A. V., Freeman, M., van Engelenburg, S. B., Walther, T. C., Farese, R. V., Lippincott-Schwartz, J., Mellman, I., … Hess, H. F. (2021). An open-access volume electron microscopy atlas of whole cells and tissues. *Nature*, *599*(7883), 147–151. https://doi.org/10.1038/s41586-021-03992-4

Yamada, E. S., Dmitrieva, N., Keyser, K. T., Lindstrom, J. M., Hersh, L. B., & Marshak, D. W. (2003). Synaptic connections of starburst amacrine cells and localization of acetylcholine receptors in primate retinas. *The Journal of Comparative Neurology*, *461*(1), 76–90. https://doi.org/10.1002/cne.10672

Yan, W., Laboulaye, M. A., Tran, N. M., Whitney, I. E., Benhar, I., & Sanes, J. R. (2020). Mouse Retinal Cell Atlas: Molecular Identification of over Sixty Amacrine Cell Types. *Journal of Neuroscience*, *40*(27), 5177–5195. https://doi.org/10.1523/JNEUROSCI.0471-20.2020

Yang, H. H., St-Pierre, F., Sun, X., Ding, X., Lin, M. Z., & Clandinin, T. R. (2016). Subcellular Imaging of Voltage and Calcium Signals Reveals Neural Processing In Vivo. *Cell*, *166*(1), 245–257. https://doi.org/10.1016/j.cell.2016.05.031

Yang, X., Liu, Q., Zhong, J., Song, R., Zhang, L., & Wang, L. (2020). A simple threat-detection strategy in mice. *BMC Biology*, *18*. https://doi.org/10.1186/s12915-020-00825-0

Yilmaz, M., & Meister, M. (2013). Rapid Innate Defensive Responses of Mice to Looming Visual Stimuli. *Current Biology*, *23*(20), 2011–2015. https://doi.org/10.1016/j.cub.2013.08.015

Yin, W., Brittain, D., Borseth, J., Scott, M. E., Williams, D., Perkins, J., Own, C. S., Murfitt, M., Torres, R. M., Kapner, D., Mahalingam, G., Bleckert, A., Castelli, D., Reid, D., Lee, W.-C. A., Graham, B. J., Takeno, M., Bumbarger, D. J., Farrell, C., … da Costa, N. M. (2020). A petascale automated imaging pipeline for mapping neuronal circuits with high-throughput transmission electron microscopy. *Nature Communications*, *11*(1), Article 1. https://doi.org/10.1038/s41467-020-18659-3

Zhang, Q., Lee, W.-C. A., Paul, D. L., & Ginty, D. D. (2019). Multiplexed peroxidase-based electron microscopy labeling enables simultaneous visualization of multiple cell types. *Nature Neuroscience*, *22*(5), Article 5. https://doi.org/10.1038/s41593-019-0358-7

Zhang, Y., Kim, I.-J., Sanes, J. R., & Meister, M. (2012). The most numerous ganglion cell type of the mouse retina is a selective feature detector. *Proceedings of the National Academy of Sciences*, *109*(36), E2391–E2398. https://doi.org/10.1073/pnas.1211547109